EVALUATION OF HYBRID-ELECTRIC POWER SYSTEM INTEGRATION CHALLENGES FOR MULTI-ROTOR UAS

By

KRISTEN ELISE MCKINNEY

Bachelor of Science in Mechanical Engineering

Oklahoma State University

Stillwater, Oklahoma

2016

Submitted to the Faculty of the
Graduate College of the
Oklahoma State University
in partial fulfillment of
the requirements for
the Degree of
MASTER OF SCIENCE
May, 2018

EVALUATION OF HYBRID-ELECTRIC POWER SYSTEM INTEGRATION CHALLENGES FOR MULTI-ROTOR UAS

Thesis Approved:

Dr. Jamey Jacob

Thesis Adviser

Dr. Richard Gaeta

Dr. Kurt Rouser

Dr. James Kidd

Name: Kristen E. McKinney

Date of Degree: MAY, 2018

Title of Study: EVALUATION OF HYBRID-ELECTRIC POWER SYSTEM

INTEGRATION CHALLENGES FOR MULTI-ROTOR UAS

Major Field: MECHANICAL AND AEROSPACE ENGINEERING

ABSTRACT:

The modern standard for multi-rotor unmanned aircraft system (UAS) propulsion is an electric configuration typically consisting of battery-powered electric motors. The primary issue with this type of propulsion system is the low energy density of the battery, which results in shorter flight times or lower payload capacity than typically desired. One possible solution for this is implementation of a hybrid-electric power system, which has been demonstrated to improve endurance in both fixed and rotary wing aircraft. The purpose of this study is to investigate the integration challenges of implementing a hybrid-electric power system on multi-rotor UAS, specifically one that utilizes a gasoline internal combustion engine. While design of a fully-integrated hybrid-electric power system is not within the scope of this study, rather experiments are conducted with intentions to provide crucial insights to expedite the design and implementation process. Integration challenges such as vibration, cooling requirements, and additional noise of small combustion engines are investigated. It is shown that a small combustion engine can produce forceful vibration signatures, the affects of which must be considered when designing a hybrid-electric power system. Without proper dampening, this additional vibration has been shown to negatively impact the function of the on-board sensors necessary for controlling small UAS (sUAS). It has also been shown that forced convection, or other external cooling, is a requirement for the small combustion engine used for this study, which presents a unique challenge in hover-capable aircraft that don't inherently supply active airflow. However, the cooling requirements of these types of engines can be estimated when designing a hybrid-electric power system, and weight-efficient solutions can be found. Finally, it has been shown that a small, two-stroke combustion engine would have a significant contribution to the overall noise signature of a hybrid-electric sUAS. Through a computational method of isolating and combining individual noise sources, the theoretical acoustic signature of a multi-rotor sUAS with a hybrid-electric power system was produced. The conclusion of this study confirms that each of the initially identified major integration challenges (vibration, cooling, and noise) must be considered when designing a hybrid-electric power system for multi-rotor sUAS, and also provides insights into how each challenge could be addressed.

ACKNOWLEDGEMENTS

I would like to thank my committee members for their support and guidance throughout my graduate journey. I would especially like to thank Dr. Jamey Jacob for his invaluable mentorship, and Dr. Richard Gaeta for the inspiration to pursue this research.

I would also like to thank Jordan Feight for his continued assistance, encouragement, and support throughout this research effort, and for going above and beyond to help me reach my goals.

Lastly, I would like to thank my friends and family for always believing in me.

TABLE OF CONTENTS

LIST OF TABLES

LIST OF FIGURES

CHAPTER I

INTRODUCTION

1.1 Motivation

Due to the increase in usage of unmanned aircraft systems (UAS) in both industry and military fields, there has been a recent increase of interest in exploring the boundaries and limitations of this technology and pursuing advancements that would allow for broader mission capabilities. There are a variety of applications that would benefit in particular from the expansion of payload and endurance capabilities of small UAS, such as photogrammetry, surveillance, and payload transportation. Nex [1] explains that while photogrammetry has previously been reliant on manned aircraft for image collection, the increasing availability and decreasing cost of small UAS has opened new doors in this field. He also stipulates that endurance limitations of some UAS can lead to difficulty in data collection and post-processing.

The main driving factor for endurance as well as payload capacity is the propulsion system of the aircraft. There are two main types of UAS, based on the method of lift: fixed-wing and rotorcraft. Fixed-wing aircraft generate lift with the aerodynamics of their wing structures, and are driven usually by a single propeller. Rotorcraft generate lift with a single or multiple rotors oriented parallel to the ground, and travel by directing the flow into the rotors or changing the speed of rotors to change the roll and pitch which in turn propels the rotorcraft in the desired direction.

Fixed-wing aircraft can be powered by either electric motors or combustion engines as the source of mechanical power to the propeller(s). Power for these aircraft can be drawn from batteries alone, both for the onboard electronics and the propulsion system with an electric motor. When using a combustion engine, power for propulsion is drawn from the fuel and power for onboard electronics is typically drawn from a secondary battery supply. Multi-rotor aircraft are typically driven by electric motors that receive power from batteries. Due to the necessity of distributing power to multiple propulsion points on these vehicles, mechanical power from combustion is traditionally not utilized.

Despite rapid development in many areas of UAS technology, there are potentially limits to the advancements of battery technology, which specifically limit the endurance capabilities of electrically-powered aircraft [2]. Because of this, new and innovative methods of supplying power to these vehicles must be considered. The scope of this work is to investigate on-board power generation as a supplement to passively stored power to increase endurance, specifically for multi-rotor aircraft. While fixed-wing aircraft could also benefit from endurance-boosting solutions, multi-rotor aircraft were chosen for investigation in this study to fill a research gap. There are several companies currently attempting to produce and sell hybrid power systems for multi-rotor UAS [3][4][5], but there are limited detailed technical publications about this technology.

The method of interest for extending endurance of multi-rotor UAS is a hybrid power system that actively generates power during flight as well as storing excess for rapid distribution when necessary. There are many existing technologies for power generation and storage that could be combined for this purpose. A gasoline internal combustion engine (ICE), specifically one utilizing intermittent combustion (piston engines), has been chosen for this work. Piston ICEs are a well-known mechanical power source, and there are several readily-available options in the size and power range of interest for this study. The mechanical power from the engine would drive an alternator and produce electrical power on-board which can either be directly distributed to the propulsion system (electric motors) or stored in LiPo batteries.

1.2 Goals

When considering the implementation of a hybrid-electric power system, as discussed above, on multi-rotor aircraft, the following basic integration challenges are anticipated: vibration, cooling, and noise. Small internal combustion engines are known to produce strong vibrations during operation, which could potentially affect the function of the onboard control and navigation sensors as well as drive structural design decisions for the aircraft of interest. These engines also produce significant amounts of heat that must be properly dissipated in order to allow the engine to continue to function and efficiently deliver power. Last, but not least, the combustion and mechanical noise produced by these small engines has the potential to significantly affect the overall noise signature of a multi-rotor platform.

For the investigation of the ramifications when introducing additional vibration to a multi-rotor UAS, the first step will be to characterize the expected vibration from small combustion engines. The vibration of a small internal combustion engine running on a test stand at relevant operating points will be measured to determine the magnitude and general characteristics. Depending on the results of this characterization, it will be determined if a suitable method exists for replication of this vibration signature with a system that could be easily mounted to a COTS multi-rotor platform for flight-testing. By isolating a single integration challenge for initial flight tests, it can be determined what issues, if any, are caused by vibration alone. The severity of these issues, such as disrupting communication or affecting navigation precision, can then be determined and strategies for mitigation can be developed.

For the investigation of the cooling requirements of small internal combustion engines, the temperature behavior of a small internal combustion engine will be observed during operation on a test stand at relevant operating points, and a determination will be made as to whether or not these engines can operate in static air with no additional cooling system. If additional cooling is required, calculations will be done to estimate this requirement for small engines of interest, and potential cooling solutions will be identified. Based on these results, it can also be determined whether or not the added complexity and weight for the required cooling system will detract significantly from the overall benefit of implementing a hybrid-electric power system.

For the investigation of the combustion engine noise signature, acoustic measurements will be taken of the internal combustion engine running on a test stand, both in indoor and outdoor environments, at relevant operating points. Steps will also be taken to isolate what components of the collected acoustic data are due solely to the engine's combustion and mechanical noise from any ambient noise contributions as well as contributions from the engine loading method. Acoustic measurements will also be taken of COTS multi-rotor platforms of interest in flight to identify a baseline for the common electric-only configuration of this type of UAS. Based on these two data sets, an analytical technique will be used to normalize the data and estimate the combined noise signature from both of these sources. Based on these results, noise reduction strategies can be discussed, and determinations can be made for what missions the noise signature from a hybrid-electric UAS might be prohibitive.

CHAPTER II

BACKGROUND & PREVIOUS WORK

2.1 Previous Work

For fixed-wing UAS the two main types of propulsion systems are battery-driven electric motors and ICE-driven, while for rotorcraft UAS (specifically multi-rotors) the main type of propulsion system is battery-driven electric motors, due to the mechanical complexity of implementing an ICE-driven propulsion system to multiple rotors. Battery driven propulsion systems are mechanically simple, provide instantaneous torque, and usually have low weight and footprint. However, ICE-driven propulsion systems have much higher energy density (Figure 1), which is crucial for endurance.

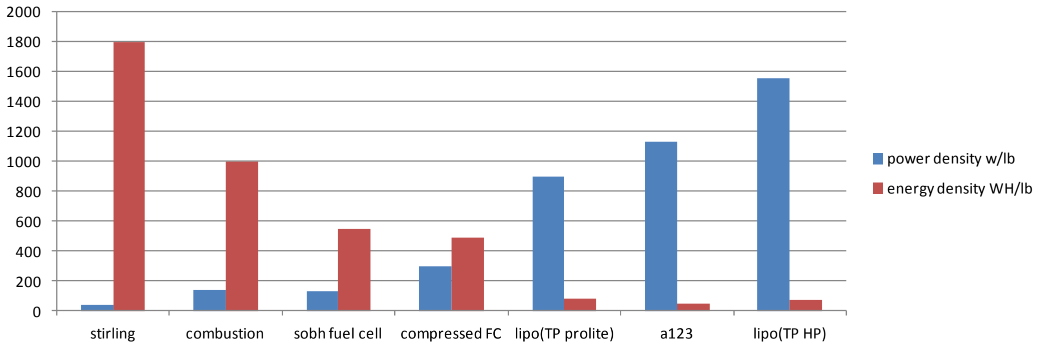

Figure 1: Comparison between power density (W/lb) and energy density (W-hr/lb) for several common power sources [6]

A hybrid power system could potentially increase the endurance of UAS by combining the benefits of a battery-driven propulsion system with those of an ICE-driven propulsion system. This technology has been used in other applications, such as automotive and other ground vehicle systems. Morita[7] identifies hybrid-electric vehicles as being one of the few alternatives to conventional vehicles that competes in terms of cost and convenience, while also promising good efficiency with a variety of fuels. These types of vehicles allow the engine to function at its most efficient operating point to supply a steady load while the electrical power storage component provides a buffer which can either absorb excess or supply the deficit as the power requirement changes with time [8].

The two most common types of hybrid power systems for UAS are fuel cell and hybrid electric. Both options are desirable for their higher energy density in comparison to batteries. Fuel cells also have minimal mechanical losses, no undesirable emissions, and low noise signature. However, fuel cells tend to be fairly costly to implement, require an on-board hydrogen supply, and the reliability of fuel cells as an energy source for UAS is relatively untested [9]. Fuel cell hybrid propulsion systems have been explored in simulation, and show promise with optimization [10].

While ICEs generally have greater noise signatures and higher emissions than fuel cells, they are relatively inexpensive and readily available. The technology is more mature and there has recently been demand for the optimization and reliability improvement of small ICEs for use on UAS platforms [11]. A hybrid electric power system consists of a diesel or gasoline ICE working in combination with a battery. There are other components involved in this hybrid system, such as a generator or clutch, depending on the configuration. These components, along with the required fuel supply, add dead weight to a system that can present a challenge when implementing on smaller UAS platforms.

2.2 Power System Configurations

The two main configurations of hybrid-electric power systems are series and parallel (Figure 2).

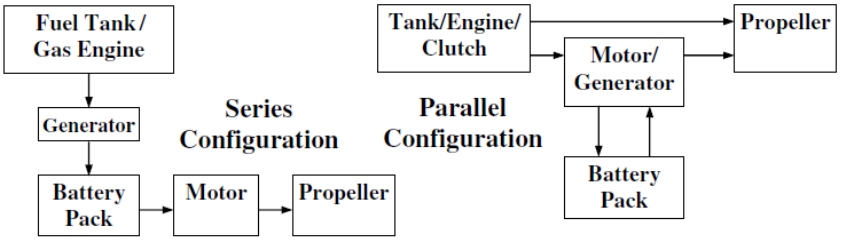

Figure 2: Series and parallel hybrid-electric power system configurations[12]

The series configuration consists of an ICE in-line with a generator that produces current to charge the battery. The battery then discharges to the electric motors, which drive the propellers. This configuration is subject to losses through the ICE and generator, and is restricted by the charge rate of the standard battery, which is typically an order of magnitude smaller than the discharge rate. The parallel configuration consists of an ICE that can directly drive the propellers and/or charge the battery through a generator, while the battery also has a direct line to the propeller. This configuration allows for multiple operating states depending on the requirements and conditions at any given time. While the series configuration is mechanically simpler than the parallel configuration, it is also considered to be ideal for high-torque, low-speed applications. An additional configuration for hybrid power systems is an electric-parallel system (Figure 3), which consists of an ICE which drives an alternator, producing the main supply of electrical power, as well as a backup battery which can be recharged by the alternator output or discharged to supply additional power instantaneously.

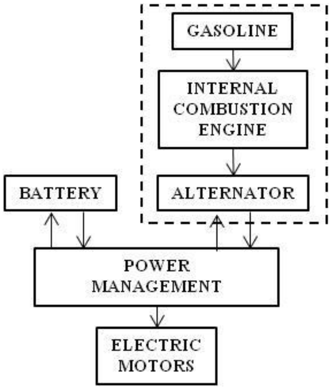

Figure 3: Electric-parallel hybrid power system block diagram (specific to gasoline ICE)

In preparation for this study, studies that have explored the potential benefits of hybrid systems were reviewed. One such study used MATLAB Simulink simulation models to predict the behavior of a fixed-wing aircraft with a parallel hybrid-electric propulsion system, specifically during a ISR (intelligence, surveillance, and reconnaissance) mission, and to compare this performance to that of the same system propelled by only an ICE [13]. The conclusion from this study was that during a 1-hour ISR mission with the selected physical components under the given conditions, a 54% energy savings was seen with the hybrid-electric propulsion system, and for a 3-hour ISR mission, a 22% energy savings (given in kWh) was seen. The flight plan for both missions included takeoff, climb, cruise, endurance speed, high speed dash, descent, and landing. Another similar study also used MATLAB Simulink to develop models for a parallel hybrid-electric propulsion system and gasoline-only propulsion system, both implemented on a fixed-wing aircraft [14]. The conclusion from this study was that during an approximately 10 minute flight consisting of climb, cruise, descent, and loiter (repeated once), a fuel savings of 6.5% was seen.

2.3 Integration Challenges

Hybrids have shown promise for fixed-wing UAS, and implementation of these types of power systems is being pursued [15], but there has been limited published exploration of hybrid-electric power systems for multi-rotor UAS. One of the most important design challenges when considering the addition of a hybrid power system that utilizes a mechanical power source such as a gasoline ICE is physical integration with an existing dynamic system. Some major considerations include vibration, cooling, and noise. The purpose of this study is to conduct analysis of some of these major integration challenges in an effort to further establish the true viability of hybrid-electric power systems for multi-rotor aircraft. Vibration is considered a major integration challenge due to its potential effects on the stability and function of the aircraft, and its on-board sensors. While vibration is present on standard multi-rotor UAS, the potential for the additional vibration signature of an internal combustion engine to be detrimental to the function of the aircraft and its on-board sensors must be considered.

Studies have been conducted which help to characterize combustion engine vibration and isolate the individual components which contribute to the overall signature. It has been shown that the motion of the piston caused by the combustion, a major contributing source of vibration, actually contributes different vibration behavior than the combustion itself, which creates an affect called combustion knock [16]. There are a variety of different contributing factors to combustion engine noise, each which contribute a different component of the overall vibration signature. Jin explains that the steady, cyclic motions of the engine such as the cam rotation, produce a continuous vibration component that is related to the RPM of the engine during operation [17]. It is also noted in his work, and elaborated on in other publications, that more transient components of the vibration signature can be caused by gas pressure pulsation, cylinder pressure fluctuation caused by combustion, and other interactions between internal engine components [18].

Cooling requirements of a small internal combustion engine is also considered to be a major integration challenge due to the hover capabilities of multi-rotor UAS. On fixed wing aircraft the engine is air-cooled by the forced convection from the free-stream velocity, however multi-rotor UAS cannot necessarily provide the same forced convection during flight. For a hybrid-electric multi-rotor UAS to be able to utilize all of its unique functions, it must be determined whether or not a small internal combustion engine could be effectively cooled by some additional source of forced convection, or a water-cooled system. An air-cooling system has the potential to be lighter-weight than a water-cooling system, but the effectiveness of an air-cooling system is limited by the amount of airflow it can produce.

Last but not least, noise is also considered a major integration challenge. For the small 2-stroke ICEs being considered in this study, there are two main components of the noise signature: mechanical noise and combustion-related noise. Mechanical noise refers to noise produced by the mechanical interactions of the engine, the sources of which include some of the vibration sources discussed above. For combustion-related noise, both intake and exhaust act as outlets for the combustion noise and are primary contributors to the overall noise signature. With projects for which detection and avoidance is a critical consideration, it is important to understand how a small internal combustion engine would affect the existing noise signature of a multi-rotor UAS. Noise can also be critical in other scenarios, such as for the simple annoyance factor of the aircraft when it is in hearing range of populated areas.

2.4 Potential Endurance Benefits

As discussed in Power System Configurations, an electric-parallel hybrid power system requires a mechanical power source (internal combustion engine) and an alternator to convert the mechanical power into electrical. When selecting a compatible set of engines and alternators, it is important to consider the power output of the engine, the efficient operating range of the engine, and how those values align with the RPM required to produce a given amount of power for the available alternators. With these considerations in mind, there is a finite number of effective engine/alternator pairs which can be considered for hybrid power systems. For UAS on the size scale of from the DJI S1000 to the Gryphon X8 and larger, several small combustion engines are available for mechanical energy production. Options for alternators with compatible energy conversion capabilities are more limited, however. The main producer of alternators design for use on UAS is Sullivan Unmanned Vehicle, and Table 1 shows several potential combinations of small combustion engines with those available alternators. The potential electrical power given for each of these combinations is an estimate of the electrical power that the hybrid system could supply. This estimate accounts for approximate power transmission losses as well as what power the alternator can provide at the chosen operating point for each engine (alternator power curves can be found in the Appendix).

Table 1: Power system sizing

Source	Mechanical Power (HP)	Optimal RPM	Compatible Alternator	Potential Electrical Power (W)
DA 35 DLE35RA	~4.0	7000	S676-400U-01	1200
DLE40	4.8	6000	S676-500U-01	1800
DA 50	5	6500	S676-500U-21	2250
DA 70	7	6000	S676-550U-01	3000
DA 100	10	5500	S676-600F-01	3500

There are several currently available COTS UAS platforms the power requirements of which could potentially be supplied by hybrid-electric power system solutions. A few of these that fall in the power supply range shown in Table 1 include the DJI S1000 [19], DJI M600 [20], and Gryphon Dynamics GD-28X [21]. These are shown in Table 2 along with their empty weight (no batteries) and the power requirements at hover for a specified GTOW.

Table 2: COTS platforms with potential for hybrid-electric conversion

Platform	Empty Weight	Power Required at Hover
S1000	8.8 lbs	1500 W @ 21 lbs
M600	12.2 lbs	2250 W @ 33 lbs
Gryphon GD-28X	26.4 lbs	3320 W @ 70.5 lbs

Power management is another major consideration when sizing these systems. The alternators produce an AC voltage that must be regulated to a stable DC voltage in order to directly power the electric motors and charge the backup battery (if necessary). Sullivan Unmanned Vehicle also offers a hybrid PMU (power management unit) which can handle all the necessary operations. Table 3 shows four potential power supply cases, and for each, the system weight factors in the weight of the engine, its compatible alternator, and the PMU discussed above. The batteries chosen for this comparison are 22.2V (6s) 11,000mAh LiPo batteries [22].

Table 3: Cases for comparison of hybrid-electric and battery-only endurance potential

Case	Engine	Hybrid System Weight (lbs)	Fuel Weight (lbs)	# of Batteries	Battery Weight (lbs)	Total Battery Capacity (Ah)
A	DA35	6.74	4.46	4	11.2	44
B	DLE40	7.26	6.74	5	14	55
C	DLE40	7.26	9.54	6	16.8	66
D	DA50	8.19	11.41	7	19.6	77

For each of these cases, calculations are done to determine the amount of time that each type of supply in each case could power a theoretical platform with an empty weight of 15 lbs, equipped with 8 KDE Direct 435 Kv electric motors with 18.5" dual-blade propellers for propulsion. These calculations are done using the provided data sheets for these motors to determine that power required for varying takeoff weights assuming a 22.2V system (6s) [23]. For example, with a power system weight of 11.2 lbs (Case A), the takeoff weight of the platform is 26.2 lbs. The power required for eight of the chosen motors to produce 26.2 lbs of thrust is approximately 1200 Watts. For a 22.2V system, this indicates a constant current draw of 54 amps. Equation **1** is used to calculate the time that the battery would be able to supply this required current for, based on the rated battery capacity, where t_f is flight time in minutes, I is current draw in amps, and C is battery capacity in amp hours.

$$t_f = \left(\frac{60 * C}{I}\right) \tag{1}$$

Equation 2 is used to calculate the amount of time that the engine would be able to supply power based on the approximate fuel consumption rate and the amount of fuel that can be carried to match the weight o the battery-only power system. w is the amount of fuel in ounces and f is the fuel consumption rate in ounces per minute.

$$t_f = w/f \tag{2}$$

Figure 4 summarizes these calculations.

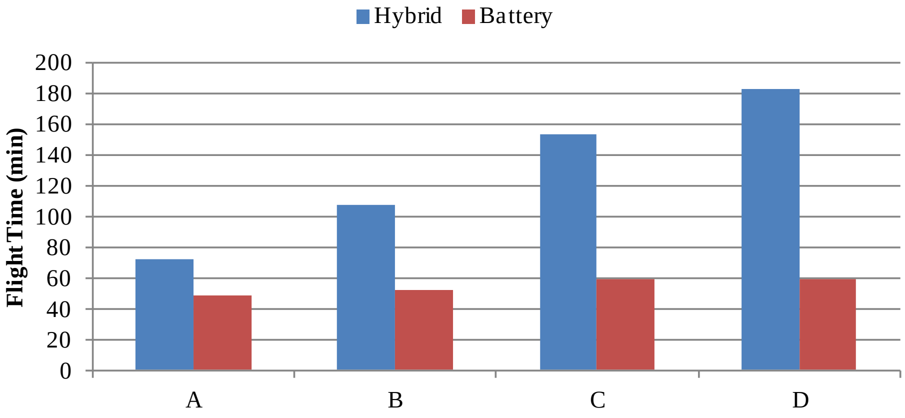

Figure 4: Comparison of hybrid-electric and battery-only with four different power supply designs.

These preliminary results show that a hybrid power system that is appropriately sized to supply the full power draw of a COTS multi-rotor UAS platform can potentially supply power for longer than a traditional LiPo supply of approximately equivalent weight. This comparison was done for four different power system weights in increasing order, with the power system weight for the hybrid being system weight and fuel. With increasing GTOW (power system weight plus platform weight), the power draw increases, and therefore the engine size must also increase, but any remaining difference between the battery weight and hybrid weight is fuel allowance. As seen in Table 3, the amount of fuel being carried continues to increase, as well as the battery capacity, but the battery flight time barely increases over the four cases while the hybrid flight time consistently increases. This indicates that a hybrid power system would potentially not be limited by the affect of diminishing returns in the way that the LiPo battery supplies are. Because the hybrid power system has proven to supply more power, the implications of actually integrating such a system on a multi-rotor platform will be investigated.

CHAPTER III

EXPERIMENTAL SETUP

The major challenges for a integrating a hybrid-electric power system of a multi-rotor UAS platform have been identified as vibration, cooling, and noise. In order to explore these integration challenges, several experimental setups have been developed from which vibration, thermal, and acoustic data will be extracted from various test articles. The main test article is a 50cc two-stroke gasoline engine, the DA50, chosen to be a representative of the type and scale of mechanical power source that could be utilized in a hybrid power system for multi-rotor aircraft. When it became necessary in vibration and noise experiments to isolate certain behaviors of the engine from the propeller used to load it, an electric motor capable of supplying the same mechanical power was used with the same propeller. The same electric motor was also used in attempts to replicate the engine vibration due to the similar mass and RPM range.

A variety of instrumentation was used with the test setups explained in this chapter to collect the necessary data, including accelerometers for vibration measurement and microphones for acoustic measurements.

3.1 Technical Approach

The ultimate goal of this work is to characterize the challenges that must be addressed when designing a hybrid power system (as described in Chapter 2) for a multi-rotor UAS. This overall goal has been divided into individual experimental goals for the three major challenges previously identified: vibration, cooling, and noise.

3.1.1 Vibration

When considering vibration, the goal is to gain a preliminary understanding of the potential issues of adding the vibrations of a hybrid power system utilizing a gasoline ICE to a multi-rotor UAS, before diving into the design process of a fully functional system. The first stage of this process will be to characterize the vibration signature of the DA50 on a test stand by measuring the oscillating acceleration produced by the engine during operation. The next stage is to design a simple system that can replicate the vibrations of the engine and be easily integrated with an existing multi-rotor platform. An electric motor of similar mass and power output to the engine will be used to drive an unbalanced cam designed to produce the same magnitude of vibrations at the same frequency. The final stage of this testing will be mount that simple system to a battery-powered COTS multi-rotor aircraft, and conduct flight testing to observe any affect that the added vibration may have on the mission capabilities of the aircraft. These stages have been detailed in Figure 5, which will be referred back to frequently during the explanation of the experimental setups and results.

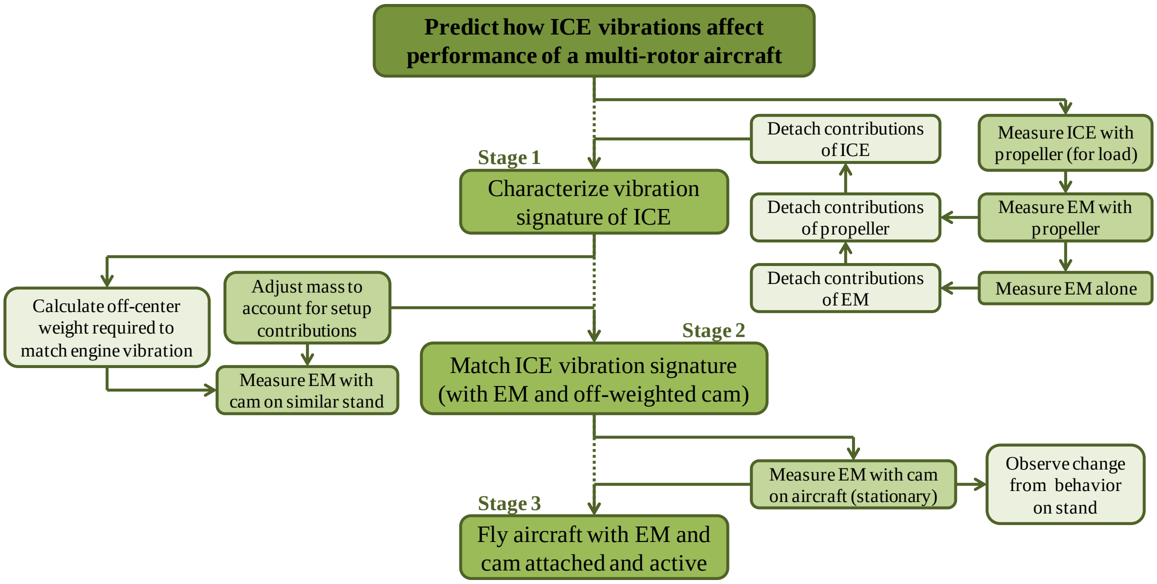

Figure 5: Testing goals for vibration, divided into three stages

3.1.2 Cooling

When considering cooling, the goal is to gain a preliminary understanding of the additional cooling (other than ambient air) required for a hybrid power system utilizing a gasoline ICE, before diving into the design process of a fully functional system. The thermal behavior of the sample engine (DA50) will be observed with a propeller as a load (and also a cooling source) to determine whether or not additional cooling is required. Calculations will also be made to predict the required cooling under different loads. Finally, the original hybrid endurance boost estimates made in Chapter 2 will be used to estimate the weight and power design margins for designing potential cooling systems.

3.1.3 Noise

When considering noise, the goal is to gain a preliminary understanding of how the noise signature of a hybrid power system utilizing a gasoline ICE would affect the existing noise signature of a multi-rotor UAS. The first stage towards this goal is to measure the acoustic signature of the sample engine (DA50) with a propeller as a load. An electric motor with similar a similar power range will be used to drive the same propeller, and the acoustic signature of this will be used to isolate the engine's contribution from the propeller's contribution. The next stage is to measure the acoustic signature of a multi-rotor aircraft that is determine to be of the correct scale and power draw to be compatible with a hybrid power system utilizing the DA50 engine. The third stage is to use analytical methods to isolate the engine signature from other contributing signatures (propeller, ambient, etc.), correct for any differences in measurement distance, and combine it with the aircraft signature. The resulting combined signature can then be compared to the aircraft by itself, and conclusions can be drawn about the effect that adding a hybrid power system would have on the noise signature of a multi-rotor aircraft. These testing stages have been detailed in Figure 6, which will be referred back to frequently during the explanation of the experimental setups and results.

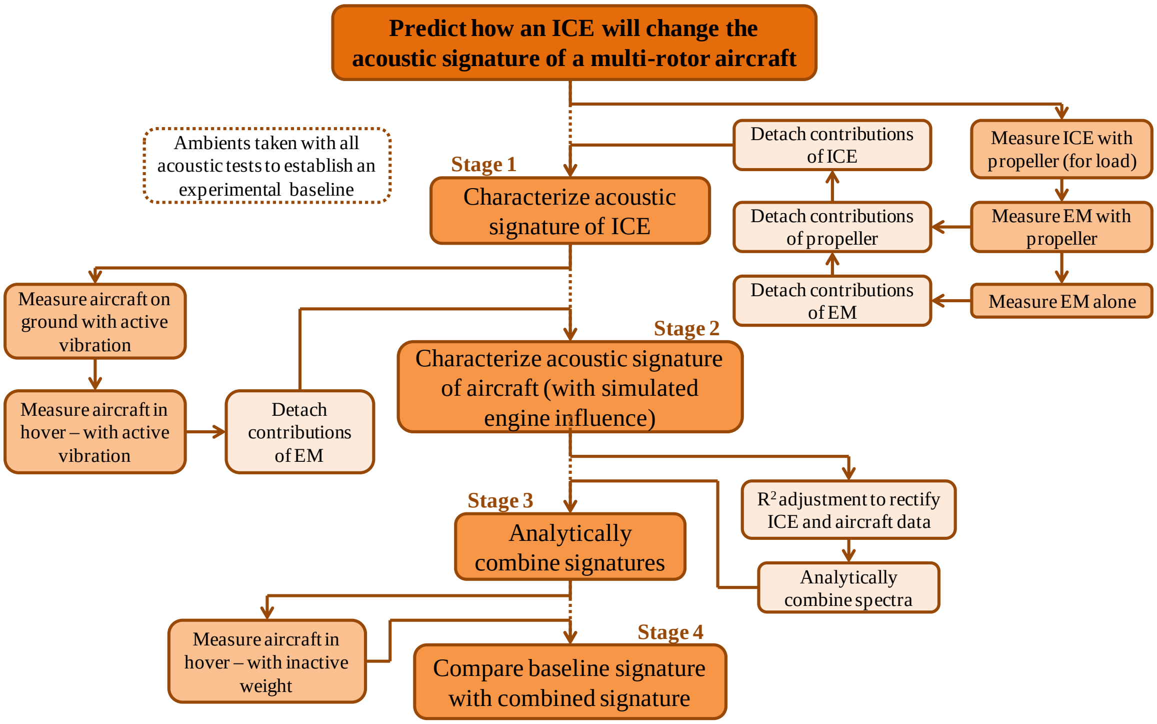

Figure 6: Testing goals for noise, divided into three stages

3.2 Engine Test Stand

The combustion engine chosen for experimentation is the Desert Aircraft 50cc engine (details in Appendix, Figure 88). In order to break in and test the engine, a stationary test stand (Figure 7) was built which would fix the engine in its upright position, allow airflow to the carburetor, and provide mounting surfaces for necessary sensors and actuators. A wooden 23x8 Xoar propeller is used to load the engine and provide cooling airflow to the cylinder head during this static testing. The test stand is equipped with a magnetic RPM sensor, and the engine is run with the recommended 50:1 gas-oil mix. A temperature loop sensor is tightened around the top fin of the cylinder head, where the highest temperatures are expected due to the combustion in the piston chamber. Ducting is routed from the outlet of the engine muffler to the lab's exhaust removal system which applies a negative pressure to draw the exhaust gasses from the testing area.

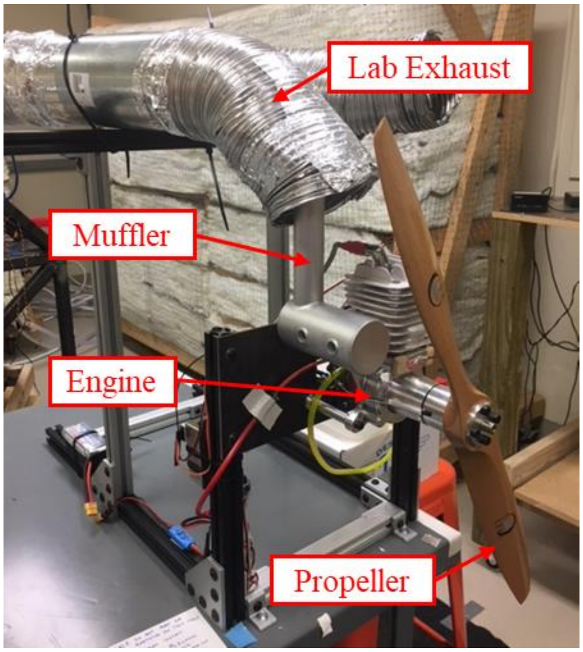

Figure 7: Engine test stand configuration

The engine is mounted to the stand with neoprene dampeners to allow the engine to move more freely. The engine is fixed at four points using the stock aluminum standoffs. Each dampener has a rated capacity of 31 lbs and a rated shear capacity of 4.5 lbs. The rated deflection at capacity is 0.07" and the rated shear deflection at capacity is 0.06".

3.3 Electric Motor Test Stand

The electric motor chosen for comparison testing is the Turnigy Rotomax 50cc, which has a similar mass (1.08kg) and mechanical power output to the engine. This brushless, outrunner motor has a KV rating of 172, so it is run on a 12s (44.4V) system to be able to consistently supply power at and above 6000 RPM. Multiple different test stand configurations were considered for testing the electric motor while closely replicating the conditions that the engine was tested with. Figure 8 shows the three different structural configurations used.

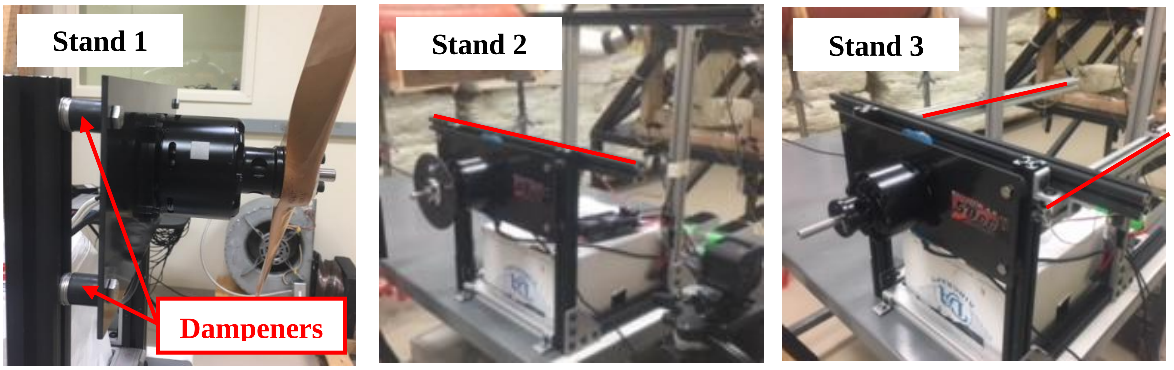

Figure 8: Different stand configurations considered for vibration replication testing.

Two different dampeners were also considered and tested. Dampener A is the same dampener used for the engine, while Dampener B has a rated capacity of 75 lbs and a rated shear capacity of 25 lbs. The rated deflection at capacity is 0.03" and the rated shear deflection at capacity is 0.1". Additional specifications for both dampeners can be found in the Appendix (Table 20). Comparison testing is conducted with the different test stand configurations and the two different dampeners. The results are shown in Table 4. For the test with Stand 1 and Dampener A, a full test was not able to be completed due to the dampeners failing.

Table 4: Vibration Half-Amplitude (g) Produced by Cam

m = 0.36 oz, r = 1.5 in

Approx. RPM	**Stand 1**	**Stand 2**	**Stand 2**	**Stand 3**	**Calculated**
	Dampener A	**Dampener A**	**Dampener B**	**Dampener B**	
3800	11.7	SAT	7.5	2.7	5.8
4600	12.4	14	SAT	5.7	8.5
5600	---	10.5	SAT	SAT	12.6
6000	---	7.5	SAT	SAT	14.5

As can be seen in Table 4, any changes to the physical characteristics of the test media can greatly affect the measurement of the vibration signature being produced. Due to the fact that all components (source and media) are coupled, and therefore behave as a whole, the measured vibration signature does not necessarily represent what is being produced by the source alone. This means that the experimental process detailed here cannot perfectly replicate the vibrations produced by a 2-stroke ICE. One of the goals of this work is to determine how strong vibrations, similar to those produced by a 2-stroke ICE, would affect the mission capabilities of a multi-rotor aircraft. Therefore this experimental process is designed to control as many parameters as possible (such as sensor accuracy) while accepting the inherent limitations of the measurements being made.

While preliminary vibration replications efforts were conducted with Stand 1 and Dampener A, at the conclusion of this experimentation, it was decided that Test Stand 2 with Dampener B would be used for the ongoing replication efforts. Stand 2 is believed to most closely physically represent the engine test stand, and the larger dampeners are required for conducting the replication tests without risk of structural failure (due to the sometimes heavily amplified vibrations).

3.4 Instrumentation

3.4.1 Vibration

To measure frequency and estimate magnitude of vibration produced by the engine at varying RPM, a 3-axis accelerometer (the VectorNav VN100) was rigidly mounted with epoxy to a safe mounting location on the engine (Figure 9). The VN100 has a measurement range of +-16g with a maximum sampling rate of 200Hz. Temperature was monitored at several possible locations during preliminary engine tests, and the chosen location (on the bottom of the crank case) was found to provide the safest operating conditions for the accelerometer, which has a maximum operating temperature of 185˚F. The coordinate system of the sensor is shown in Figure 9. The piston travels within the Z axis, therefore vibration in this axis is expected to be caused by the combustion and motion of the piston. The rotational plane of the crank contains the Z and Y axes, therefore vibrations in the Y axis are expected to be caused by the motion of the crank. However, these vibrations are expected to be relatively small. The thrust produced by the propeller acts in the X axis, therefore vibrations in this axis are expected to be caused by variation in the amount of thrust produced at each time step.

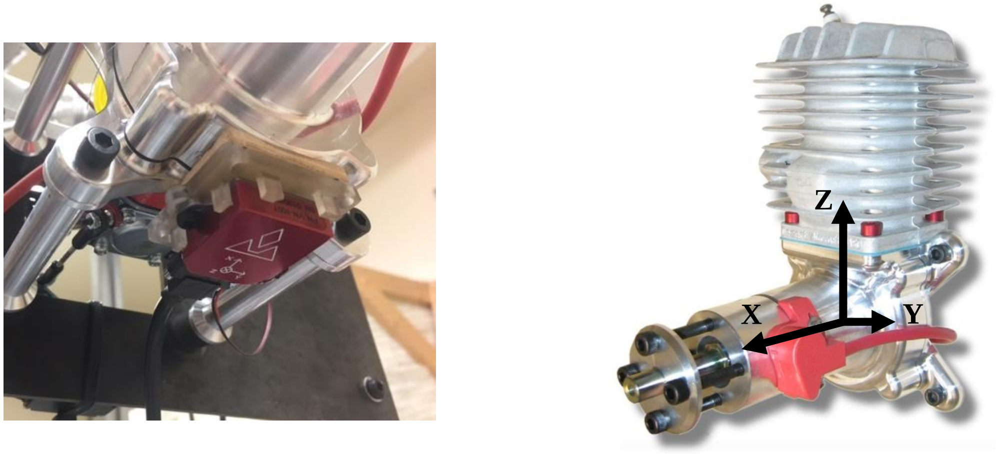

Figure 9: Accelerometer orientation and measurement coordinate system for engine tests

Figure 10 shows the same sensor mounted to the electric motor test stand, directly below where the electric motor is attached.

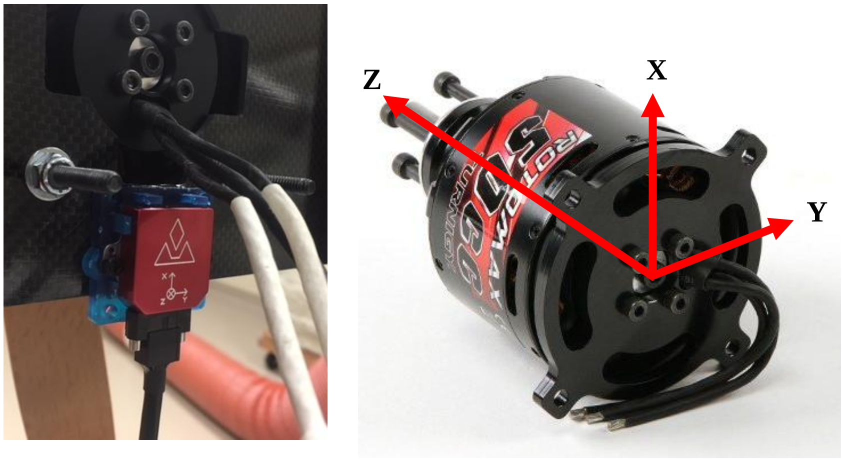

Figure 10: VN100 accelerometer orientation and measurement coordinate system for electric motor tests

Due to the different mounting orientation of the accelerometer in the electric motor testing, it should be noted that the Z axis in the engine data corresponds to the X axis in the electric motor data, and in both of these axes the additional acceleration due to gravity must be corrected for in order to observe only the acceleration due to the motion of the engine/electric motor. Likewise the X axis in the engine data corresponds to the Z axis in the electric motor data, and the Y axes are equivalent.

To provide a larger range of measureable data frequencies, the Variense VMU931 is also used for vibration measurement. This sensor has a measurement range of +-16g and a maximum sampling frequency of 1000Hz. This sensor has a maximum operating temperature of 104˚F, so the placement of this sensor on various test setups is also carefully chosen with temperature as a consideration.

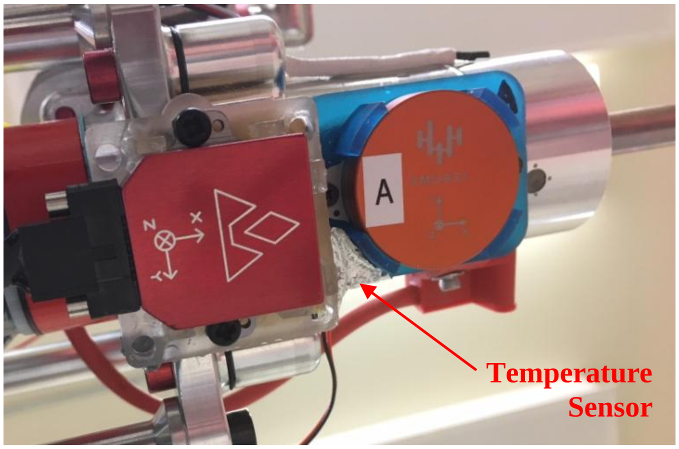

Figure 11: Placement of VN100 and VMU931 on engine, chosen based on areas of the engine which stay below sensor safe operating temperatures during engine operation.

Figure 11 shows the placement of the both accelerometers on the engine, while Figure 12 shows the placement of the VMU931 on the electric motor test stand. In both cases, the sensor is rigidly mounted with epoxy as close as possible to the center of mass of the test article being measured.

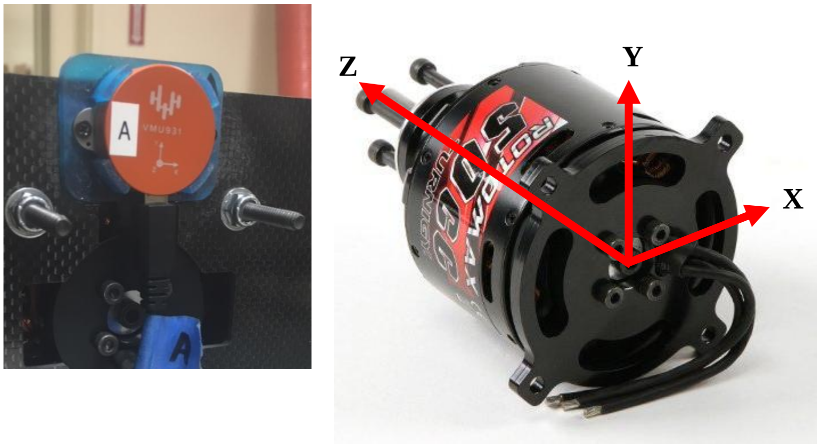

Figure 12: VMU931 accelerometer orientation and measurement coordinate system for electric motor tests

3.4.2 Cooling

The instrumentation used for data thermal data collection is two different types of temperature sensors, both designed for use with the Eagle Tree eLogger V4 (data logger). One is a temperature loop sensor, used to monitor the temperature of the engine cylinder head, and the other is a single-point temperature sensor used to monitor several locations on the engine.

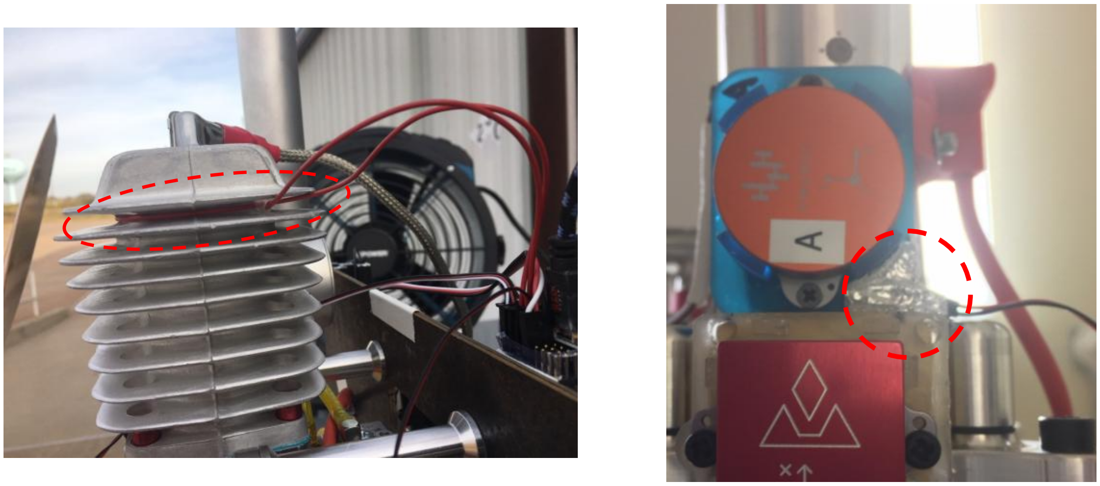

Figure 13: Placement of EagleTree temperature sensors used during engine testing.

3.4.3 Noise

All acoustic data is collected with G.R.A.S. 1/2-inch pre-polarized microphones with G.R.A.S. 1/2-inch CCP pre-amplifiers. Table 5 and Table 6 show the relevant specifications of this hardware.

Table 5: Microphone Specifications

	1/2" Prepolarized Pressure Microphone
Frequency Range (+-2dB)	3.15 Hz - 10 kHz
Dynamic Range (w. CCP Preamp)	18 dB(A) - 138 dB(A)
Sensitivity (250Hz, +-2dB)	50 mV/Pa
Resonance Frequency	14 kHz

Table 6: Preamplifier Specifications

	1/2" CCP Preamplifier
Frequency Range (+-0.2dB)	2.5 Hz - 200 kHz
Typical Noise	3.5 μV (typ.)
Gain	-0.30 dB

National Instruments' NI USB-4431 DAQ is used for data collection, and all data is collected using the NI Signal Express Software (Table 7).

Table 7: DAQ Specifications

	NI USB-4431
Sampling Range	102.4 kS/s
Sampling Resolution	≤2.10 mS/s
Dynamic Range (1kHz, 102.4kS/s)	100 dB (typ)
Amplitude Accuracy (-30C to 70C)	AC @ 1kHz: +-0.052 dB DC: +-0.5%

3.5 Tests

3.5.1 Vibration

During initial testing, the engine was throttled through seven phases and allowed to settle in each phase while acceleration data was recorded. The seven phases, selected based on throttle position, are shown in Table 8. The data from each full test is separated into each individual phase for graphing and processing such as frequency analysis.

Table 8: Vibration testing throttle phases

Phase	Approximate Servo Position	Average RPM
1	20%	3000
2	25%	3800
3	35%	4600
4	45%	5600
5	50%	6250
6	75%	6400
7	100%	6500

The frequency of vibration oscillations in each phase is governed by Equation 3:

$$frequency = \frac{rev}{min} * \frac{1\ min}{60\ sec} \tag{3}$$

To obtain a baseline comparison point for the engine vibration measurements, a second set of tests is conducted with the same accelerometer (VN100), mounted as shown in Figure 10, to collect data while running the Turnigy RotoMax 50cc-size brushless motor with the same 23x8 wooden propeller. This electric motor supplies comparable power to the DA50 but potentially with limited vibration and noise. To as closely replicate the previous setup as possible, the electric motor is mounted as shown in Figure 8 with the same dampeners used in the previous tests, and the same RPM phases are used (Table 8).

Based on the rotating imbalance dynamics shown in Figure 14, the off-center mass (m) and radius (e) required to produce the same magnitude of vibrations as that measured from the engine can be calculated using the equation below. The RPM will be the same as the operating point of interest for the engine (6000 RPM) so that the frequency of the vibration is the same.

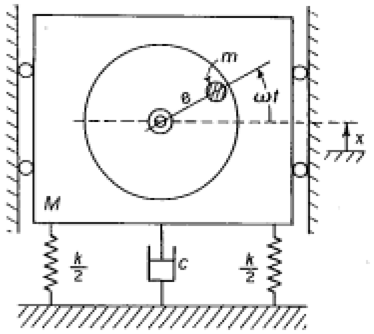

Figure 14: Theoretical system dynamics for rotating imbalance[24]

Equation 4 is used to calculate the mass required at a given radius from center e, at a given frequency ω. F is the force created by the off-center weight, which is calculated by the mass of the oscillating object (engine) and the acceleration.

$$F = me\omega^2 \tag{4}$$

Based on initial calculations, a simple adjustable cam (Figure 15) is designed which allows for variation in radius and mass for experimental adjustment.

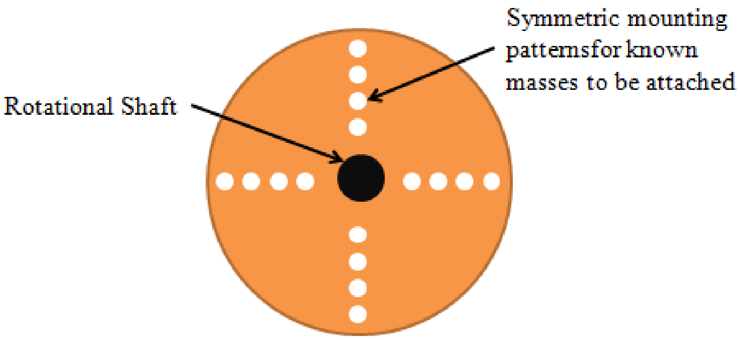

Figure 15: Basic design used for adjustable cam for which the off-center mass and radius can be changed to experimentally adjust vibrations produced during testing.

This cam design is tested by attaching it to the electric motor, and running it at multiple RPM on the test stand discussed on page 20, and the appropriate mass or radius adjustments are made before the vibration system is mounted to an sUAS for flight testing. The DJI M600 is chosen as the test sUAS platform due to its size and payload capacity, which allow for easy integration of the necessary hardware and electronics for operating the electric motor (schematic shown in Appendix, Figure 92).

Flight-testing was conducted at the OSU Unmanned Aircraft Flight Station from 8:00am to 9:30am on December 12th, 2017. DJI Go was chosen as the mission planning software, and flights were conducted both with and without the electric motor running. Communications with the electric motor are separate from the communications with the aircraft, with an independent receiver and transmitter. In order to simplify the payload design, the RPM of the attached electric motor is set on the ground, and then maintained throughout test flight. Three types of flight paths were planned (rectangular, point-to-point, and orbit) in order to observe if different dynamic maneuvers during flight changed how the vibration affected the platform, if at all. Due to electrical connection malfunctions only the rectangular flight path was successfully executed.

The first flight, with the motor off, was used to set the waypoints in the mission planner. Once the points were set, the rectangular flight path was executed with the electric motor off. Upon completion of this flight, a second flight was conducted with the same set of waypoints, and the electric motor operating at approximately 5700 RPM. The RPM was set using a measurement of the acoustic signature during motor operation and manual identification of the peak attributed to the motor noise. All flights were flown at an altitude of 15m.

Flight testing was repeated at the OSU Unmanned Aircraft Flight Station in March with a new cam design (Figure 16) in March 2018. The weather data for these flight tests can be found in the Appendix, Table 18.

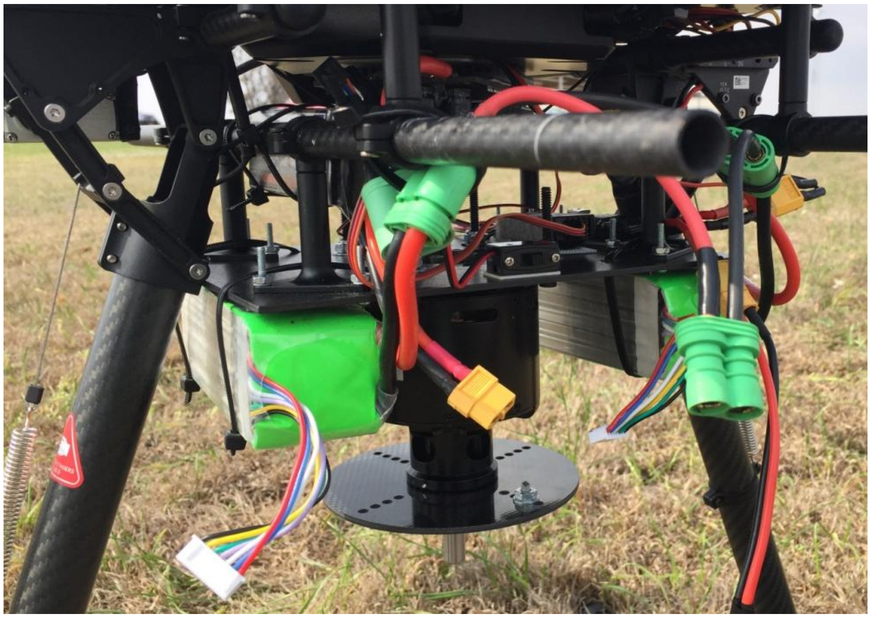

Figure 16: Electric Motor with unbalanced cam mounted to M600 for flight testing (March 2018)

DJI Ground Station Pro was chosen as the mission planning software, and flights were conducted both with and without the electric motor running. As with the previous vibration replication flights, communications with the electric motor are separate from the communications with the aircraft, with an independent receiver and transmitter, and the RPM of the attached electric motor is set on the ground before takeoff. Once again, three types of flight paths were planned (rectangular, point-to-point, and orbit) as shown in Figure 17.

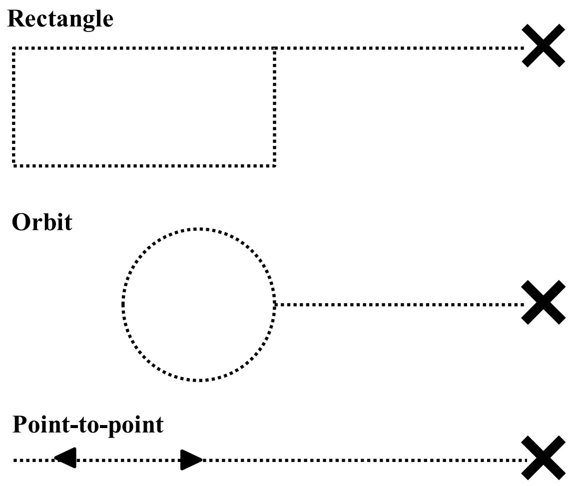

Figure 17: Flight paths used for all vibration replication comparison flights.

3.5.2 Cooling

Steady-state temperature tests were conducted to observe the thermal behavior of the engine at different power outputs with the active cooling flow provided by a 23x8 wooden propeller, which was also the source of loading for the engine. Predictive cooling calculations were also made to show the theoretical cooling requirements for a variety of power outputs of the same engine.

3.5.3 Noise

Initial measurements of the noise signature produce by the engine are taken in a lab setting on the engine test stand (Figure 7). Two G.R.A.S. 1/2-inch pre-polarized microphones with G.R.A.S. 1/2-inch CCP pre-amplifiers are placed as shown in Figure 18 to collect data while running the engine with a 23x8 wooden propeller. The microphone orientations are chosen to be in-plane with the propeller, and 90° relative to the propeller plane. The engine is mounted in the same configuration (Figure 7), and running at the same operating points (Table 8) used in vibration tests.

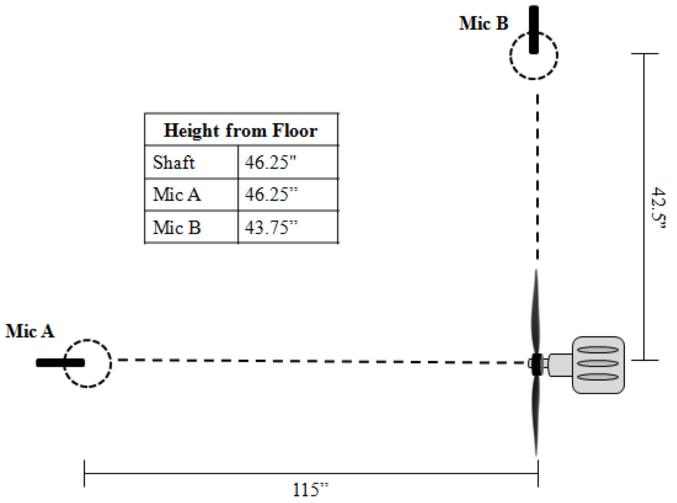

Height from Floor	
Shaft	46.25"
Mic A	46.25"
Mic B	43.75"

Figure 18: Microphone array for acoustic measurements of DA50 with 23x8 wooden propeller

To isolate the engine signature from the noise produced by the propeller, a second set of tests is conducted with the same two microphones placed in the same configuration shown in Figure 18 to collect data while running the Turnigy RotoMax 50cc-size brushless motor with the same 23x8 wooden propeller (Figure 10) on the electric motor Stand 1 (Figure 8). This electric motor supplies comparable power to the DA50 but with potentially limited vibration and noise. To further differentiate between the components of the noise signature that are contributed by the propeller and the electric motor, additional data is taken with the electric motor running without the propeller at the same operating points.

Before recording acoustic data with the engine and electric motor running, ambient measurements are taken with the lab exhaust removal system active. This ambient data, the data from the engine tests, and the electric motor data with and without the propeller is processed, and the acoustic data from the electric motor tests is used to help identify which components of the overall noise signature can be attributed to the engine.

To better assess the acoustic signature of the engine, outdoor tests were conducted in March 2018 to allow measurement in the geometric far-field of the engine. This was accomplished by spacing the microphones more than 125 times the diameter of the exhaust port away from the engine [25]. This testing was conducted with the engine test stand (Figure 7) and the electric motor test stand discussed on page 20. Due to the propeller being used to load the engine during this acoustic testing, the microphone spacing is also based on the geometric far-field of the propeller, which can be estimated as 10 times the propeller diameter[26]. To achieve the most quiet ambient environment possible, this testing was conducted from 10pm to 5am. The weather data for this testing can be found in the Appendix, Table 19.

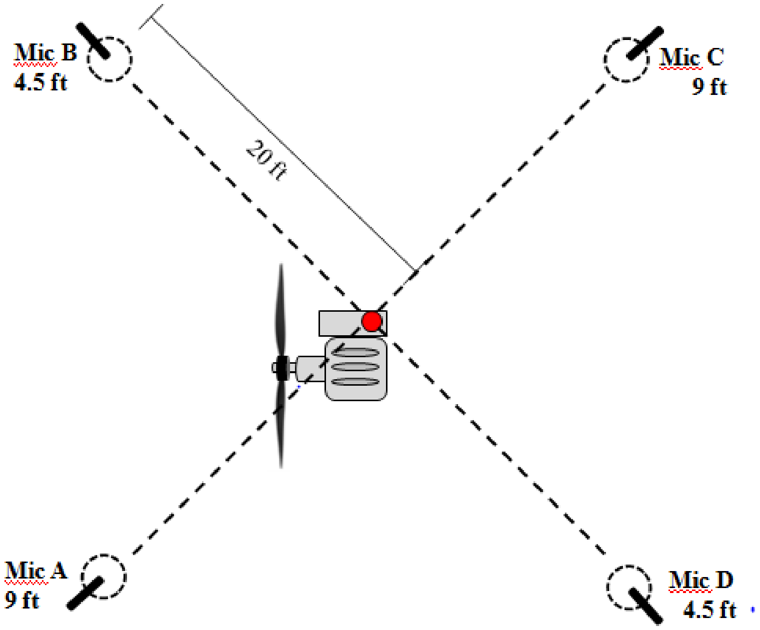

Figure 19: Microphone orientation and placement for outdoor engine far-field testing.

Acoustic data was collected for two different aircraft of interest. The DJI M600 was measured as a compatible aircraft for the DA50 engine, and its corresponding theoretical hybrid power system. Acoustic data is collected while this aircraft hovered ~30 ft above a 20ft radius microphone array, as shown in Figure 20. The weather data for these flight tests can be found in the Appendix, Table 18.

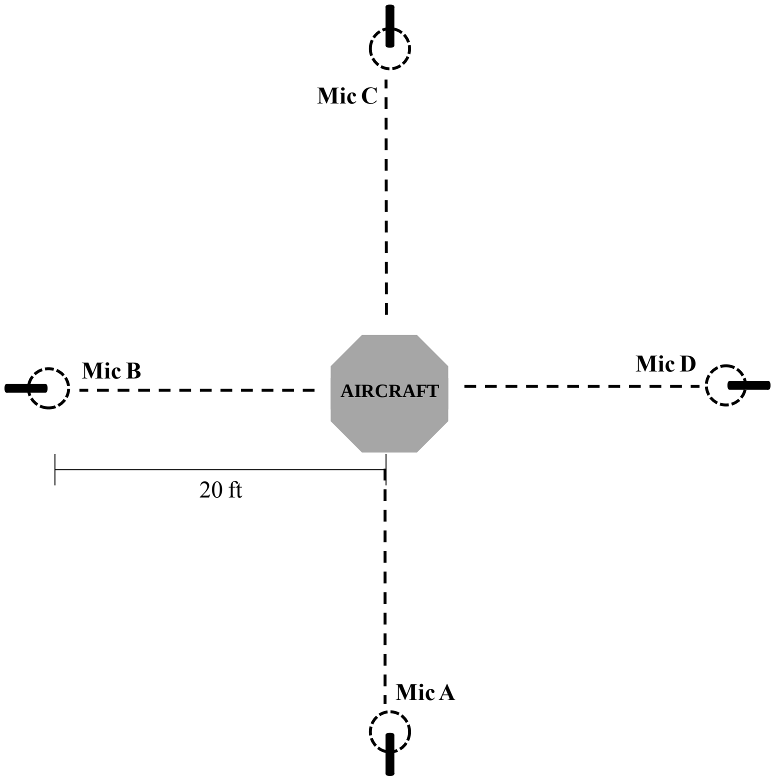

Figure 20: Microphone orientation and placement for acoustic data collecting during flight for multi-rotor aircraft.

To visualize the acoustic impact that a small 2-stroke engine would have on a multi-rotor aircraft, an analytical approach based on the basic concepts of noise propagation (Equation 5) was taken to process the data from the M600 f lights and the outdoor measurements of the engine.

$$SPL = 10\log\left(\frac{{P_{RMS}}^2}{{P_{ref}}^2}\right) \qquad 5$$

First, the ambient, electric motor, and propeller contributions are removed from the engine spectra, leaving what we will assume is a good estimation of the engine's independent contribution using Equation 6.

$$SPL_2 - SPL_1 = 10\log\left(\frac{{P_{RMS(2)}}^2/{P_{ref}}^2}{{P_{RMS(1)}}^2/{P_{ref}}^2}\right) \quad 6$$

The engine data is then corrected for the difference in measurement distance. The M600 was at the center of a 20ft radius microphone array, hovering 30ft above the microphones, making the direct distance approximately 36ft. The engine is therefore corrected by approximately -5dB to estimate how it would sound if it were also measured from 36ft instead of 20ft (Equation 7).

$$SPL_{36ft} = SPL_{20ft} + 10\log\left(\frac{(20)^2}{(36)^2}\right) \quad 7$$

The M600 data is adjusted to a bandwidth of 2Hz (originally 1Hz) to match that of the engine data by using Equation 8 to combine the SPL every two frequencies, and finally, the two resulting spectra (engine only and M600 in hover) are added (Equation 8).

$$SPL_2 + SPL_1 = 10\log\left(\frac{{P_{RMS(2)}}^2}{{P_{ref}}^2} + \frac{{P_{RMS(1)}}^2}{{P_{ref}}^2}\right) \quad 8$$

All the equations discussed above were taken or derived from Ruijgrok [27].

3.6 Overall Bias Error

Overall bias error considers all contributing instrumentation errors, including sensors, wiring, electronics, etc. The sensors and electronics used for vibration and temperature data collection did not have published error data, and so are not discussed here. Equation 9 [28] describes the method for calculating an overall bias for a combination of component errors, where u is each contributing error.

$$Total\ Bias = \sqrt{\sum (u)^2} \quad 9$$

This overall bias calculation was conducted for the acoustic data collection equipment, and the results are shown in Table 9.

Table 9: Bias Error for Microphone Measurements

40AD 1/2" Pre-polarized Microphone	±2 dB
26 CA 1/2" CCP Preamplifier	±0.2 dB
NI USB 4431	±0.032 dB
Coaxial cable (150 ft)	±0.045 dB
Connectors (2 per cable)	±0.1 dB
TOTAL BIAS ERROR	±2.01 dB

CHAPTER IV

RESULTS

The test setups and instrumentation discussed in Chapter 3 are used to produce the results discussed here.

4.1 Vibration

One goal of this study is to examine the potential affect that the vibrations produced by a hybrid-electric power system would have on a multi-rotor sUAS. To accomplish this,

4.1.1 Objectives

As detailed in Chapter 3, the goals for studying vibration as an integration challenge is to characterize the vibrations of a small two-stroke ICE, and use that data to predict how those vibrations will affect the mission capabilities of a multi-rotor aircraft (Figure 5).

4.1.2 Initial Engine Characterization

Of the initial seven RPM phases, only those under 6000 RPM (100 Hz) can be correctly measured by the accelerometer, which has a sampling frequency of 200 Hz. Therefore only the results in the first four phases will be presented and discussed. Table 10 shows the summary data for the engine running on the dampened stand. Within each phase, a time span of one second is selected which displays consistent acceleration behavior and an RPM trend which centers around the goal RPM for that phase with smaller standard deviation between time steps. Within that time span, a representative amplitude (high and low point for a single time step) is measured, and the corresponding force is calculated.

Table 10: Sample observed amplitudes in each axis at each operating point

Phase	RPM	Axis	Accel. Amplitude (m/s^2)	Force Amplitude (N)
1	**3000**	**X**	198.4	281.8
		Y	205.5	291.9
		Z	100.1	142.0
2	**3800**	**X**	206.4	293.1
		Y	178.5	253.5
		Z	195.5	277.6
3	**4600**	**X**	166.4	236.3
		Y	140.7	199.9
		Z	180.2	255.9
4	**5600**	**X**	153.8	218.4
		Y	115.8	164.4
		Z	228.2	324.0

It can be seen that there is significant acceleration, and therefore force, applied in all of the measured directions. The assumption is made that the motion in the X axis can be mostly attributed to the fluctuation in thrust produced by the propeller, further analysis will only be done on the Z and Y axes.

Figure 21 shows the results of frequency analysis conducted on the accelerometer data for the dampened stand in the Z axis. It can be seen that the major peaks in this axis correspond to the RPM in that phase. There is also a trend that as the RPM increases, the peaks that accompany the primary peaks become more significant.

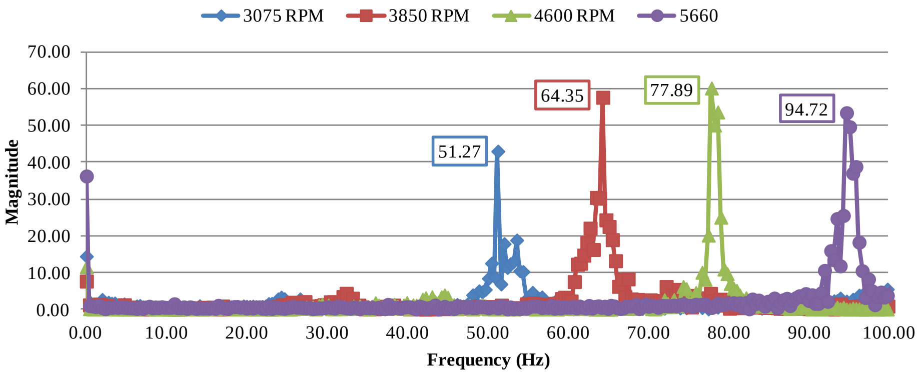

Figure 21: FFT analysis of acceleration in Z axis with varying RPM

Figure 22 shows the results of frequency analysis conducted on the accelerometer data for the dampened stand in the Y axis. It can be seen that the same peaks that correspond to the RPM are present, and the same trend of the peaks surrounding the RPM peaks becoming more significant with higher RPM still exists. However, for the lower RPMs, major peaks appear lower in the frequency spectrum. As the RPM increases, these additional peaks greatly decrease. When comparing Figure 21 and Figure 22, small traces of these unidentified lower-frequency peaks can be seen in the Z axis, but they are significantly less apparent than in the Y axis.

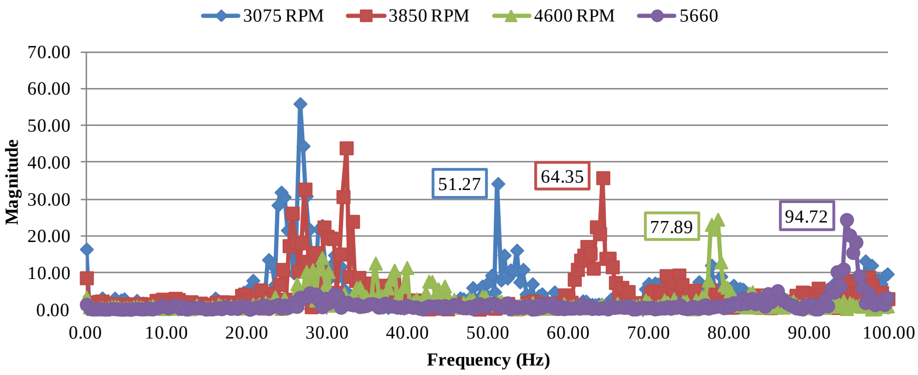

Figure 22: FFT analysis of acceleration in Y axis with varying RPM

Due to the larger vibration amplitudes in the Z axis than in the Y axis for the higher RPM, which represent the more efficient operating range of the engine, the acceleration comparison between the engine and electric motor with the same propeller will only be presented and discussed for the Z axis. For this comparison, the Z axis from the engine measurements will be paired with the X axis from the electric motor measurements, as these axes both correspond to vertical motion.

Figure 23, Figure 24, Figure 25, and Figure 26 show one second of the acceleration data from the engine with the propeller at each RPM, as well as the acceleration data from the electric motor at the closest matching RPM. These small samples were chosen from each data set as range which contained an RPM trend centering around the closest to desired RPM with smaller standard deviation between time steps, as well as consistent acceleration behavior.

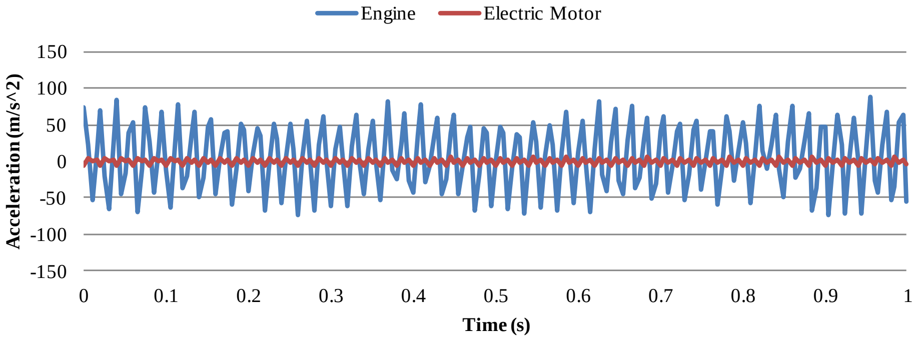

Figure 23: Comparison between acceleration of engine and electric motor with the same propeller, at approximately 3000 RPM in the vertical axis

It can be seen that at approximately 3000 RPM, the vibration signature from the electric motor with the propeller is significantly lower than that of the engine with the propeller. This indicates that most of the vibration of the engine could potentially be contributed to the behavior of the engine alone.

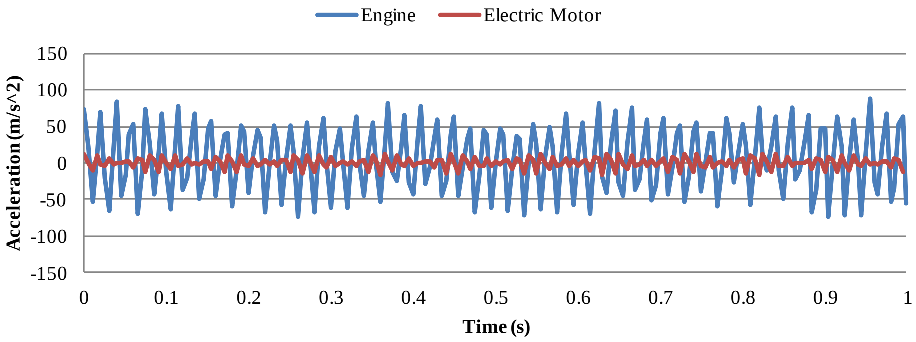

Figure 24: Comparison between acceleration of engine and electric motor with the same propeller, at approximately 3800 RPM in the vertical axis

It can be seen that at approximately 3800 RPM, the vibration signature from the electric motor with the propeller is still significantly lower than that of the engine with the propeller, but now there is visible amplitude modulation in the electric motor data. It still appears that most of the vibration of the engine could potentially be contributed to the behavior of the engine alone.

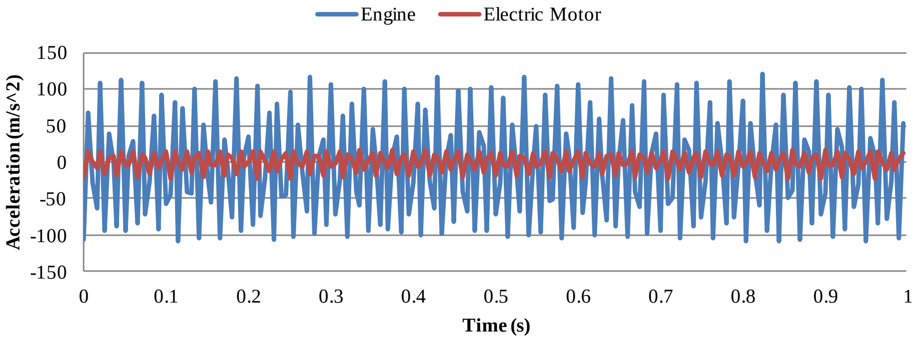

Figure 25: Comparison between acceleration of engine and electric motor with the same propeller, at approximately 4600 RPM in the vertical axis

It can be seen that at approximately 4600 RPM, the vibration signature from the electric motor with the propeller remains significantly lower than that of the engine with the propeller. This indicates that most of the vibration of the engine could potentially be contributed to the behavior of the engine alone.

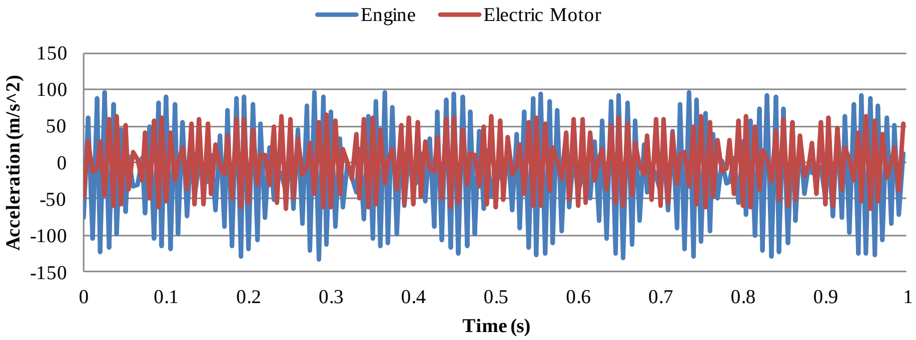

Figure 26: Comparison between acceleration of engine and electric motor with the same propeller, at approximately 5600 RPM in the vertical axis

It can be seen that at approximately 5600 RPM, the vibration signature from the electric motor with the propeller is significantly larger than at the lower RPM, and displays obvious amplitude modulation. The vibration signature from the engine with the propeller also displays obvious amplitude modulation at this higher RPM, but at a little more than half of the frequency of the electric motor with the propeller. During testing, it was visually observed that directly below and around 5600 RPM, the electric motor with the propeller was visibly vibrating much more strongly that at the lower RPM. It is not apparent what this distinct amplitude modulation affect and stronger electric motor vibration at this higher RPM can be attributed to, but it is thought to be caused by the physical characteristics of the test stand.

4.1.3 Initial Vibration Replication

The initial calculations of how much mass is required at a certain offset from center is shown in Table 11.

Table 11: Initial Cam Calculations

Rotational Velocity	5700	RPM
+Z Acceleration	105	m/s^2
Engine Mass	1.33	kg
Offset Distance	0.0254	m
Offset Mass	0.01547	kg

The design point for the cam is chosen as 0.55oz (0.01547kg) placed 1 inch (0.0254m) from the center. However, to decrease risk in case of some kind of failure due to the induced vibration on the electric motor, much smaller masses were used in initial testing at 1 inch from the center, and the mass was steadily increased in multiple tests until the design point was safely reached.

It is observed during testing that with 0.1oz and 1.35in from the center of the shaft rotating at 5700 RPM, the engine vibration magnitude is being very closely replicated, so the data from this test is fully processed. Figure 9 shows the comparison between the engine vibration signature at 5700 RPM and the electric motor vibration signature at 5700 RPM with a weight of 0.1oz at 1.35in from the center of the shaft.

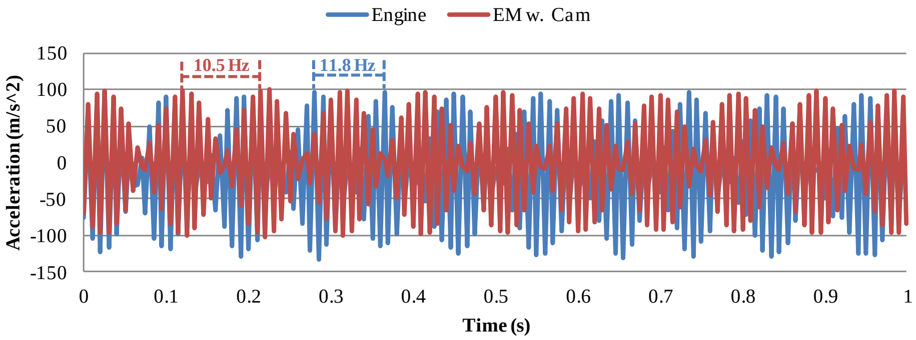

Figure 27: Acceleration magnitude of electric motor with cam (0.1oz @ 1.35in) and engine at 5700 RPM

A much smaller weight was required for replication than expected, so a comparison is done between the engine and the electric motor with no cam at 5700 RPM to identify any inherent system imbalances that might be contributing to the overall measured signature. It is found that the electric motor does produce vibration even without a load on it, which explains why less off-center mass was required to replicate the engine vibration than originally calculated. When vibration is intentionally being produced, the inherent imbalance of the electric motor is amplified.

4.1.4 Sensor Validation

In order to measure engine vibration above 6000 RPM (100Hz), the VMU931 is tested as a potential replacement for the VN100 in the vibration measurement tests. With both mounted on the engine, as shown in Figure 11, the engine is accelerated to 4600 RPM and data is taken. A representative second of data is taken from both sensors, and the results are shown in Figure 28. There appears to be significant variation both in the magnitude and behavior observed by the two sensors. The amplitude modulation observed in this measurement as well as previous with the VN100 is not present in the VMU931 data. The VN100 also measures lower maximum amplitudes, on the order of 4g (~40 m/s) less than the VMU931.

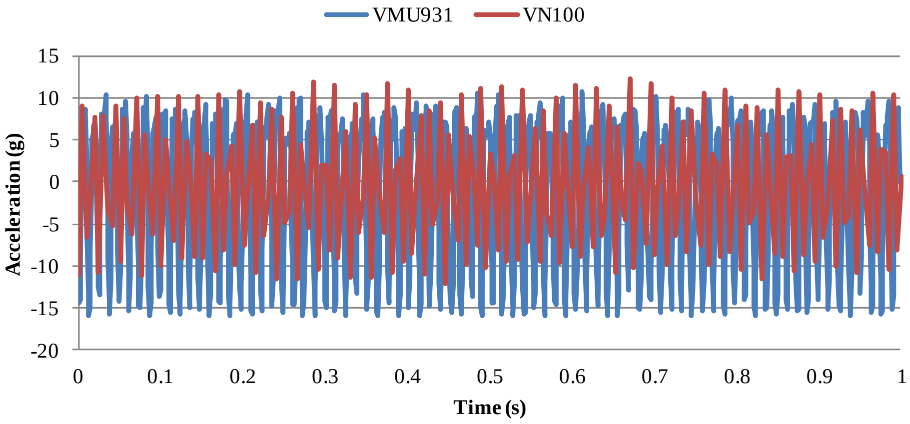

Figure 28: Comparison of Engine vibration signature as recorded by VN100 and VMU931 at 4600 RPM (~77 Hz)

To determine which sensor is correctly representing the vibration signature of the engine, tests were conducted with the vibration table (Appendix, Figure 97) to provide a known vibration source, and an the MSR165 Data Logger as an additional sensor for comparison.

A comparison of the magnitudes recorded by all of the sensors under the same stimulus from the vibration table (Figure 29) shows a vast discrepancy between the VN100 and the other two sensors.

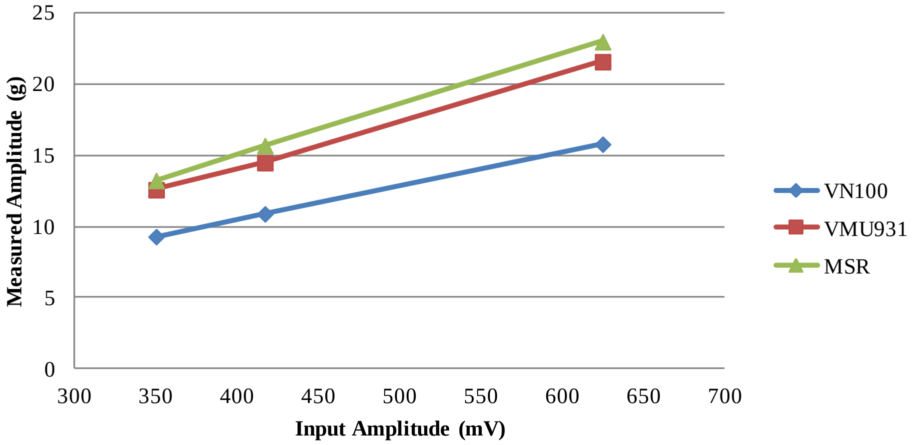

Figure 29: Discrepancy between measured vibration amplitude from three different accelerometers with the same known stimulus. Vibration amplitudes shown are the maximum observed amplitude measurement.

The stimulus of the vibration table is set to a sine wave at a specific frequency and magnitude/ Comparison between the behavior of the VN100 and the VMU931 shows that the VN100 is once again recording data with distinct amplitude modulations which should not be present given the constant-amplitude sine wave input (Figure 30).

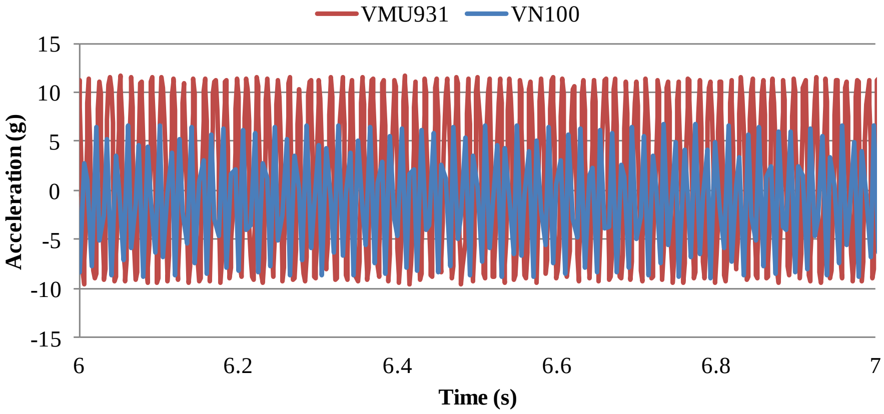

Figure 30: Vibration signature as measured by the VN100 and VMU931 with a 75 Hz sine wave stimulus

Based on these diagnostic tests, it is determined that the VN100 is not accurately representing the vibration signature of the sample engine. Based on this conclusion, and the sampling frequency limitations of the sensor, previous attempts and vibration replication will be repeated in order to simulate the behavior at the test point of interest (6000 RPM) as well as correct for the under-estimated vibration amplitude.

4.1.5 Final Engine Characterization

The engine is re-characterized using the VMU931.

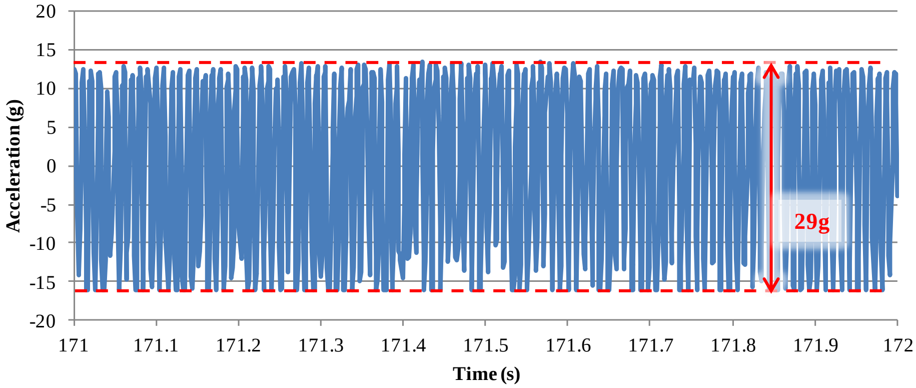

Figure 31: One-second representative measurement of engine vibration at approximately 6000 RPM. Full amplitude is observed to be approximately 29g, which makes the effective single-direction amplitude 14.5g (~142 m/s^2)

4.1.6 Final Vibration Replication

The previous cam design calculations are repeated, but with the new measurements of the engine vibration signature taken using the VMU931 accelerometer (Table 12).

Table 12: New Cam Calculations

Rotational Velocity	6000	RPM
Single-direction Acceleration	142	m/s^2
Engine Mass	1.33	kg
Offset Radius	1.5	in
Offset Mass	0.36	oz

The previous cam design testing is also repeated, with the new cam design. The acceleration sensor (VMU931) is measuring full saturation at 6000 RPM with the current cam design with the chosen test stand configuration. This cam design is also tested while mounted to the M600 in a lab setting (propellers inactive) (Appendix, Figure 96). It is found to fully saturate the sensor in this configuration as well. The measured vibrations of the engine do not fully saturate the sensor, and based on calculations the current cam design shouldn't either. Therefore, it is determined that a reduction will have to be made to the off-center weight in the current cam design to account for inherent imbalance in the electric motor, which is thought to cause the higher vibration amplitudes being observed (also observed in previous cam designs and testing).

To achieve a similar vibration magnitude to that measured from the engine, the offset mass is systematically reduced, and the resulting vibration measured, until this goal is reached. These iterative steps are shown in Table 13, along with the calculated vibration that the mass and offset should produce as well as the actual measured vibration. Any measurements above the saturation limit of the VMU931 (16g) are simply expressed as being in excess of this limit, which converts to ~157m/s^2.

Table 13: Cam Mass Reduction Test Points (6000 RPM)

Offset Mass (oz)	Offset Radius (in)	Calculated Accel. (m/s^2)	Measured Accel. (m/s^2)
0.36	1.5	142	>157
0.288	1.5	114	>157
0.246	1.5	97	>157
0.162	1.5	64	147.2

When the mass had been reduced to 0.162 oz, the measured acceleration was relatively close, but slightly higher than the signature of the engine. It would be preferable to overshoot the engine vibration rather than undershoot since the goal of this work is to observe a worst-case scenario. A direct comparison between the vibration of the engine and the electric motor with the cam is shown in Figure 32.

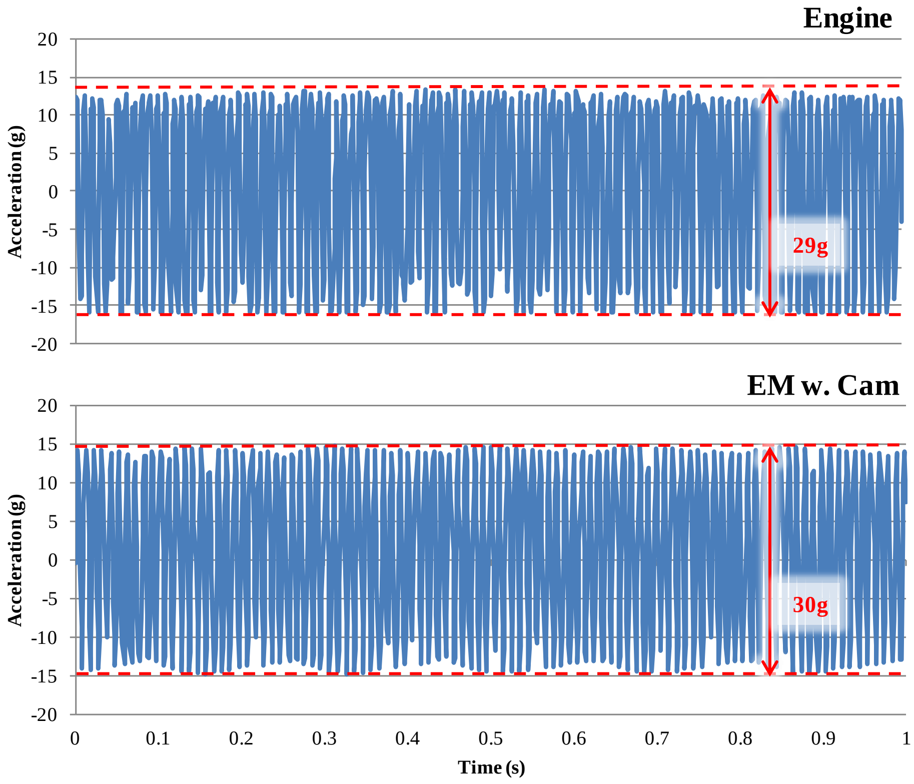

Figure 32: One-second representative vibration measurement of engine and electric motor with cam (0.162oz, 1.5in off-center) at approximately 6000 RPM

In preparation for flight testing on the M600, the electric motor with the cam and all necessary power and control electronics are integrated with the platform. The electric motor is then run at 6000 RPM, and the vibration signature measured while the aircraft rests stationary on the lab floor. The results of this testing are show in Figure 33.

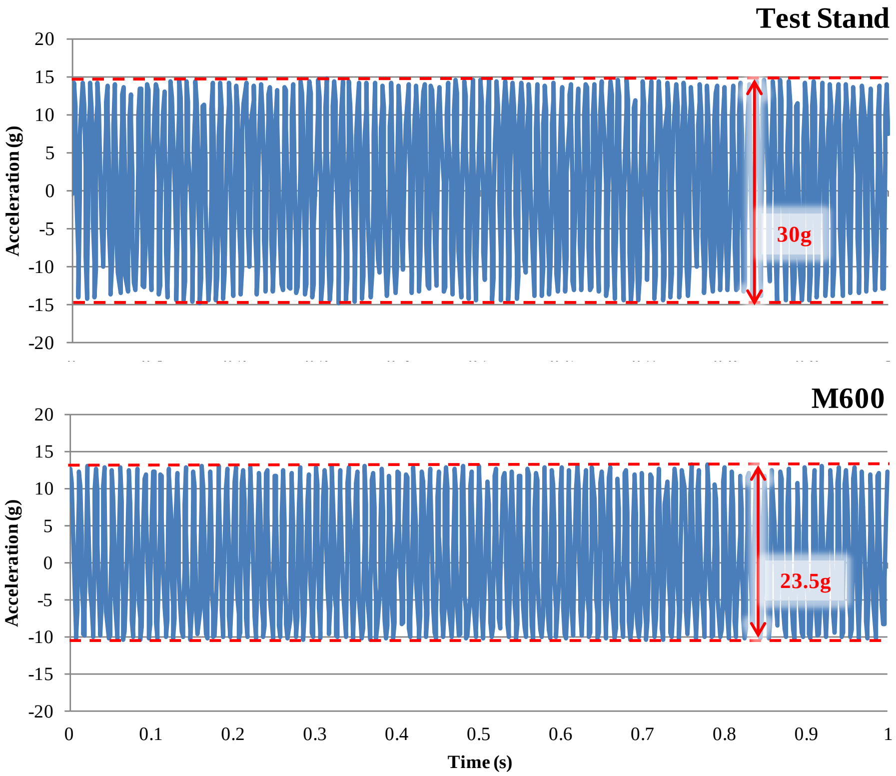
Test Stand

M600

Figure 33: One-second representative vibration measurement of the electric motor with cam (0.162oz, 1.5in off-center) on the test stand and on the M600 at approximately 6000 RPM

Once again, it is observed that the structure to which the vibration source is mounted to has a significant effect on the vibration measured.

4.1.7 Flight Testing (December 2017)

From the flight logs of the M600, multiple platform behaviors are examined for the initial vibrations at 5700 RPM. Figure 34 shows the actual path traveled by the platform while following the same waypoints from DJI Go, with and without the attached electric motor active. It can be seen that the flight with the electric motor active demonstrated a couple of distinct variances not seen in the flight with the motor inactive.

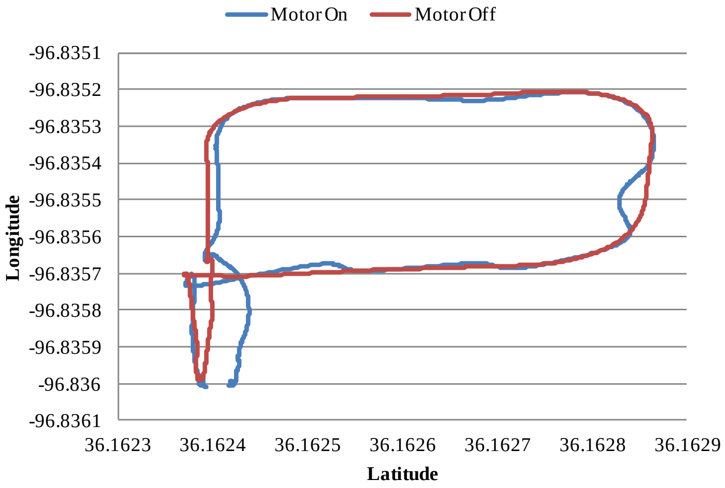

Figure 34: Comparison of platform location following the same flight path with electric motor on and off

Figure 35 and Figure 36 shows the altitude during the flights with and without the motor active. The start time and flight time vary between the motor on and motor off tests, so in each figure plotted by data points, dotted lines indicate the data taken at altitude. It can be seen that there are some minor fluctuations in altitude during the motor on test that are not present in the motor off test.

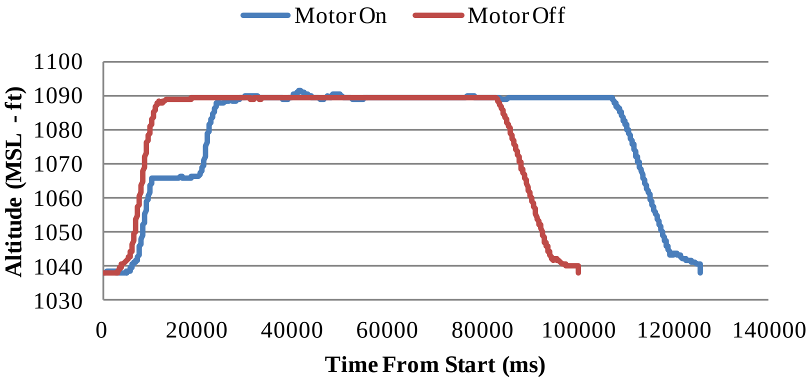

Figure 35: Comparison of altitude during flights with electric motor on and off (entire duration)

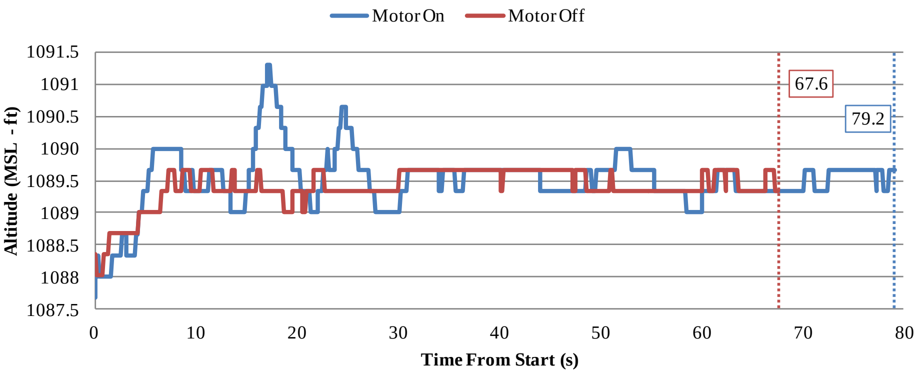

Figure 36: Comparison of altitude, starting when flight altitude is reached. Duration in seconds for both flights shown in boxes on right

Figure 37 shows the velocity data from the aircraft during the two flights. It can be seen that the velocity of the platform fluctuates significantly more during the flight with the electric motor active than without. This observation explains the differing flight times from the motor off to the motor on test for the same flight path.

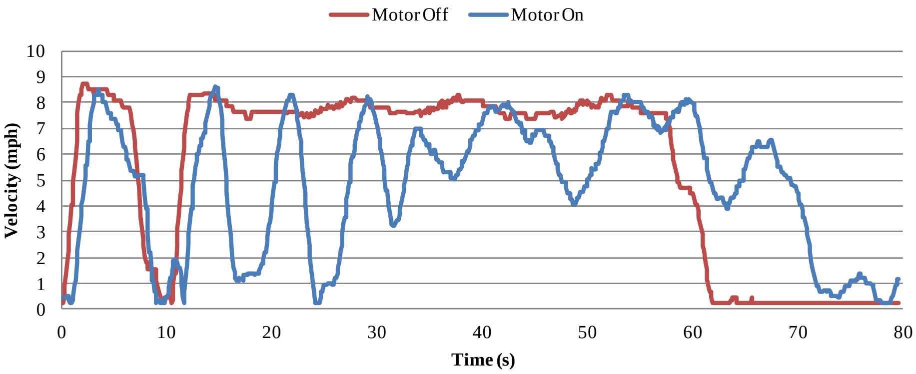

Figure 37: Comparison of velocity with the same flight path with the electric motor on and off (from time that altitude is reached)

Figure 38 shows the number of connected satellites during flight with the motor on and off. It can be seen that during the flight with the motor off, 16 satellites were consistently connected for the majority of the time at altitude, while with the motor on the number of satellites fluctuates between 15 and 16 throughout the flight (in the same location at the same altitude).

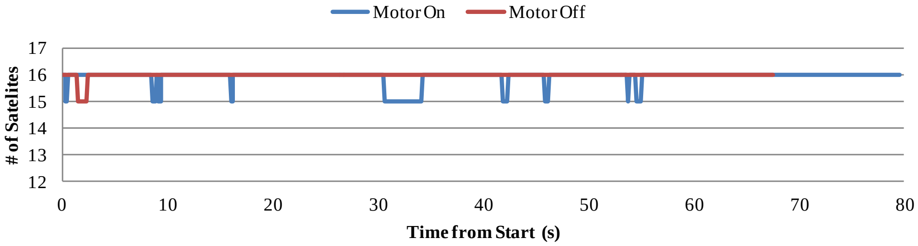

Figure 38: Comparison of number of satellites connected during the same flight path with the electric motor on and off (from time that altitude is reached

4.1.8 Flight Testing (March 2018)

From the flight logs of the M600, the waypoints and actual flight paths flown for testing the increased vibration at 6000 RPM have been plotted in Figure 39.

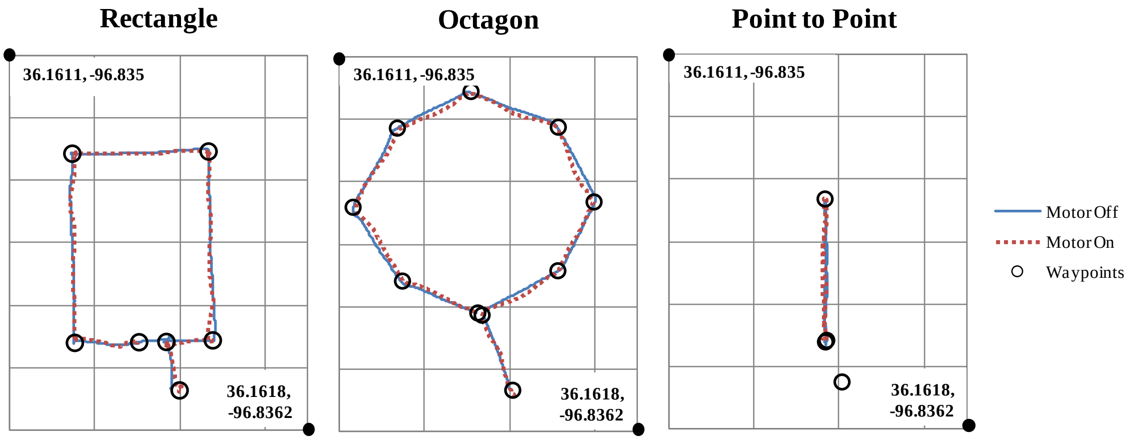

Figure 39: Three different waypoint-driven flight paths with the actual path flown during each flight

Starting with the rectangular flight path, other performance parameters such as flight velocity, signal strength, roll, pitch, and yaw are compared between motor on and motor off flights.

Composite velocity (independent of direction) is plotted relative to an approximately normalized start time (Figure 40). One key observation from the velocity data, as well as the other rectangle flight path data, is that with the motor on, the flight path took approximately 40 seconds (33%) longer than the with the motor off. The reason for this can be seen in the velocity plots: there are several points at which the aircraft lingers in a hover with the motor on where it did not with the motor off.

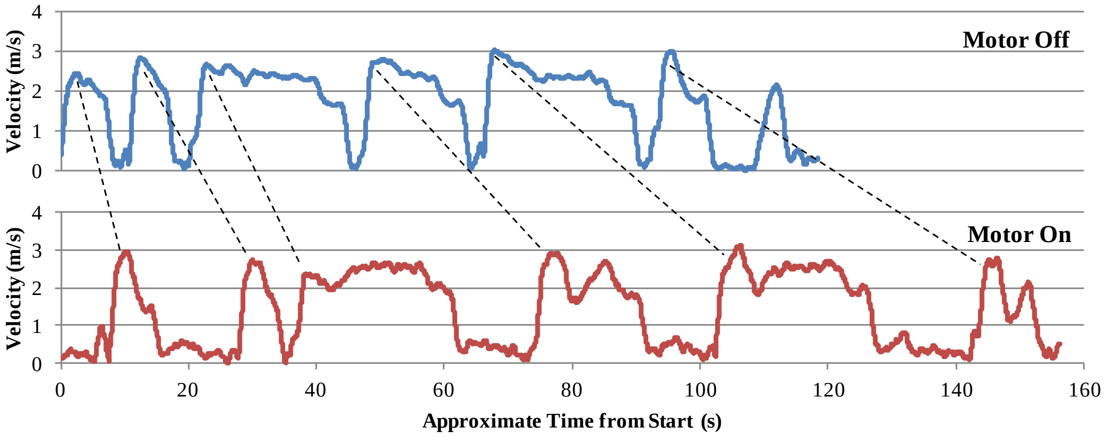

Figure 40: Composite velocity of the aircraft during flight for the rectangular flight path, with the motor off and the motor on. Dotted lines indicate the corresponding behaviors between the two flights, which relate to location in the flight path.

Signal strength has also been plotted relative to an approximately normalized start time (Figure 41). It can be seen that with the motor running and producing vibration, the signal strength drops significantly more throughout the flight than with the motor off.

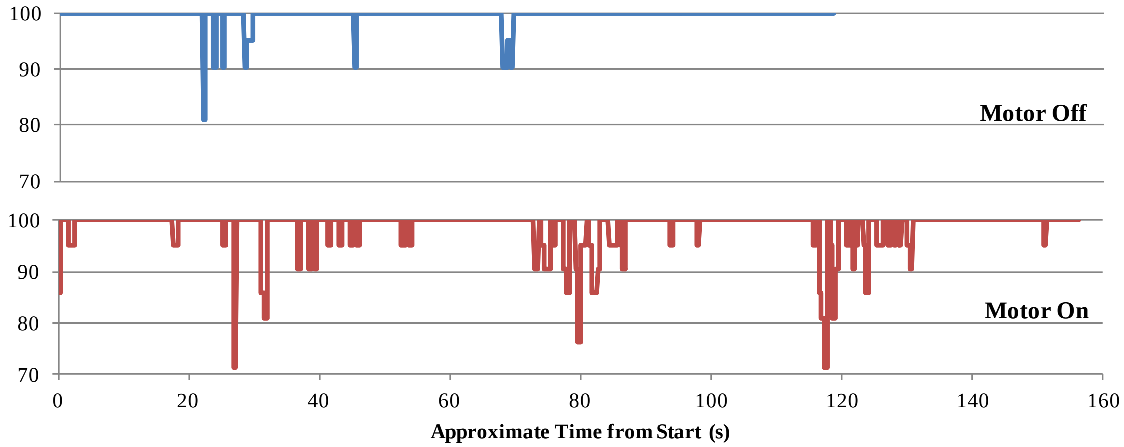

Figure 41: Signal strength during flight for the rectangular flight path, with the motor off and the motor on.

Figure 42 shows the roll measurements reported by the on-board IMU during flight testing both with and without the motor active and producing vibration.

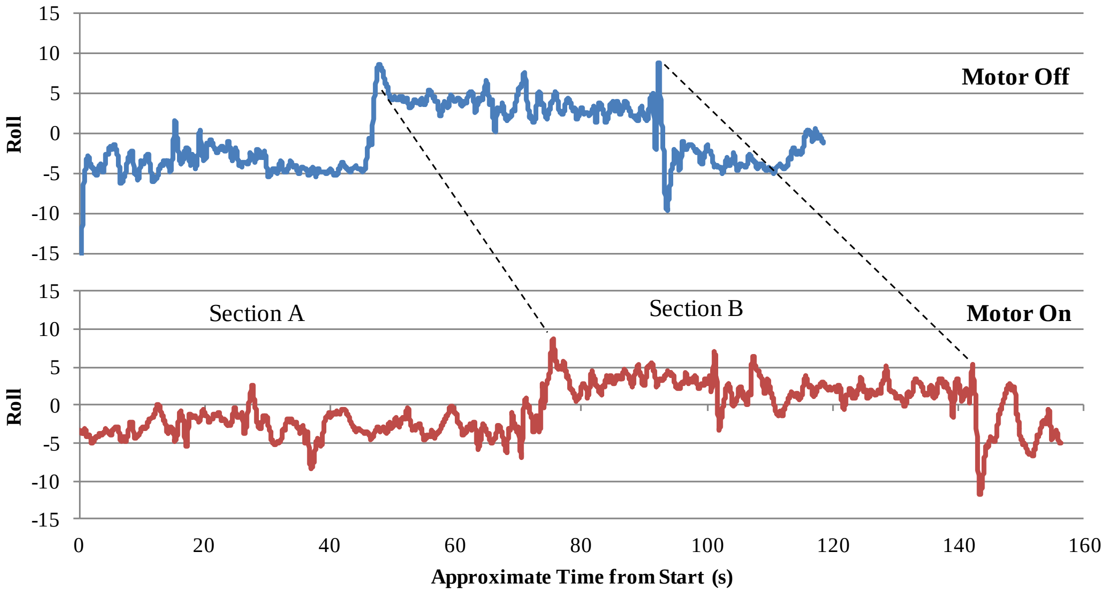

Figure 42: IMU roll measurement during flight for rectangular flight path, with the motor off and the motor on. Dotted lines indicate the corresponding behaviors between the two flights, which relate to location in the flight path.

Standard deviation is calculated for the labeled regions of roll behavior to better quantify the differences between the motor off and motor on flights (Figure 43).

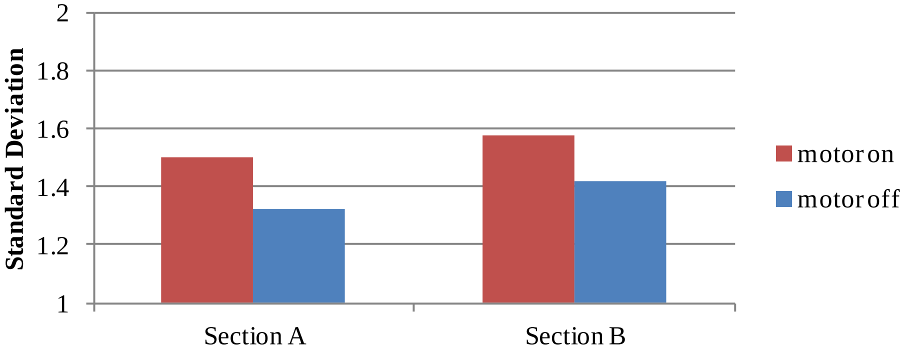

Figure 43: Standard deviation for two of the regions between the dotted lines in Figure 42 both with the motor on and motor off.

Figure 44 shows the pitch measurements reported by the on-board IMU during flight testing both with and without the motor active and producing vibration.

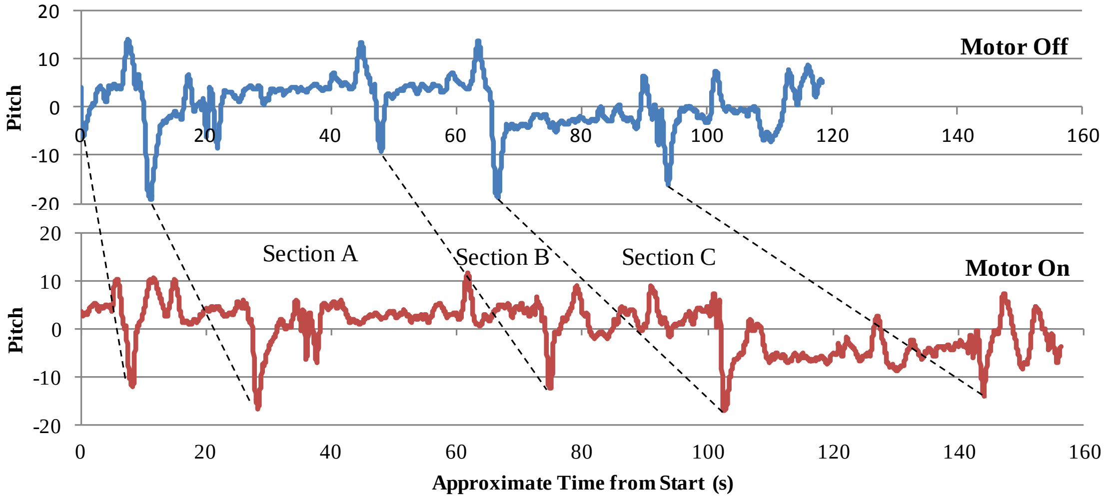

Figure 44: IMU pitch measurement during flight for rectangular flight path, with the motor off and the motor on. Dotted lines indicate the corresponding behaviors between the two flights, which relate to location in the flight path.

Standard deviation is calculated for the labeled regions of pitch behavior to better quantify the differences between the motor off and motor on flights (Figure 45).

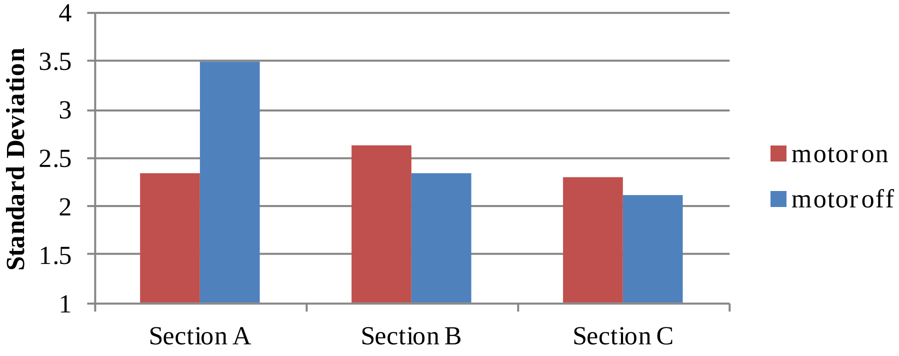

Figure 45: Standard deviation for three of the regions between the dotted lines in Figure 44 both with the motor on and motor off.

Although the overall trend from the pitch and roll data appears to show that with the motor on, there is more variation in the platform orientation during flight than with the motor off (no additional vibration). However, Section A of the pitch data appears to break this trend. This is attributed to the fact that in Section A of the motor off data, there appears to be a steady increase in pitch over time that is not seen in the motor on data. This could be due to a difference in the wind conditions during that flight as compared to the motor on flight.

Data from the two additional flight paths (octagon & point to point) showed similar trends to those discussed her for the rectangular flight path. The processed results can be found in the Appendix. An additional note from this flight testing is that at one point in between flight tests, the aircraft was on the ground, and the electric motor was active and producing vibration. At this time, the controller was attempting to connect to the aircraft, and a warning was produced stating that the IMU was unable to boot up. Through systematic reduction of the electric motor RPM (and therefore the vibration magnitude) the IMU was eventually able to boot up successfully, around 4100 RPM.

4.1.9 Precision Uncertainty

Precision uncertainty for the vibration measurement tests is evaluated in a variety of ways. First, the variation of the engine RPM at a set throttle position is quantified (Figure 46). Over three different tests, it can be seen that the overall standard deviation in engine speed at a set throttle position is typically 8RPM.

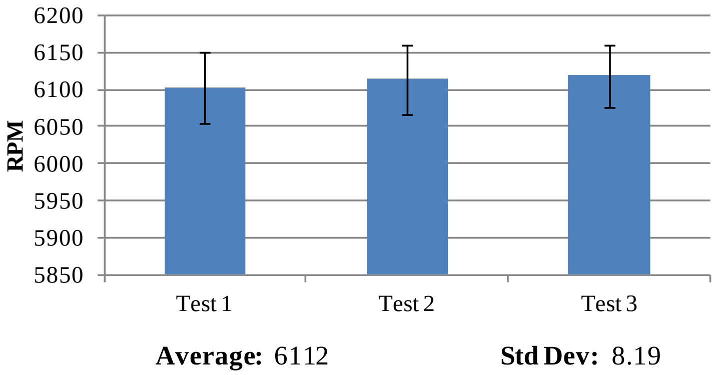

Figure 46: Precision uncertainty of engine RPM during repeated tests at with a goal RPM of 6000. Error bars show standard deviation of RPM for each specific test.

The variations in measured acceleration from the engine at approximately the same RPM set point is quantified. It is found that based on the measurements from the VMU931, the standard deviation of the maximum amplitude (which is used for the vibration replication stages) measured at approximately 6000 RPM is 0.47g (Figure 47).

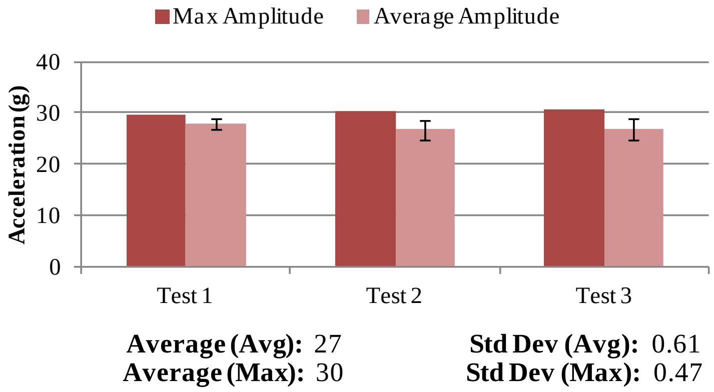

Figure 47: Precision uncertainty of engine acceleration measured from the VMU931 at a goal RPM of 6000, for both the maximum measured acceleration and the average measured acceleration. Error bars show standard deviation of acceleration amplitude for each specific test.

For the electric motor vibration replication tests, multiple measurements of the same testing conditions were not available, so different measures were taken to analyze the variation in vibration behavior. First, a comparison is made between the standard deviation of the RPM of the electric motor during three tests with different acceleration magnitudes (Figure 48). The results show that in each case, the standard deviation in RPM is similar, and does not appear to correlate to the magnitude of the vibration being produced. On a whole, the standard deviation between all three tests is ~19RPM.

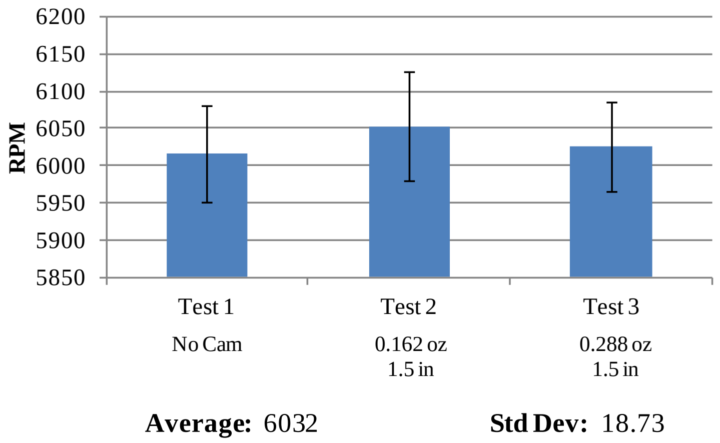

Figure 48: Comparison of three independent electric motor tests with a goal RPM of 6000. Average RPM displayed for each test with error bars of the standard deviation during that test. The cam weight and offset distance is noted (if applicable), and the overall average and standard deviation of the three tests is displayed.

Finally, the standard deviations of the acceleration amplitude measured both with and without a cam attached and producing vibration are calculated (Table 14). It appears that the standard deviation may be related to the magnitude of the vibration being produced, implying that the system becomes more unstable when more vibration is being actively produced.

Table 14: Comparison of acceleration consistency of the electric motor at a goal RPM of 6000 with and without forced vibrations

	Cam Details	Average Amplitude	Standard Deviation
Test 1	None	0.98	0.15
Test 2	0.162 oz 1.5 in	27.4	1.42

4.2 Cooling

4.2.1 Objectives

As detailed in Chapter 3, the goals for studying cooling as an integration challenge is to characterize the cooling requirements of a small two-stroke ICE, and use that data to anticipate the affect that meeting the cooling requirements will have on the efficacy of a hybrid power system as an endurance booster.

4.2.2 Steady-State Temperature Testing

The RPM and temperature data from the steady state temperature test is plotted versus time in Figure 49. The three phases (4700, 5550, and 6250 RPM) can be clearly seen between ignition and engine shutoff. The average temperatures observed at each phase do not exceed 300°F.

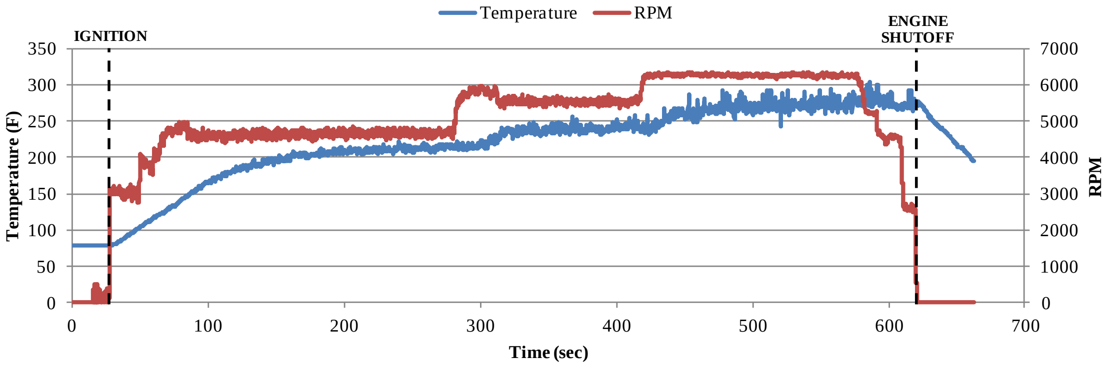

Figure 49: Temperature and RPM during steady-state temperature test

The airflow estimates produced are shown in Table 15 along with the corresponding RPM values, power required to produce that airflow, and the steady state temperature reached by the cylinder head with an ambient temperature of 79°F.

Table 15: Steady-state temperature under given operating conditions

RPM	Power Req (HP)	Induced Velocity (m/s)	Est. Useful Velocity (m/s)	Mass Flow (kg/s)	Avg Temp (°F)
4700	1.58	10.2	3.4	3.34	210
5550	2.60	12.0	4.0	3.94	240
6250	3.71	13.5	4.5	4.44	273

While the propeller produces a significant amount of airflow, only a portion of it actually travels over the cooling fins of the cylinder head, which are located in the top portion of the propeller area and adjoining the center. The useful velocity has been estimated as one third of the total induced velocity. Based on these calculations, it can be seen that even with increasing forced convection (with increasing RPM), the temperature of the cylinder head continues to increase. It can be concluded that without forced convection, or some other external cooling such as a water-cooled system, the cylinder head temperature would increase to a point of detriment to the engine.

4.2.3 Predictive Calculations

Predictive cooling calculations are conducted for the engine of interest in this study (the DA50) using basic convection cooling concepts. Equation 10 shows the relationship between volumetric flow required ($\dot{V}$) and the heat produced by the engine (Q). Heat produced by the engine is estimated based on the power output of the engine and an estimated thermal efficiency (η). C_p is the specific heat of air, ρ is the density of air, and ΔT is the allowable rise in temperature.

$$\dot{V} = \frac{Q}{C_p \rho \Delta T} \tag{10}$$

Based on the measured thermal efficiency of a larger two-stroke gasoline engine [29], a thermal efficiency of 0.3 is chosen for these calculations. This is assumed to be an over-estimation of the realistic thermal efficiency of the engine used in this study due to the smaller size of the engine. Required volumetric flow and required flow velocity based on an estimate of the frontal area of the cylinder head, are calculated and the results displayed in Table 16. The center column can be compared to the steady-state temperature test conducted previously. The discrepancy in estimated velocities can be due to an overestimated engine efficiency, or inaccuracy in the estimate of useful velocity from the propeller.

Table 16: Required Cooling Estimates for DA50

Assumed η	0.3	0.3	0.3	
Rated Power	5	3.7	2.68	HP
	3,729	2767	2000	W
Waste Power (heat)	8,700	6,455	4,667	W
Max Allowable Temp	300	273	300	°F
ΔT	227	200	227	°F
Estimated Cylinder Head Area	0.058	0.058	0.058	ft^2
Required Flow Volume	118.7	99.9	63.7	CFM
Required Flow Velocity	10.5	8.9	5.6	m/s

A chart presenting cooling requirements for a given power output, using the same calculations discussed above, has been produced (Figure 50).

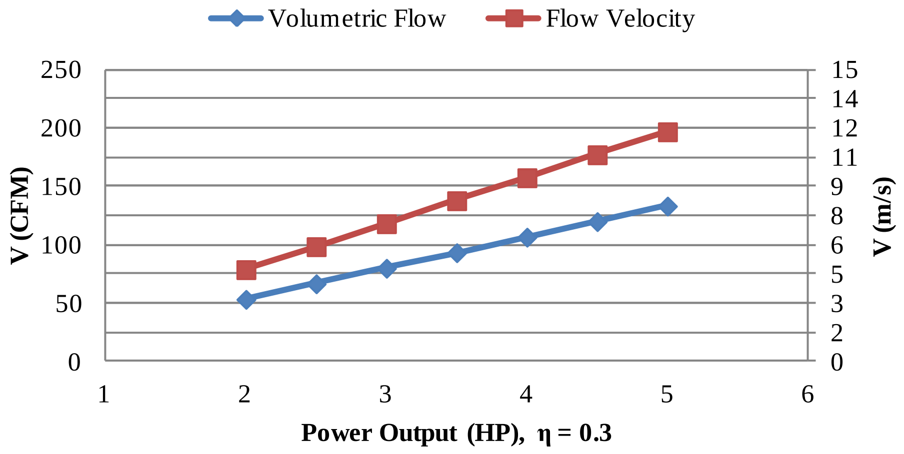

Figure 50: Required cooling estimates for a small two-stroke engine based on power output and an assumed thermal efficiency of 0.3.

This chart can be used to estimate the amount of cooling required for different hybrid power systems.

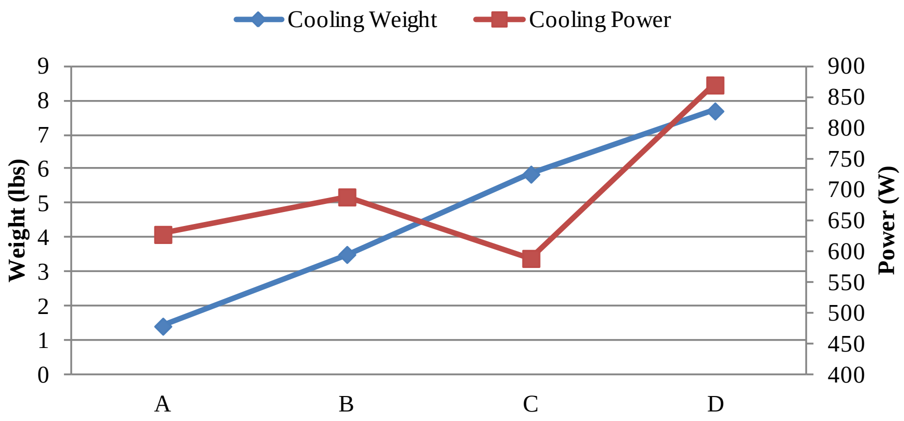

Figure 51: Estimates of the design margin for cooling hardware weight and electrical power for the four theoretical hybrid configurations discussed in Chapter 2 (Table 3).

Figure 51 shows the amount of additional weight (for cooling hardware, or other) that could be added to the hybrid configuration discussed in Chapter 2 before the hybrid would match the flight time of the battery-only configuration. It also shows the amount of power that could be siphoned for electrically-powered cooling systems from the excess being produced by the engine during flight. The cooling power margin was determined by subtracting the amount of power required by the platform in hover from the steady power supply capability of the hybrid system. Cases B and C have the same engine but carry different amounts of fuel (different takeoff weights), which is why case C has a smaller cooling power margin. From a design perspective, these margins give an idea of how feasible a endurance-boosting hybrid system is.

4.3 Noise

4.3.1 Objectives

As detailed in Chapter 3, the goals for studying noise as an integration challenge is to characterize the acoustic signature of a small two-stroke ICE, as well as that of a compatible COTS multi-rotor aircraft, and use that data to predict how the noise signature of the aircraft will change with the addition of the hybrid power system (Figure 6).

4.3.2 Indoor Engine Characterization

Initial testing is conducted in the lab with the experimental setup illustrated in Figure 7. Figure 52 and Figure 53 show comparisons between five different acoustic spectra: ambient background noise, noise produced by an electric motor with and without a propeller, and noise produced by an ICE with a propeller. The RPM of each test in the following data sets were all approximately 6250. Figure **52** shows the data collected by Microphone A and Figure 53 shows the data collected by Microphone B, the locations of which are shown in Figure 18 and in the bottom-left corner of each figure. Both data sets were measured with a resolution of 10 Hz, therefore tones that fall between increments of 10Hz were not measured.

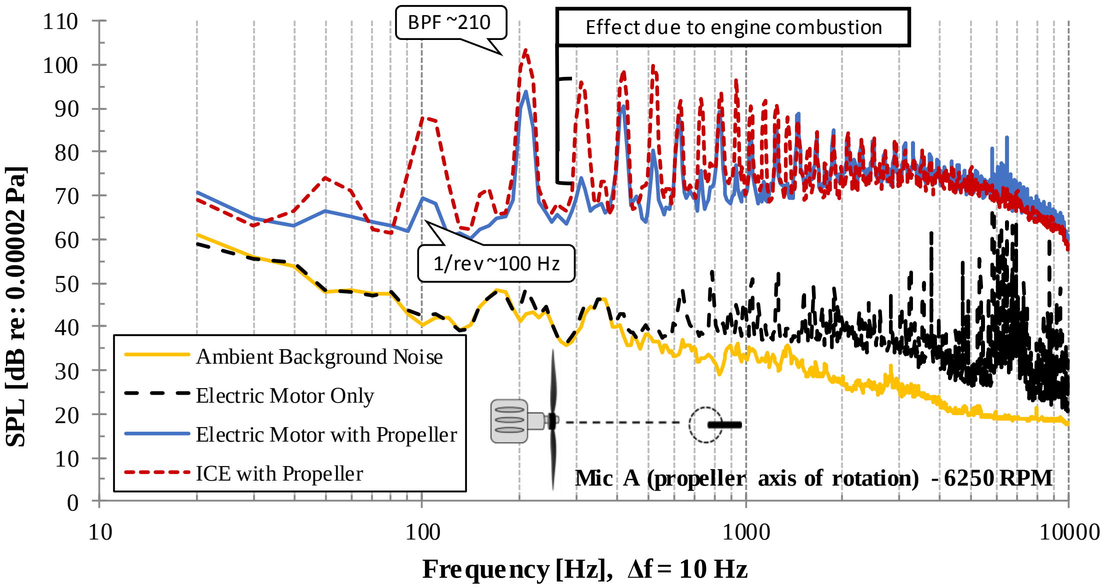

Figure 52: Comparison of narrowband acoustic spectra (ambient background noise with and without exhaust, electric motor with and without a propeller, and ICE with a propeller), all at 6250 RPM, with Microphone A at a distance of 115 inches

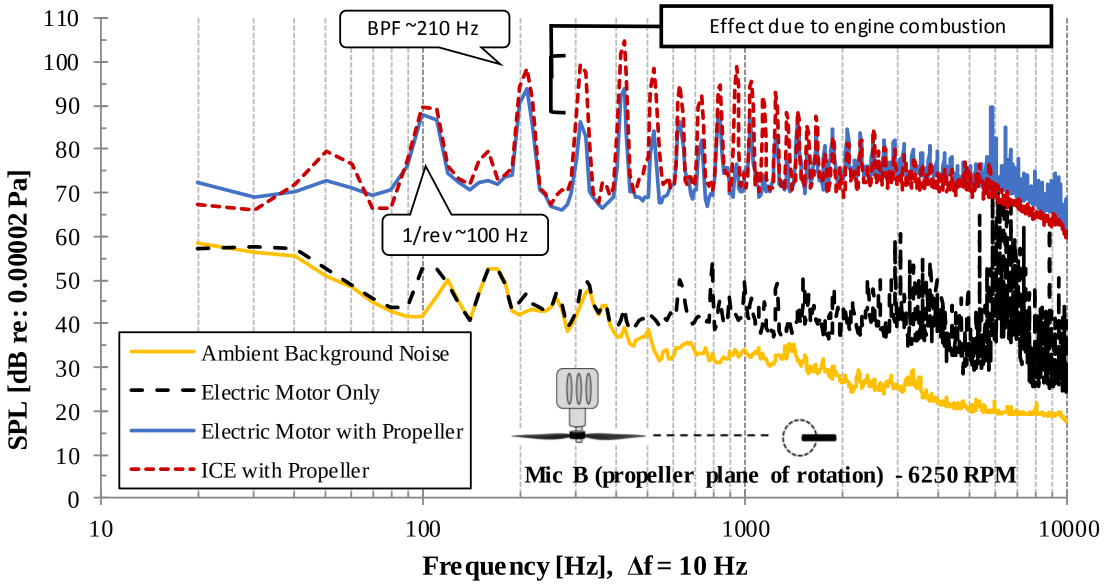

Figure 53: Comparison of narrowband acoustic spectra (ambient background noise with and without exhaust, electric motor with and without a propeller, and ICE with a propeller), all at 6250 RPM, with Microphone B at a distance of 42.5 inches

The ambient measurements were taken with the lab exhaust removal system activated. The ambient spectrum shows a tone at 120 Hz and a considerable amount of broadband noise. The cause of the tonal content is not known but is believed to be due to the heating, ventilation and air conditioning (HVAC) in the testing room, while the broadband is caused by the turbulent air from the exhaust removal system.

Two sets of data were collected which included propeller noise (shown in Figure 52 and Figure 53): the electric motor with the propeller, and the ICE with the propeller. In all non-ambient spectra a 1/rev appears at approximately 100 Hz. For both electric motor cases, this tonal noise is believed to be caused by an instability in the electric motor. For the data from the ICE with propeller, this is caused by the combustion within the engine. The engine used for this test is a two-stroke engine that completes a power cycle at every revolution of the crankshaft. Therefore, the combustion noise produces a fundamental tone at the frequency associated with the RPM that is the same as the 1/rev. This type of noise also produces harmonics that occur at every multiple of the fundamental tone. These harmonics, as well as the rotor stator interaction noise, will in turn increase the tonal content at the BPF and its harmonics. Due to the presence of combustion noise, there is a clear increase in tonal noise at the 1/rev and its associated harmonics between the data for the ICE with propeller and the data for the electric motor with propeller.

The noise produced by a propeller is well known and contains both, tonal content and broadband content[30]. The tonal content consists of the blade passing frequency (BPF), which can be calculated as the number of propeller blades multiplied by the RPM and divided by 60 seconds per minute. This tone appears at approximately 210 Hz, and its associated harmonics which appear at multiples of the BPF. The tonal content tends to dominate the lower frequencies while the broadband content dominates the high frequencies. It is also apparent that another tonal noise source is present which is in the form of a rotor wake-body interaction between the exhaust duct and the propeller. This type of noise has been shown to exist in typical multi-rotor aircraft configurations[31], although the cause is typically the arm of aircraft that holds the electric motor and acts as the interacting body. These tones would appear at the BPF and every harmonic and has even been shown to appear at half harmonics. This rotor wake-body interaction noise is also present in the ICE case since the exhaust duct is in the same position, however the ICE case also has the presence of combustion noise at the same frequencies.

Acoustic measurements were also performed without a propeller attached to the electric motor. The purpose of this test was to determine the noise produced by the electric motor and if this noise contributes to the overall noise produced by the motor-propeller system. At the lower frequencies (20-400 Hz) the ambient background noise with the lab exhaust removal system activated dominates, however at the higher frequencies (600-10,000 Hz) the spectrum becomes dominated with tonal content. At these higher frequencies the motor noise appears to be contributing to the overall system noise. Between 6,000 and 10,000 Hz, there is a clear increase in tonal content in the Electric Motor with Propeller spectrum that is not present in the ICE with Propeller spectrum.

Table 17: Overall Sound Pressure Level of each acoustic measurement, calculated between 20 – 10,000 Hz

Acoustic Measurement	**Mic A OASPL (20-10000 Hz)**	**Mic B OASPL (20-10000 Hz)**
Ambient with Exhaust Off	50.0	52.4
Ambient with Exhaust On	65.2	65.3
Electric Motor Only	76.2	86.5
Electric Motor with Propeller	105.3	106.4
ICE with Propeller	110.9	111.8

Table 17 shows the overall sound pressure level (OASPL) for each acoustic measurement taken, calculated between the frequencies 20-10,000 Hz. As expected, there is a clear increase in OASPL as noise sources are added to the environment. The greatest difference occurs when the propeller is added to the electric motor, which resulted in an increase in OASPL of approximately 20-30 dB depending on the microphone placement. However, the overall system noise increases again when the propeller is driven by an ICE, with an increase in OASPL of 5 dB. This increase can be considered significant due to the fact that the typical human can detect an increase of at least 3 dB. Assuming that the noise sources are in phase, the increase of 5dB over the entire frequency spectrum indicates that the noise source has been effectively doubled. It should also be noted that these results may vary depending on the orientation of the intake and exhaust ports of the engine relative to the microphones.

4.3.3 Outdoor Engine Characterization

To truly capture the far-field acoustic behavior of the engine, the previous tests were repeated in an open field at night (least background noise possible). The results from these measurements are shown in Figure 54. The ambient sound, unloaded electric motor, and both the electric motor and engine with the propeller operating at 6000 RPM are all plotted from 10 to 10,000Hz. The measurements from microphone B (Figure 19) are chosen as representative.

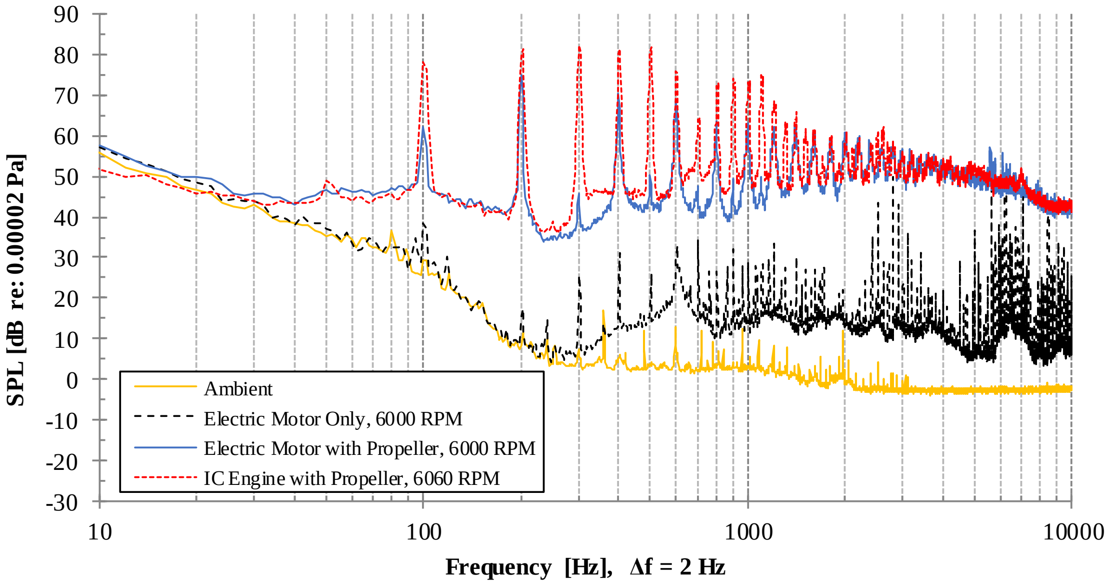

Figure 54: Narrowband acoustic data of DA50 engine and electric motor with 22x8 propeller measured at a radius of 20 ft, microphone 1 (see Figure 19)

4.3.4 Multi-Rotor Platform Characterization

The M600 acoustic signature is measured while hovering 30ft above a 20ft radius microphone array. Figure 55 shows the ambient noise, the stock aircraft signature (no extra weight), as well as the aircraft signature under load, all plotted from 10 to 10,000 Hz.

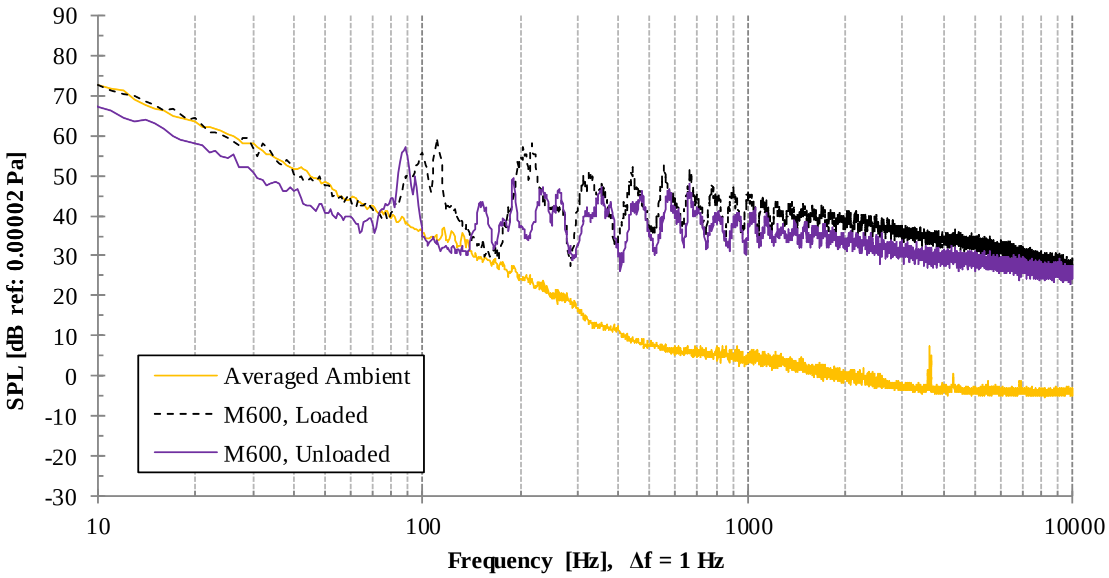

Figure 55: Narrowband acoustic data of M600 hovering an altitude of 36 ft, loaded and unloaded, microphone 2 (see Figure 20)

An important note about this data is that there is more than just a single clearly distinguishable BPF (blade passing frequency) for this aircraft, but instead a cluster of peaks around a specific frequency. This is due to the multiple rotors all operating independently of each other, with independently varying RPM [31]. Figure 56 shows the variation in motor RPM during steady hover, which can be attributed to imperfect weight distribution and, in certain cases, steady wind. Based on the motor schematic shown, it appears that the platform may be carrying extra weight towards motors one and six.

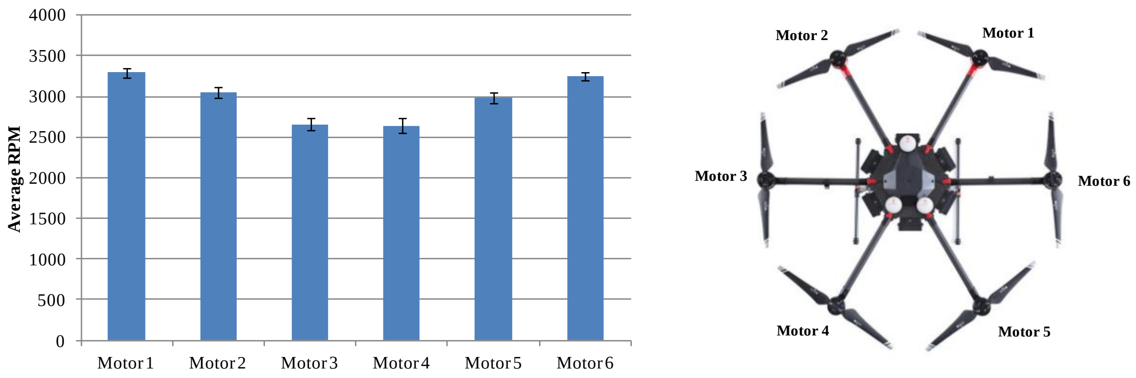

Figure 56: Average RPM with standard deviation error bars for a 10 second period of stable hover at an altitude of 36ft. Orientation of motors shown on the right.

4.3.5 Analytical Source Combination

Following the procedure detailed in Chapter 3, the far-field acoustic data for the engine obtained in Stage 1 is isolated from the other contributing signatures (propeller, ambient, etc.). What we will assume to be the fully isolated signature of the engine is shown in Figure 57. While there exists some broadband contribution from the engine, the most significant contribution is the tonal content the is clearly visible at 100 Hz and the corresponding harmonics.

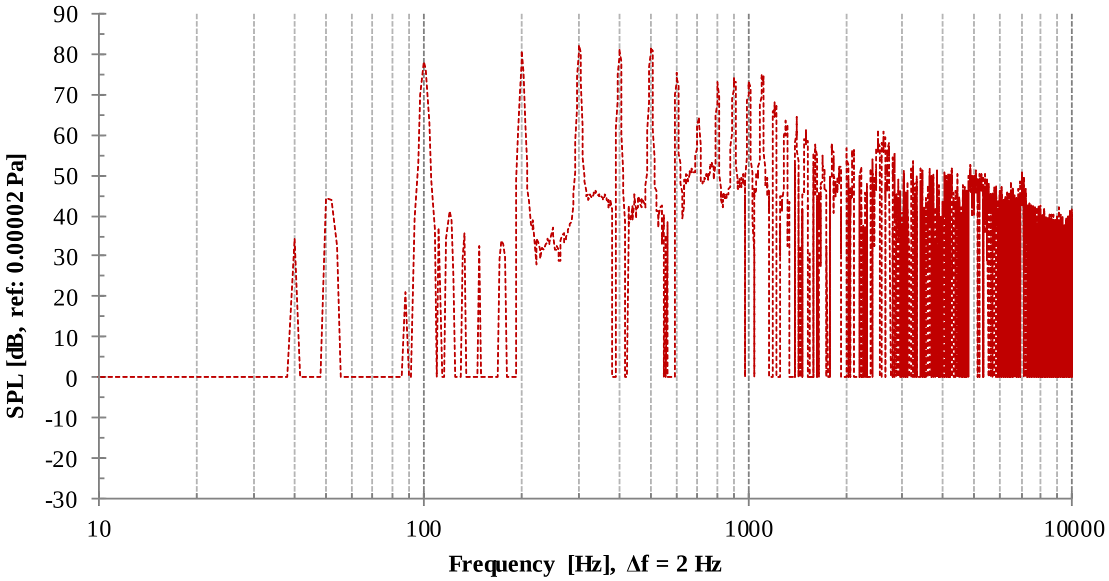

Figure 57: Analytically extracted acoustic signature of the DA50

After a distance correction of the engine data, and the compression of the M600 acoustic data to a Δf of 2Hz to match the engine data, the engine and aircraft signatures have been analytically combined. The results of these computations are shown in Figure 58, as well as the original M600 signature and the corresponding ambient. The OASPL (80-10,000 Hz) for each data set is given in the legend. It is important to note what acoustic affects the analytical combination does not consider but could affect the actual combined acoustic signature such as interaction noise, constructive or destructive interference, reflection, etc.

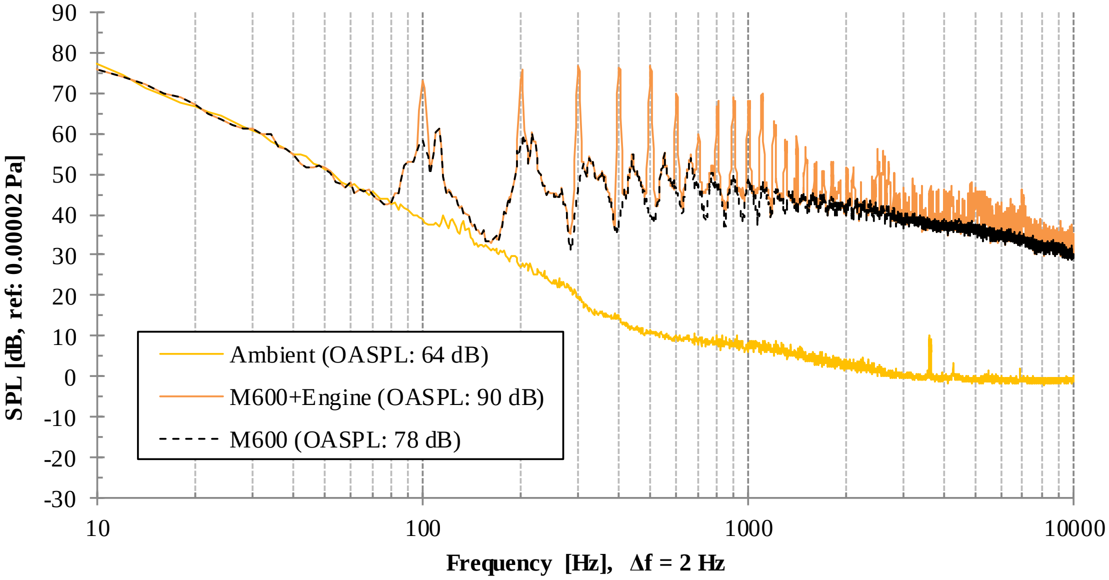

Figure 58: Analytically combined M600 and DA50 acoustic signatures, rectified to the same measurement distance, in comparison with the original M600 signature and corresponding ambient. OASPL calculated from 80 to 10,000 Hz.

This is the analytically produced acoustic behavior of the platform with additional weight and the noise from the engine. Coincidentally, the BPF of the platform's propellers (spinning at an average of 3000 RPM in hover) aligns with the firing frequency of the engine running at 6000 RPM, which is approximately 100 Hz. This alignment would vary with different platform configurations and varying RPM of propellers throughout flight. As expected, the engine signature's greatest contribution to the overall signature is the massive tonal content at 100 Hz and the corresponding harmonics. This contribution can also be seen when comparing the OASPL for each data set. The OASPL range of 80-10,000 Hz is chosen to avoid the low frequencies where broadband wind noise dominates. Within this range, there is an increase of 12dB in the aircraft signature with the addition of the engine.

4.3.6 Precision Uncertainty

Precision uncertainty for the acoustic data is calculated as the standard deviation of three different measurements of the same source, computed at each individual frequency. The results of this analysis are shown for the loaded M600 measurements and the engine with propeller measurements (Figure 59 and Figure 60).

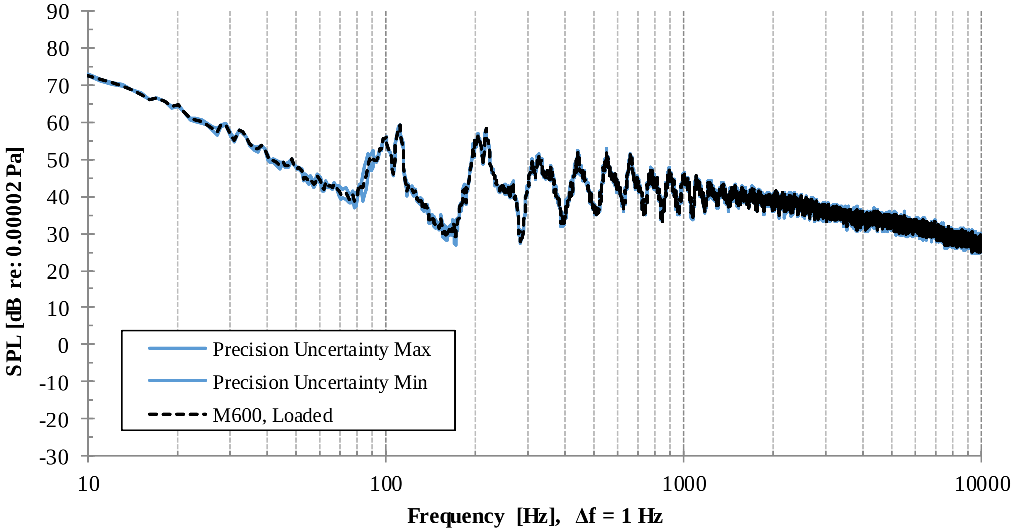

Figure 59: The precision uncertainty minimum and maximum values associated with the loaded M600 acoustic signature.

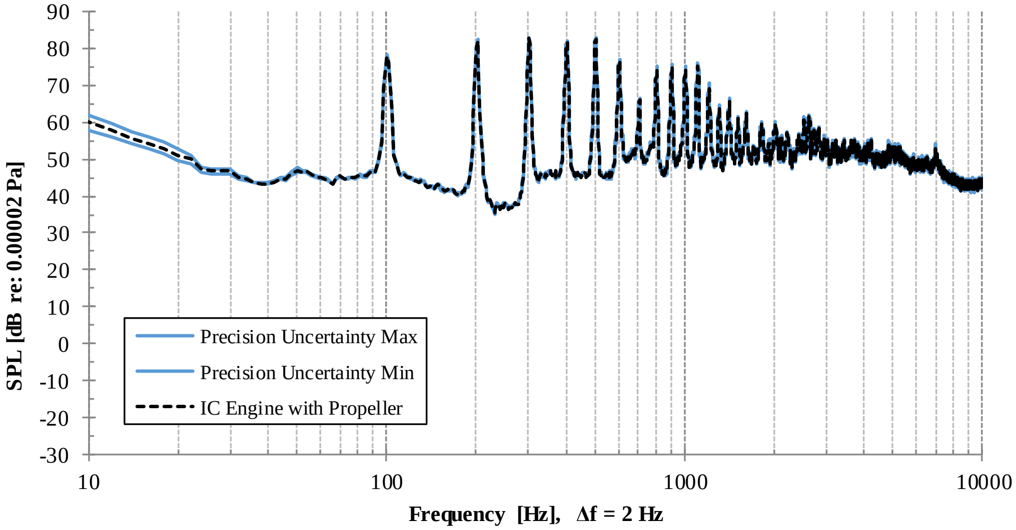

Figure 60: The precision uncertainty minimum and maximum values associated with the acoustic signature of the engine loaded by a propeller.

The bias uncertainty associated with the acoustic data collection equipment (Table 9) is also plotted as minimum and maximum boundaries for the loaded M600 and engine with propeller measurements (Figure 61 and Figure 62).

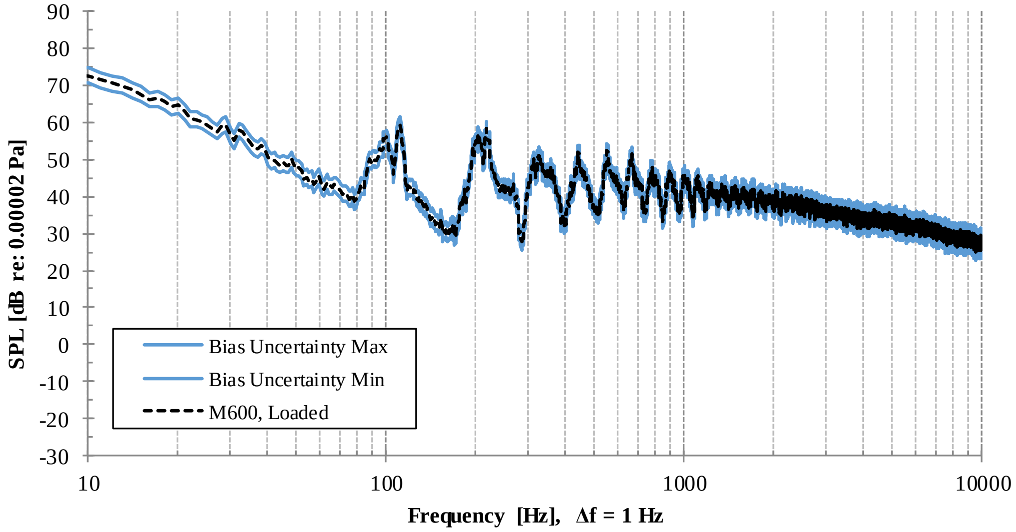

Figure 61: Bias uncertainty associated with the loaded M600 acoustic signature

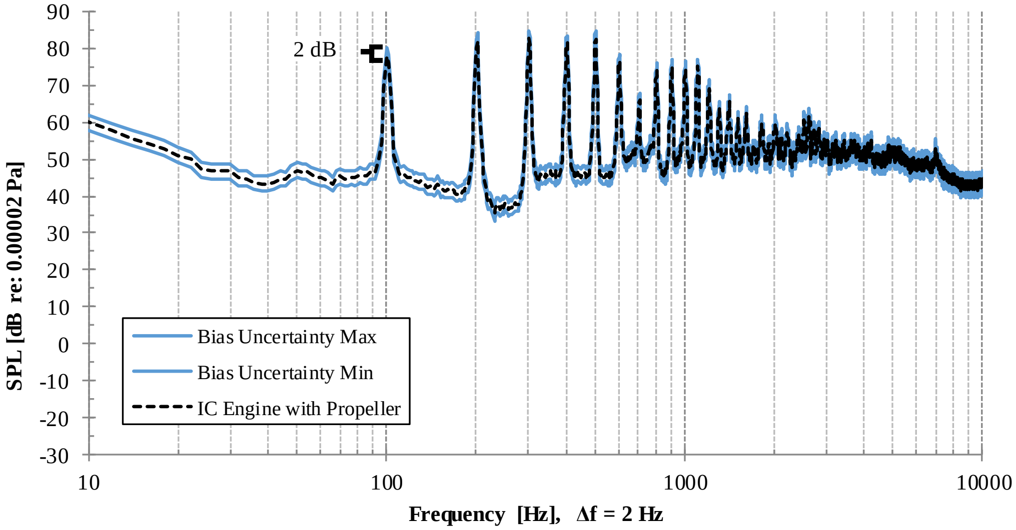

Figure 62: Bias uncertainty associated with the acoustic signature of the engine loaded by a propeller.

CHAPTER V

DISCUSSION & CONCLUSIONS

The ultimate goal of this research was to fully characterize the implications of implementing a small internal combustion engine as a mechanical power source in a hybrid-electric power system for a multi-rotor UAS. Short of fully designing and implementing the theoretical hybrid-electric power system discussed, the experiments conducted were successful in meeting this goal.

As expected, based on previous research, the vibration, cooling requirements, and noise of small internal combustion engines each present a unique and intricate challenge when considering integration with multi-rotor UAS platforms. Small internal combustion engines produce powerful vibrations in multiple axes, and even simplified replication of this vibration was shown to have a noticeable effect on the function of a multi-rotor sUAS. In the course of this study it became apparent that quantifying vibration is heavily dependent upon the physical characteristics of the test setup, and without fully integrating this engine on a flying multi-rotor platform, the affects cannot be perfectly replicated. However, strong vibrations clearly impede the critical functions of the on-board sensors, making vibration a very significant consideration when designing a hybrid power system for multi-rotor sUAS.

It is also shown that forced convection is required to cool a small internal combustion engine utilizing intermittent combustion (piston engine) and experimental estimates of the amount of flow required were made. Convection cooling theory is also used to predict based on power output how much cooling will be required.

To assess the feasibility of adding cooling solutions to the hybrid power system design, estimates are made of the amount of design margin (of weight and power) for a theoretical hybrid and platform combination that could be used for external cooling (Figure 63). With correct sizing and careful design, the necessity for external cooling should not negate the endurance benefits of a hybrid power system.

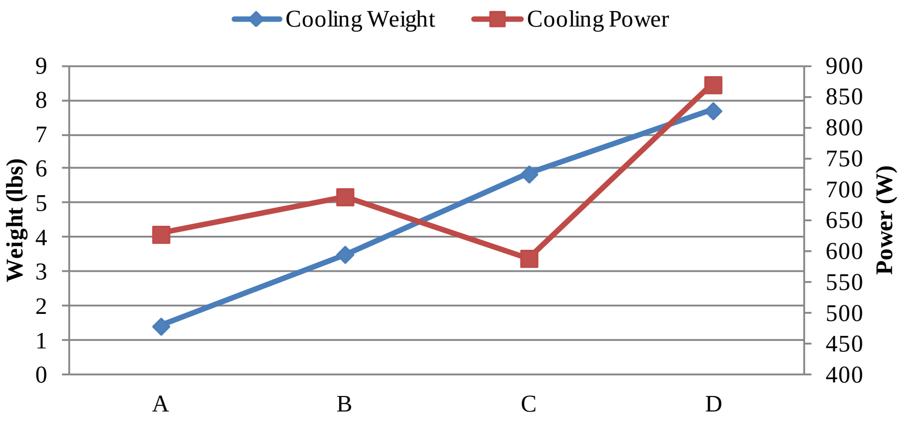

Figure 63: Estimates of the design margin for cooling hardware weight and electrical power for the four theoretical hybrid configurations discussed in Chapter 2 (TABLE).

Along with initial characterization of the single-cylinder two-stroke internal combustion engine noise signature, an analytical prediction of the combined signature of a multi-rotor sUAS with an engine on-board has been presented. The results of the characterization indicate that the engine, which produces mechanical and combustion-related noise, has a significant amount of tonal content as well as some broadband, and a significant amount of noise overall. To more fully assess the independent signature of the engine (without the noise of the propeller that was used in this study to apply load during operation), other known contributing signatures were computationally removed. The isolated signature also clearly showed major tonal content with some broadband as well in the low to mid frequency range (approximately 80 to 1500 Hz). When analytically combined with the measured acoustic signature of a hex-configuration (6 rotors) multi-rotor sUAS, it is clear that the most significant contribution of the engine is the tonal content, which has the potential to increase the overall signature by 12dB (Figure 64). While noise may not be a critical concern for all sUAS applications, if noise mitigation is required, it must be effective specifically for major tonal content.

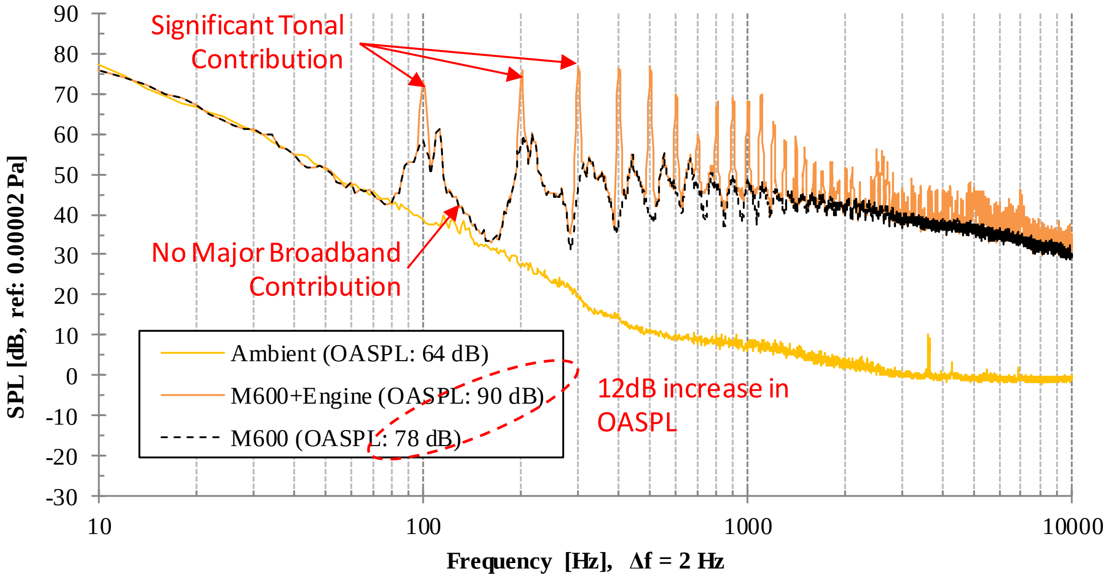

Figure 64: Analytically produced hybrid signature, with notable features highlighted. OASPL calculated from 80 to 10,000 Hz.

The challenges discussed herein, viz. vibration, cooling, and noise, while significant, are not the only ones that must be faced when designing a viable hybrid-electric power system for integration with multi-rotor sUAS. Other considerations such as effective power management, space claim (proper component placement), and general system robustness must be made as well. Future work for this subject includes the full design and implementation of a hybrid-electric power system that is compatible with COTS sUAS and could be used as an endurance booster. While there are benefits to a system that can be implemented on any platform, the biggest opportunity lies one step further: the intentional design of a complete hybrid-electric multi-rotor sUAS. This type of approach would offer even more flexibility in tackling the major integration challenges identified and characterized in this study. It is also worth pursuing what other classes of UAS could benefit from this type of power system, as only rotary wing sUAS are considered in this study. Applications to small fixed wing systems and larger vehicles, both manned and unmanned in fixed wing and rotary wing configurations, are also of great interest.

REFERENCES

[1] F. Nex and F. Remondino, “UAV for 3D Mapping Applications: A Review,” *Applied Geomatics,* pp. 1-15, 2014.

[2] M. J. Logan, J. Chu, M. A. Motter, D. L. Carter, M. Ol and C. Zeune, “Small UAV Research and Evolution in Long Endurance Electric Powered Vehicles,” in *AIAA Infotech@Aerospace Conference and Exhibit*, Rohnert Park, CA, 2007.

[3] "5 Hour Endurance Multirotors," Skyfront, 2017. [Online]. Available: https://skyfront.com/. [Accessed May 2018].

[4] "GE35 Range Extender," Pegasus, [Online]. Available: http://www.pegasusaero.ca/ge35-range-extender. [Accessed May 2018].

[5] "Hybrix.20," Quaternium, 2017. [Online]. Available: http://www.quaternium.com/uav/hybrix-20/. [Accessed May 2018].

[6] T. Hays, *High Energy Density Propulsion Systems and Small Engine Dynamometer,* Stillwater, OK: M.S. thesis, Dept. Mech. Aero. Eng.,Oklahoma State Univ., Stillwater, OK, 2007.

[7] K. Morita, “Automotive Power Source in 21st Century,” *JSAE Review,* pp. 3-7, 2003.

[8] Y. Gao and M. Ehsani, “Hybrid Electric Vehicle: Overview and State of the Art,” *IEEE ISIE,* 2005.

[9] O. Gonzalez-Espasandin, T. J. Leo and E. Navarro-Arevalo, “Fuel Cells: A Real Option for Unmanned Aerial Vehicles Propulsion,” *The Scientific World Journal*, 2014.

[10] L. Karunarathne, Economou and K. Knowles, “Power and Energy Management System for Fuel Cell Unmanned Aerial Vehicle,” *Proceedings of Institution of Mechanical Engineers,* vol. 226, pp. 437-454, 2011.

[11] S. Menon, N. Moulton and C. Cadou, “Development of a Dynamometer for Measuring Small Internal-Combustion Engine Performance,” *Journal of Propulsion and Power,* vol. 23, no. 1, pp. 194-202, 2007.

[12] F. G. Harmon, A. A. Frank and S. S. Joshi, “The control of a parallel hybrid-electric propulsion system for a small unmanned aerial vehicle using a CMAC neural network,” *Neural Networks,* vol. 18, pp. 772-780, 2005.

[13] F. Harmon, A. A. Frank and J. J. Chattot, “Conceptual Design and Simulation of a Small Hybrid-Electric Unmanned Aerial Vehicle,” *Journal of Aircraft,* vol. 43, no. 5, pp. 1490-1498, 2006.

[14] J. Y. Hung and L. F. Gonzalez, “On Parallel Hybrid-Electric Propulsion System for Unmanned Aerial Vehicles,” *Progress in Aerospace Sciences,* pp. 1-17, 2012.

[15] M. D. Hageman and C. Wisniewski, “Development and Analysis of a Group 1 UAC Series Hybrid Power System with Two Engine Options,” in *AIAA Propulsion and Energy Forum,* Salt Lake City, UT, 2016.

[16] X. Liu and R. B. Randall, “Blind Source Separation of Internal Combustion Engine Piston Slap From Other Measured Vibration Signals,” *Mechanical Systems and Signal Processing,* vol. 19, no. 6, pp. 1196-1208, 2005.

[17] J. Yang, H. Zhi-yong and Z. Xu, “Comparison of different techniques for time-frequency analysis of,” *Journal of Zhejiang University,* vol. 12, no. 7, pp. 519-531, 2011.

[18] Z. Geng, J. Chen and J. B. Hull, “Analysis of engine vibration and design of an applicable,” *International Journal of Mechanical Sciences,* no. 45, pp. 1391-1410, 2003.

[19] DJI, “Spreading Wings S1000 Specs,” DJI, 2017. [Online]. Available: https://www.dji.com/spreading-wings-s1000/spec. [Accessed 3 December 2017].

[20] DJI, “Matrice 600 Specs,” DJI, 2017. [Online]. Available: https://www.dji.com/matrice600/info. [Accessed 3 December 2017].

[21] Rise Above, “Gryphon Dynamics GD-28X ARF Endurance Drone (X8 1400mm Super Frame),” Rise Above, 2017. [Online]. Available: https://www.riseabove.com.au/gryphon-dynamics-gd-28x-arf-custom-build-x8-1400mm. [Accessed 3 December 2017].

[22] Max Amps, “LiPo 11,000 6S 22.2v Battery Pack,” Max Amps, 2017. [Online]. Available: https://www.maxamps.com/lipo-11000-6s-22-2v-battery-pack. [Accessed 3 December 2017].

[23] KDE Direct, “KDE5215XF-435 Performance Testing Data Sheet (KDE Direct Propellers),” 2017. [Online]. Available: https://cdn.shopify.com/s/files/1/0496/8205/files/KDE_Direct_XF_CF_Brushless_Performance_Testing_-_KDE5215XF-435.pdf?7734511287488513374. [Accessed 3 December 2017].

[24] W. T. Thompson, Theory of Vibration with Applications, Prentice Hall, 1981.

[25] A. D. Jones and G. L. Brown, “Determination of Two-Stroke Engine Exhaust Noise by the Method of Characteristics,” *Journal of Sound and Vibration,* vol. 82, no. 3, pp. 305-327, 1982.

[26] K. K. Ahuja, “Reliable Acoustic Measurements of Ducted and Unducted Rotors for use in Predicting Flyover Data,” in *DARPA/NASA Propeller-Rotor Acoustics Workshop*, NASA Langley Research Center, 2010.

[27] G. J. J. Ruijgrok, Elements of Aviation Acoustics, Delft, The Netherlands: VSSD, 2007.

[28] J. M. Seitzman, *Experimental Errors and Unceratinty: An Introduction,* Georgia Tech College of Engineering, unpublished.

[29] G. P. Blair, Design and Simulation of Two-Stroke Engines, Warrendale, PA: Society of Automotive Engineers, 1996.

[30] H. H. Hubbard, Aeroacoustics of Flight Vehicles: Theory and Practice. Volume 1. Noise,

vol. 1, Ft. Belvoir: Defence Technical Information Center, 1991.

[31] J. A. Feight, G. Donnell, J. D. Jacob and R. J. Gaeta, “Progress Towards Detection and Identification of sUAS via Acoustic Signature,” in *AIAA/CEAS Aeroacoustics Conference*, Denver, 2017.

[32] "Alternators," Sullivan Unmanned Vehicle, 2018. [Online]. Available: http://www.sullivanuv.com/products/alternators/. [Accessed May 2018].

[33] “Desert Aircraft,” Desert Aircraft, 2018. [Online]. Available: https://www.desertaircraft.com/collections/da-engines/products/da-50r. [Accessed April 2018].

[34] "Turnigy RotoMax 50cc Size Brushless Outrunner Motor," Hobby King, 2018. [Online]. Available: https://hobbyking.com/en_us/turnigy-rotomax-50cc-size-brushless-outrunner-motor.html. [Accessed May 2018].

[35] "Vibration Damping Sandwich Mounts," McMaster-Carr, [Online]. Available: https://www.mcmaster.com/#vibration-damping-sandwich-mounts/=1cop63u. [Accessed May 2018].

APPENDICES

i. Power System Sizing[32]

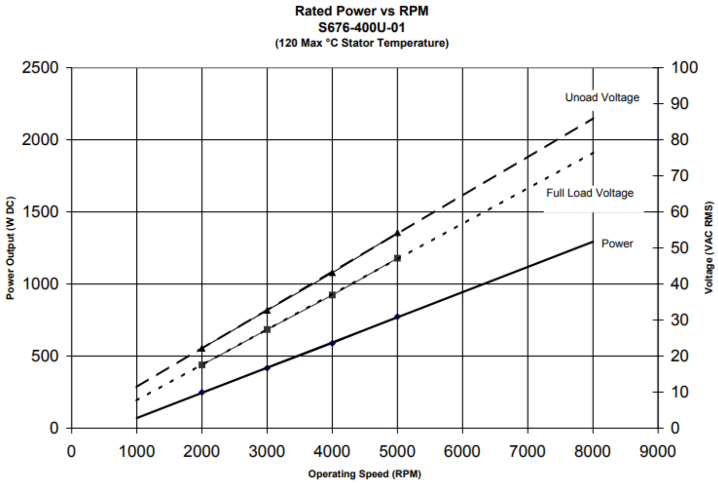

Figure 65: Performance chart for Sullivan UV S676-400U-01

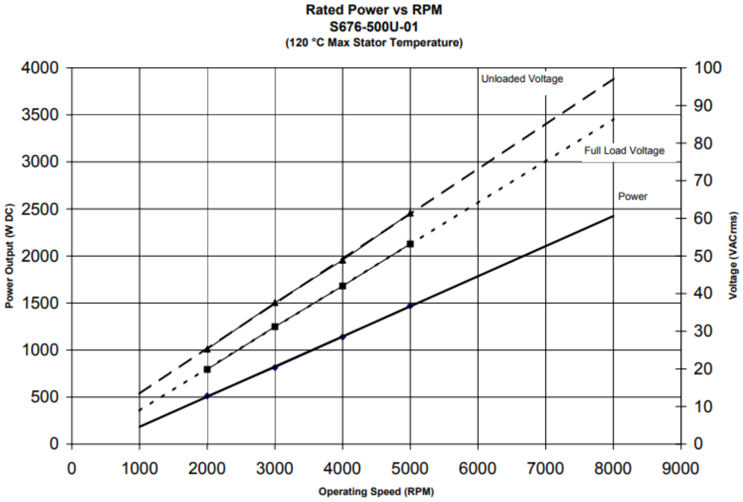

Figure 66: Performance chart for Sullivan UV S676-500U-01

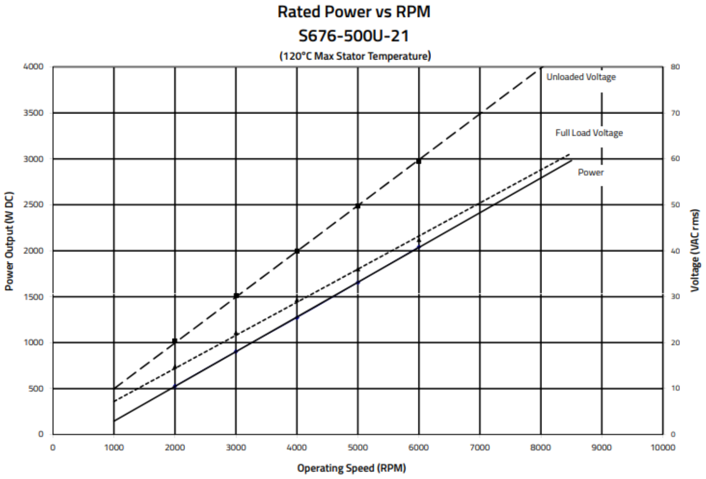

Figure 67: Performance chart for Sullivan UV S676-500U-21

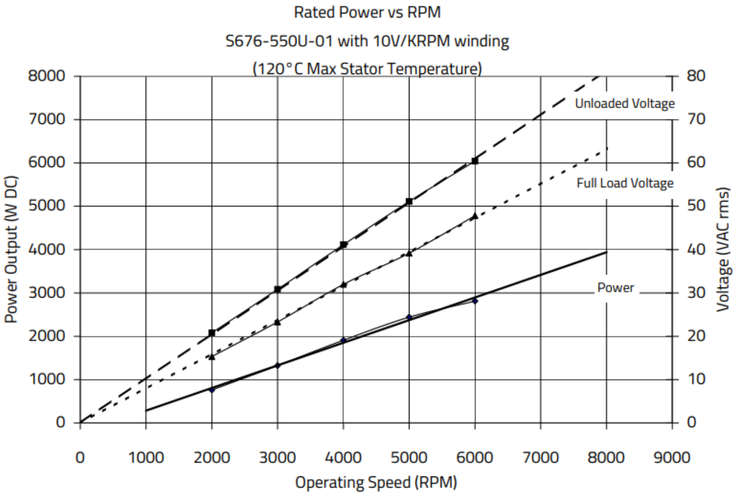

Figure 68: Performance chart for Sullivan UV S676-550U-01

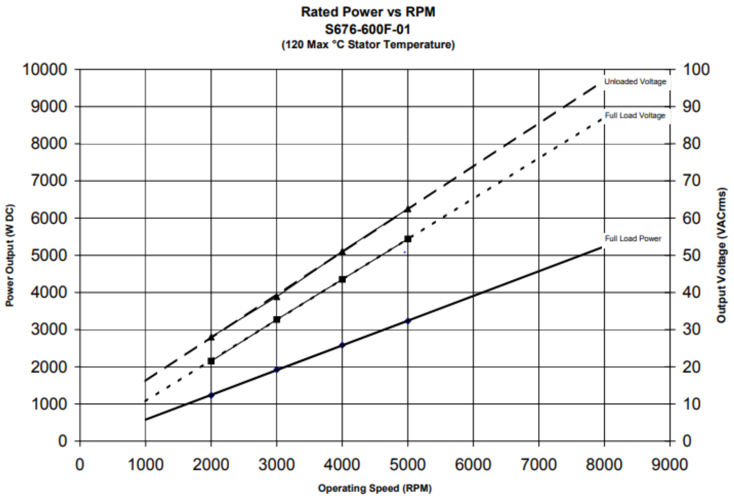

Figure 69: Performance chart for Sullivan UV S676-600F-01

ii. Additional Vibration Data

a. Octagon Flight (March 2018)

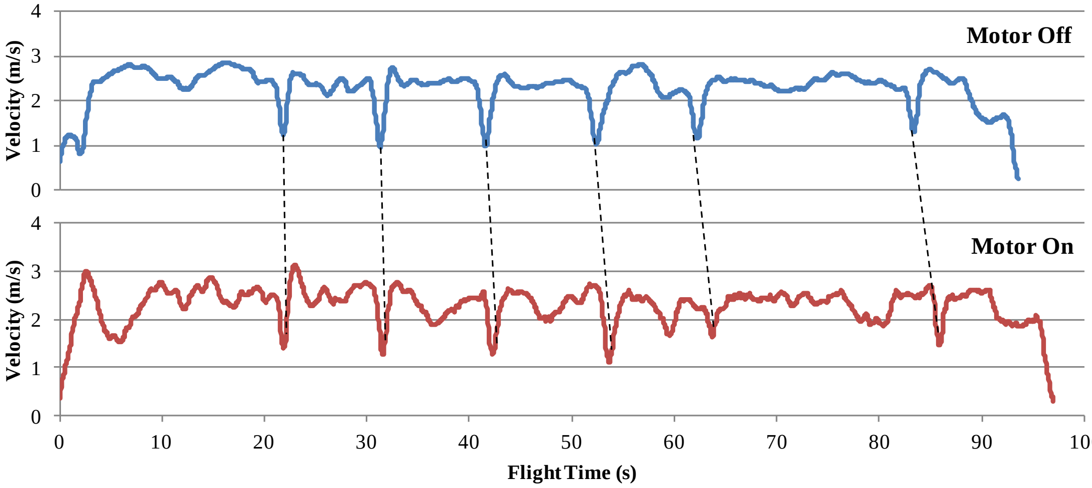

Figure 70: Comparison of velocity behavior between octagon waypoint flights with electric motor (with cam) off and on. Due to the different flight times, regions of similar flight behavior are marked with dotted lines.

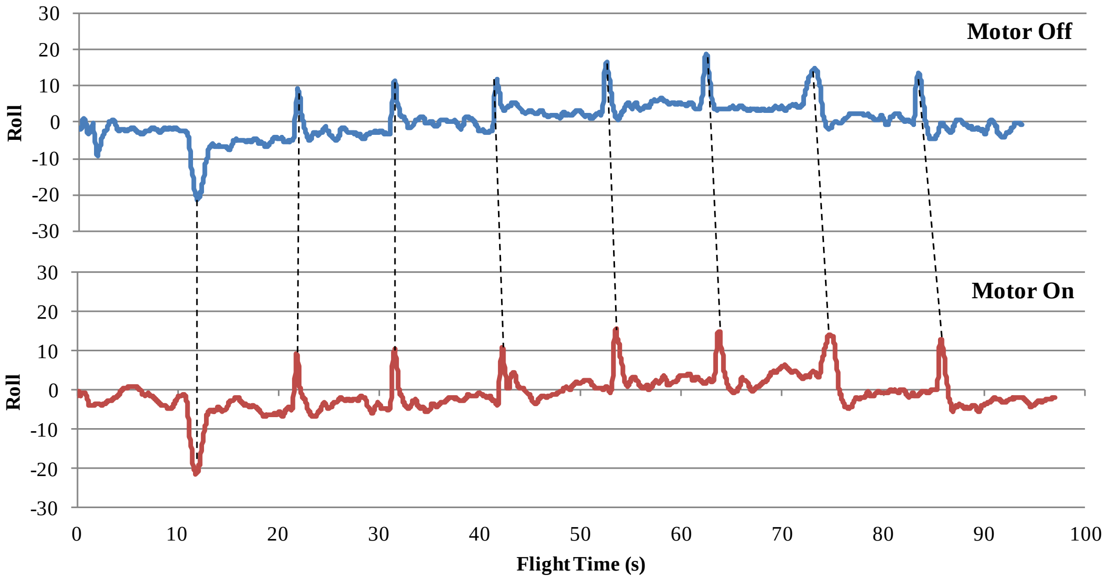

Figure 71: Comparison of platform roll between octagon waypoint flights with electric motor (with cam) off and on. Due to the different flight times, regions of similar flight behavior are marked with dotted lines.

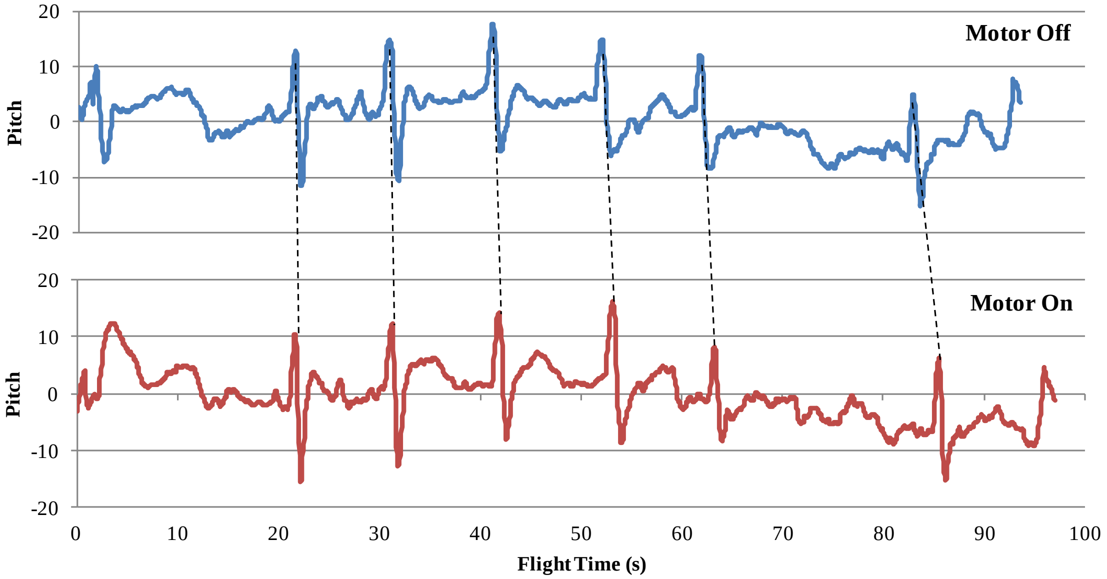

Figure 72: Comparison of platform pitch between octagon waypoint flights with electric motor (with cam) off and on. Due to the different flight times, regions of similar flight behavior are marked with dotted lines.

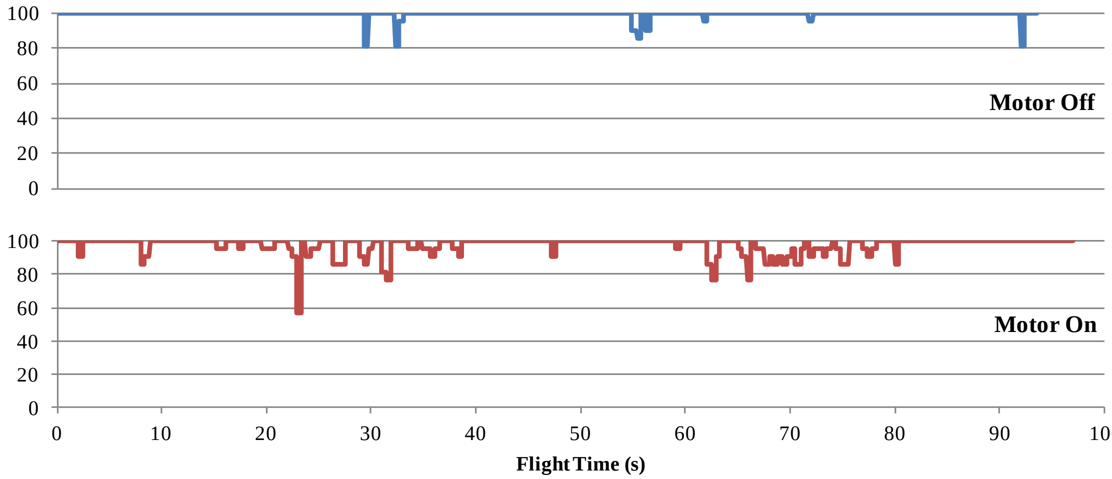

Figure 73: Comparison of signal strength between octagon waypoint flights with electric motor (with cam) off and on. Due to the different flight times, regions of similar flight behavior are marked with dotted lines.

b. Point to Point Flight (March 2018)

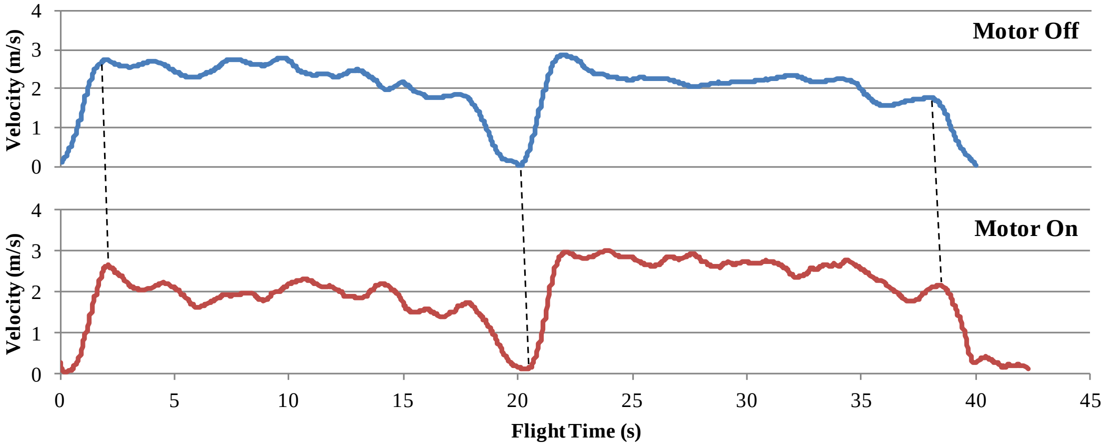

Figure 74: Comparison of velocity behavior between point-to-point flights with electric motor (with cam) off and on. Due to the different flight times, regions of similar flight behavior are marked with dotted lines.

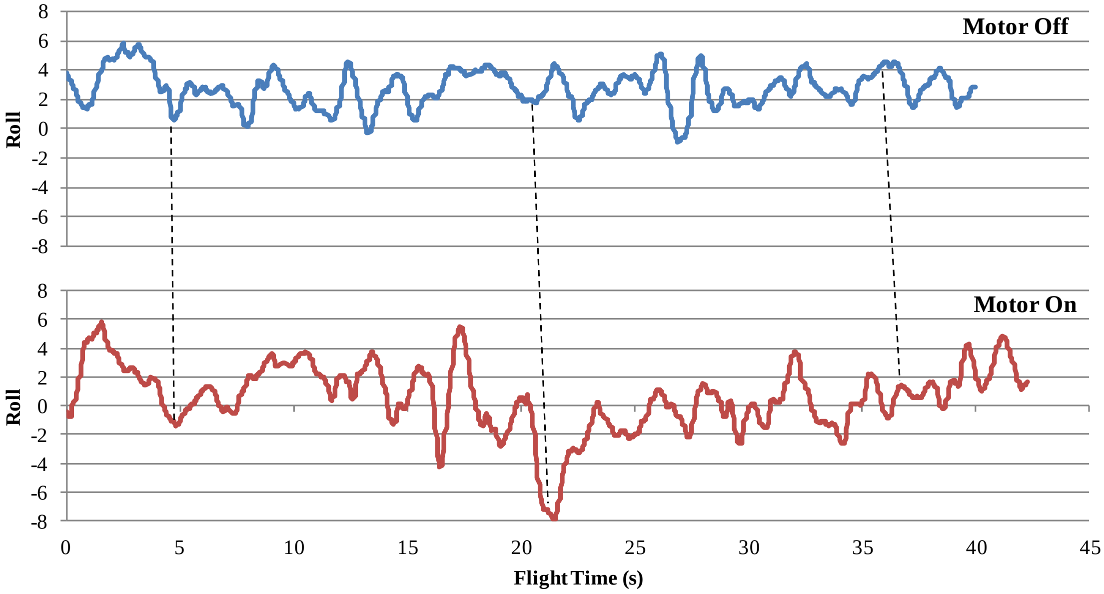

Figure 75: Comparison of platform roll between point-to-point flights with electric motor (with cam) off and on. Due to the different flight times, regions of similar flight behavior are marked with dotted lines.

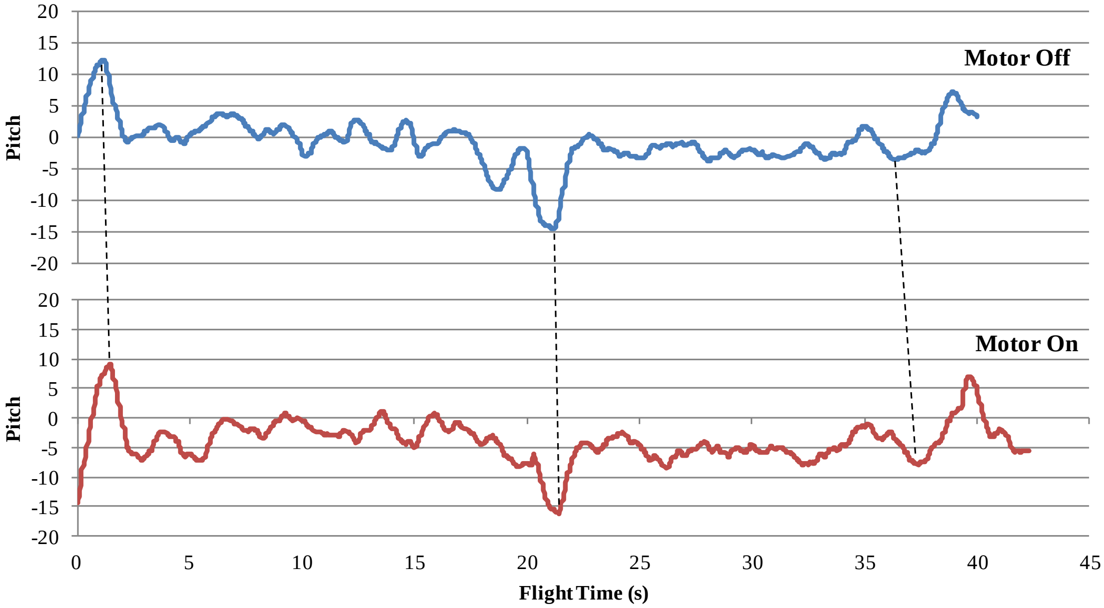

Figure 76: Comparison of platform pitch between point-to-point flights with electric motor (with cam) off and on. Due to the different flight times, regions of similar flight behavior are marked with dotted lines.

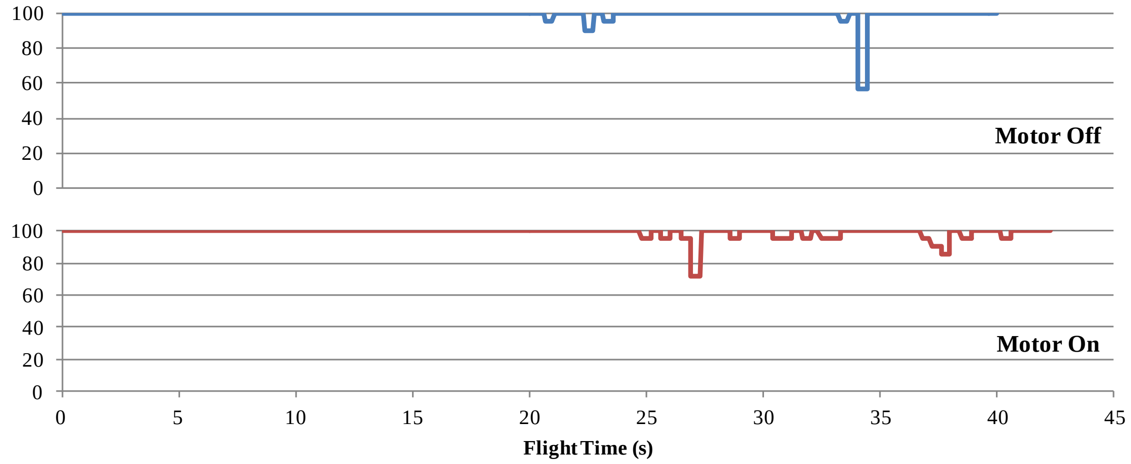

Figure 77: Comparison of signal strength between point-to-point flights with electric motor (with cam) off and on. Due to the different flight times, regions of similar flight behavior are marked with dotted lines.

iii. Additional Noise Data

a. Analytical Source Combination

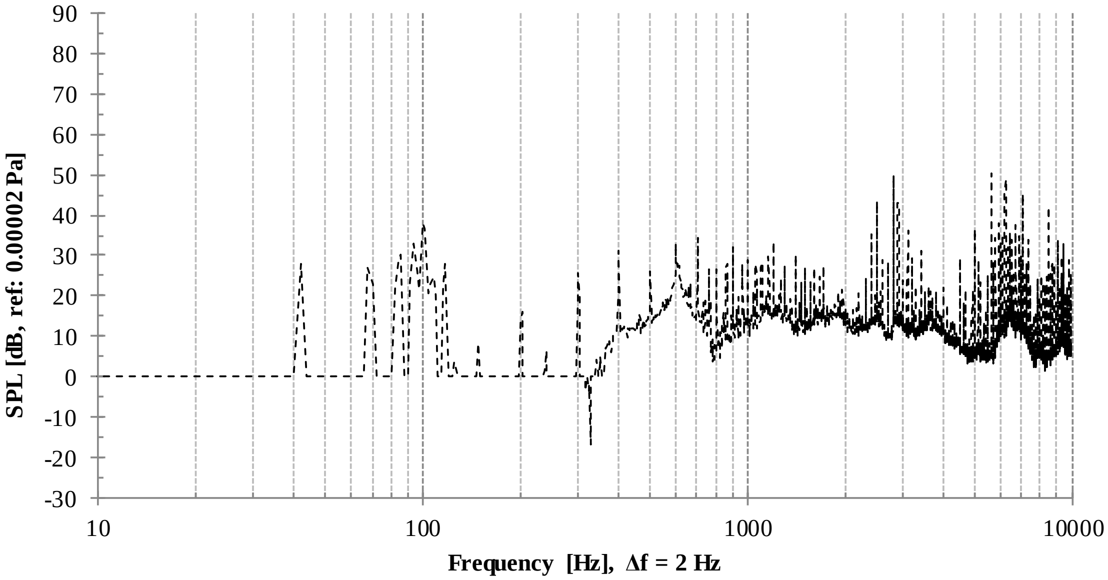

Figure 78: Analytically subtracted narrowband acoustic spectra for the electric motor only, derived from the narrowband acoustic spectra shown in Figure 54

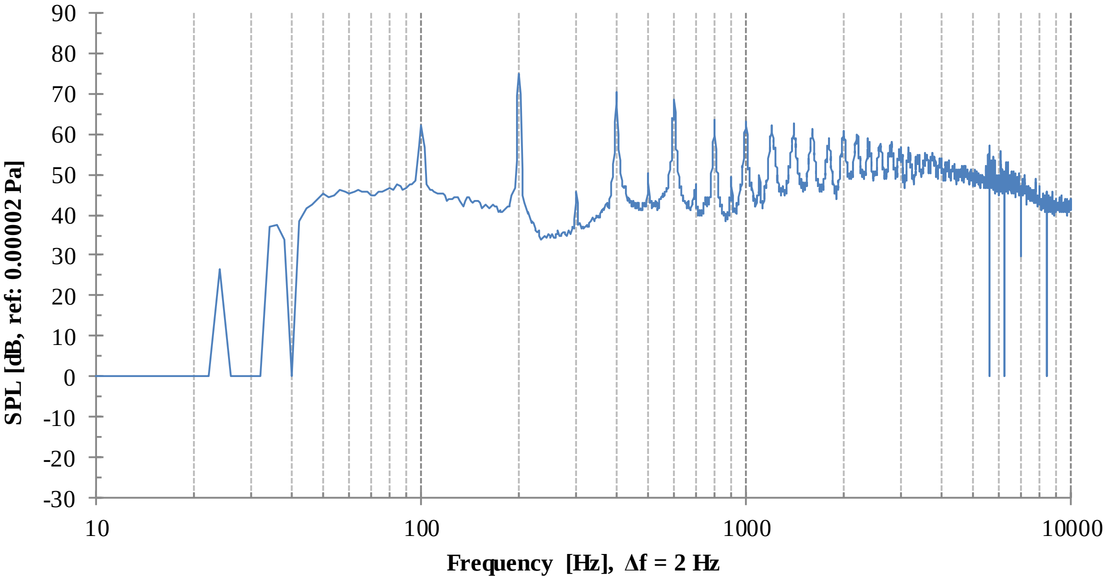

Figure 79: Analytically subtracted narrowband acoustic spectra for the 22x8 wooden propeller only, derived from the narrowband acoustic spectra shown in Figure 54

b. Vibration Affect of Acoustic Signature

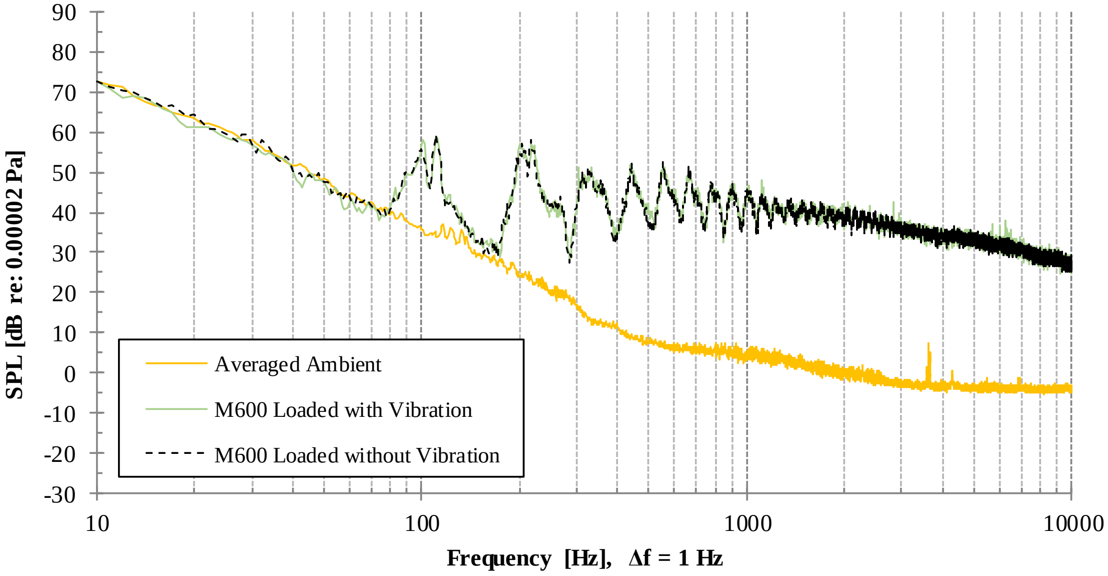

Figure 80: Comparison of the loaded M600 with and without the electric motor active and producing additional vibration to show if the vibration has any significant affect on the acoustic signature of the aircraft.

c. Microphone Comparison

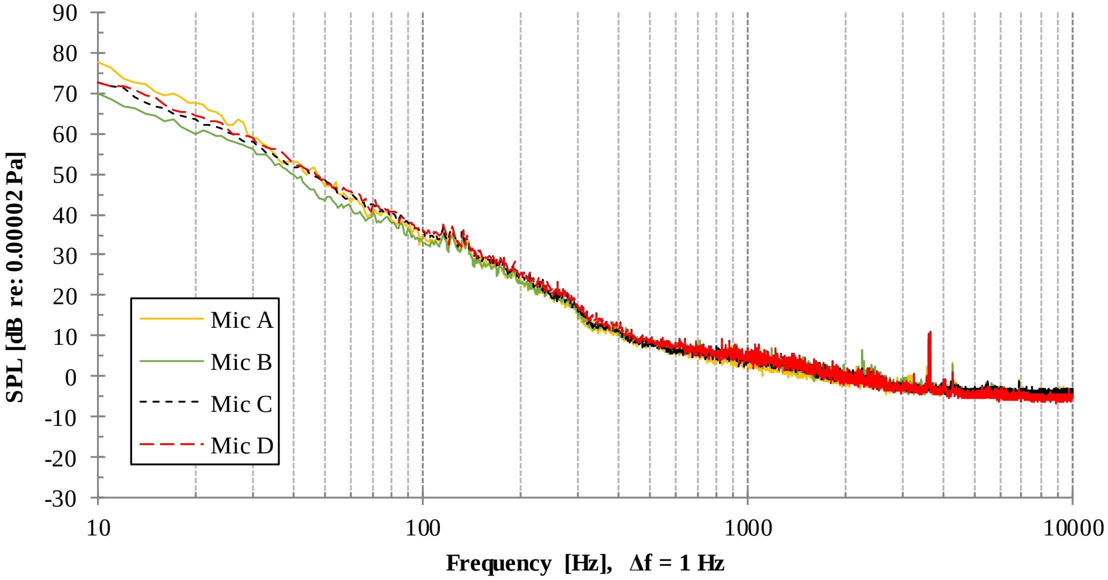

Figure 81: Averaged ambient measurements from all microphones in array for M600 flight tests

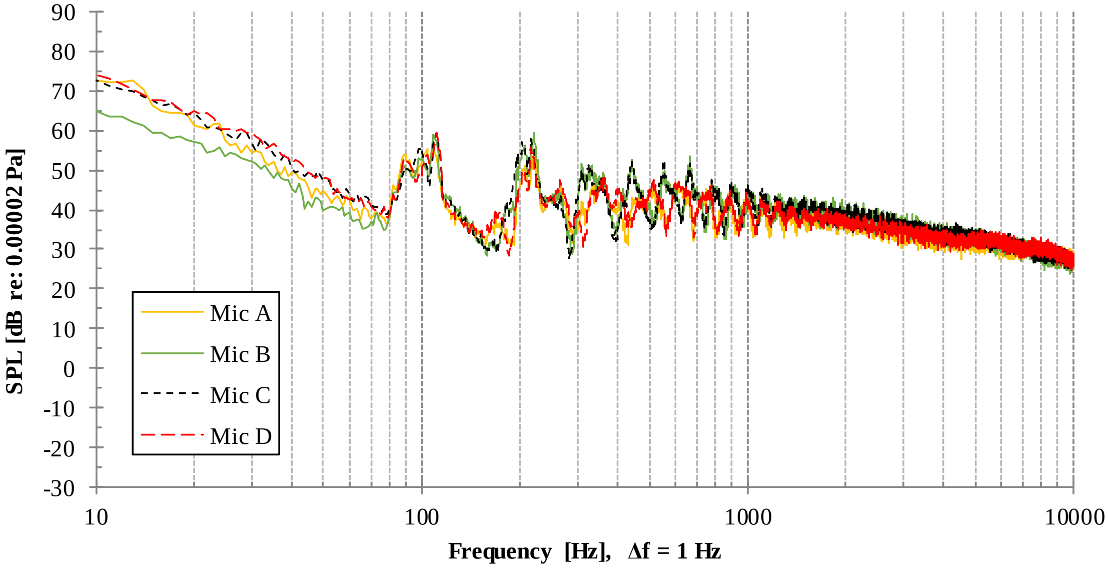

Figure 82: Loaded M600 acoustic signature from all 4 microphones in array

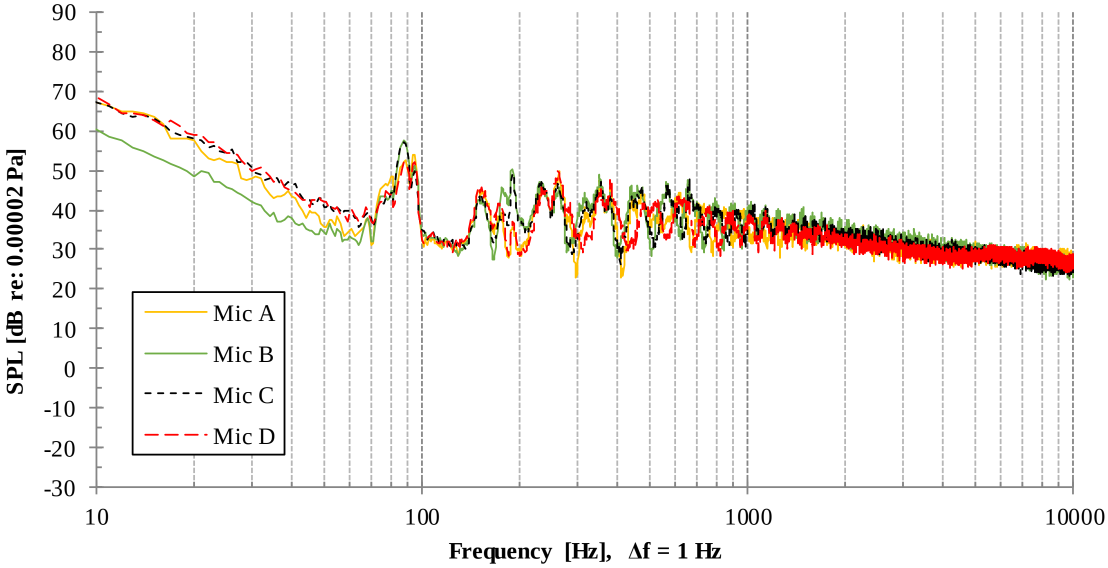

Figure 83: M600 Unloaded acoustic signature from all 4 microphones in array

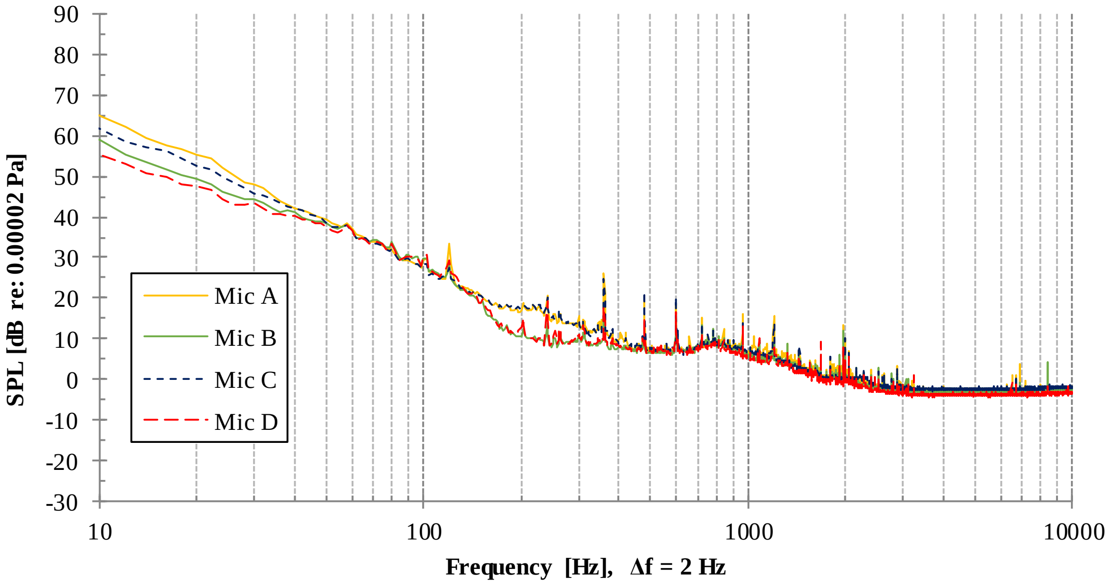

Figure 84: Averaged ambient measurement from all 4 microphones in array for engine field testing. Microphones A and C are at a height of 9ft, while microphones B and D are at a height of 4.5ft.

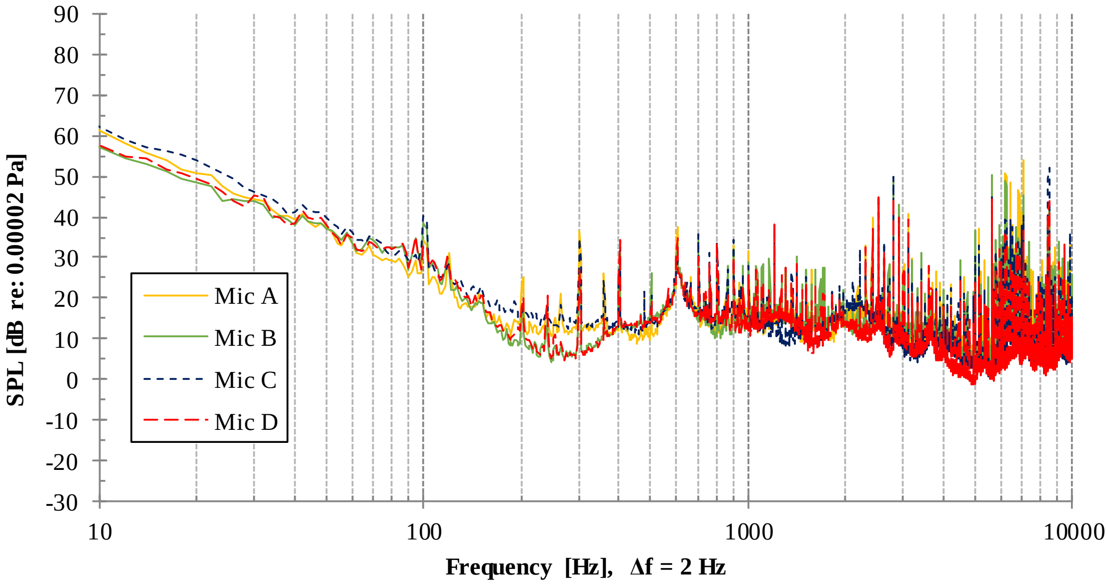

Figure 85: Acoustic signature of electric motor with no propeller from all 4 microphones in array. Microphones A and C are at a height of 9ft, while microphones B and D are at a height of 4.5ft.

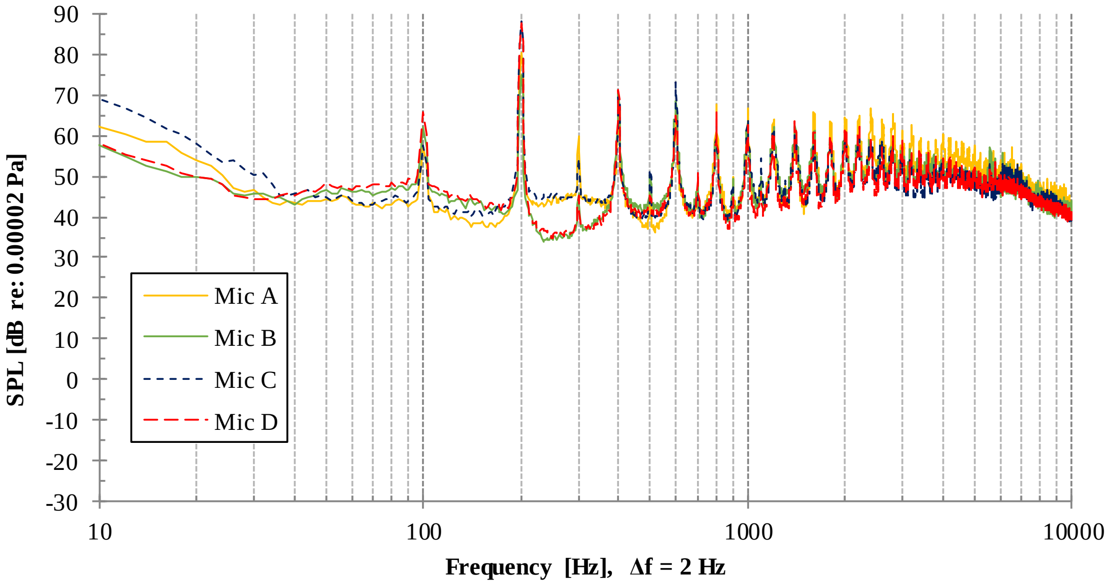

Figure 86: Acoustic signature of electric motor with propeller from all 4 microphones in array. Microphones A and C are at a height of 9ft, while microphones B and D are at a height of 4.5ft.

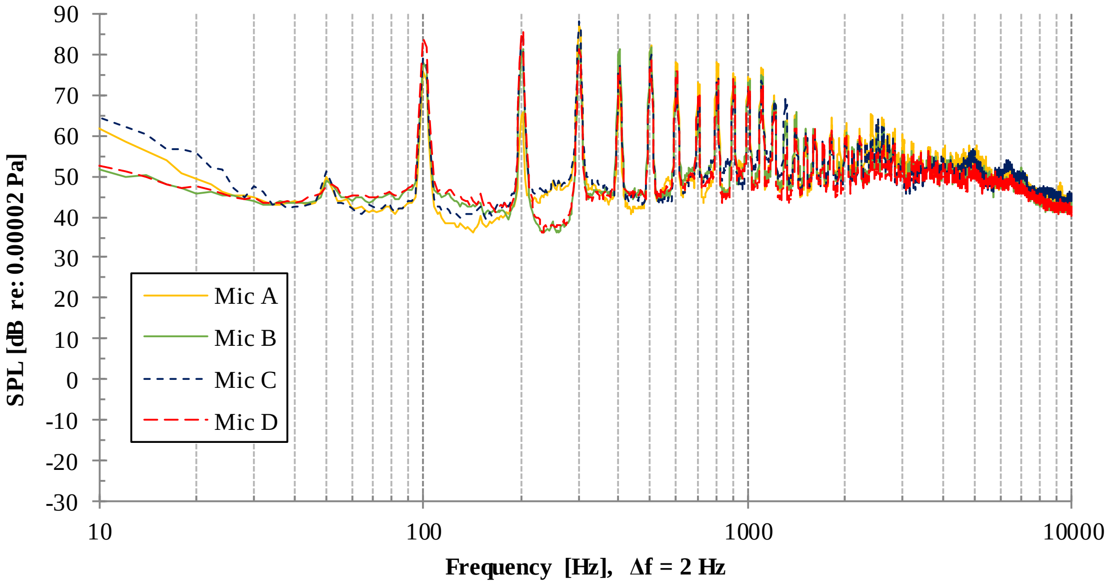

Figure 87: Acoustic signature of engine with propeller from all 4 microphones in array. Microphones A and C are at a height of 9ft, while microphones B and D are at a height of 4.5ft.

d. Ambient Weather Conditions

Table 18: **M600 Flight Testing (03/29/2018)**

Time	Temperature (F)	Pressure (psi)	Wind Speed (kts)	Humidity (%)
2:52 pm	58.6	14.19	6.3	60
3:16 pm	56.2	14.19	3, gusting 7	
3:25 pm			7, gusting 10	

Table 19: Engine Flight Testing (03/16/2018-03/17/2018)

Time	Temperature (F)	Pressure (psi)	Wind Speed (kts)	Humidity (%)
1:40 am	52.9	14.13	1.8, gusting 4.8	44.5
2:31 am	45.7	14.14	1, gusting 2.5	62
4:58 am	41.8	14.15	0.7	75.3

iv. Additional Specifications

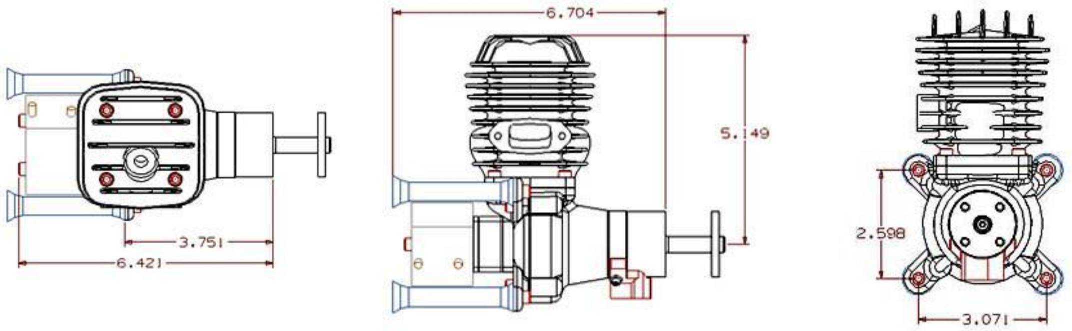

Displacement	50	cc
Weight	2.94	lbs
Bore	1.6771	in
Stroke	1.3779	in
Recommended Propellers	2-bladed: 23x8, 22x10, 22x8 3-bladed: 22x10n, 20x12, 20x10	

Figure 88: Desert Aircraft DA50 engine specifications [33]

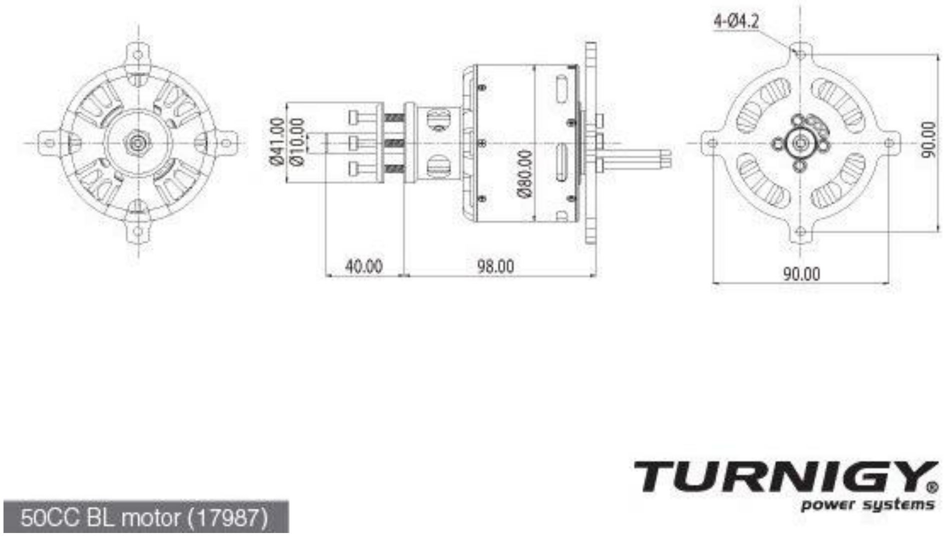

RPM	172 kv
Max Current	120 A
Watts	5300 W
No Load Current	44V/1.65A
Internal Resistance	0.021 ohm
Weight	1080 g
Diameter of Shaft	10 mm

Figure 89: Turnigy Rotomax 50cc electric motor specifications [34]

Table 20: Vibration-Dampening Sandwich Mount with Stud & Insert [35]

	Dampener A	**Dampener B**
Mount Type	Threaded Stud and Threaded Insert	Threaded Stud and Threaded Insert
Thread Size	1/4"-20	1/4"-20
Thread Type	UNC	UNC
Capacity per Mount	31 lbs.	75 lbs.
Deflection @ Capacity	0.07"	0.03"
Shear Capacity per Mount	4.5 lbs.	25 lbs.
Deflection @ Shear Capacity	0.06"	0.1"
Diameter	5/8"	1"
Height	5/8"	1/2"
Thread Length	1/2"	1/2"
Thread Depth	3/16"	3/16"
Hardness	Durometer 50A	Durometer 50A
Hardness Rating	Medium	Medium
System of Measurement	Inch	Inch
Shape	Round	Round
Material	Black Neoprene Rubber	Black Neoprene Rubber
Stud Material	Zinc-Plated Steel	Zinc-Plated Steel
Insert Material	Steel	Steel
Temperature Range	10° to 180° F	10° to 180° F
RoHS	Compliant	Compliant
Use these rubber sandwich mounts to minimize vibration between surfaces inside machinery and equipment, such as in circuit boards, small fans, compressors, and pumps. They're for use in compression and shear load applications. Neoprene rubber has good resistance to weather and acids and moderate resistance to oils.		

v. Schematics and Pictures

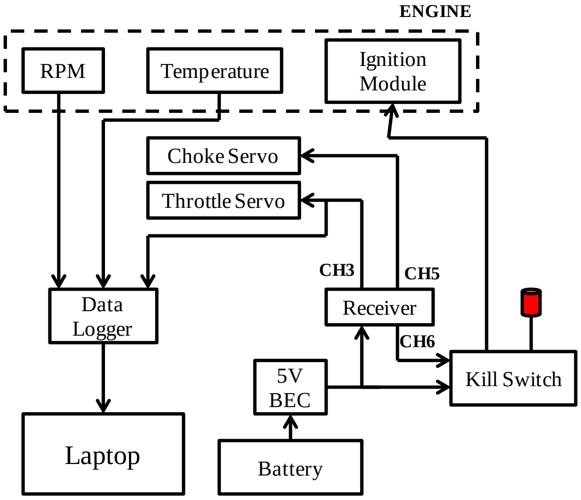

Figure 90: Engine wiring schematic

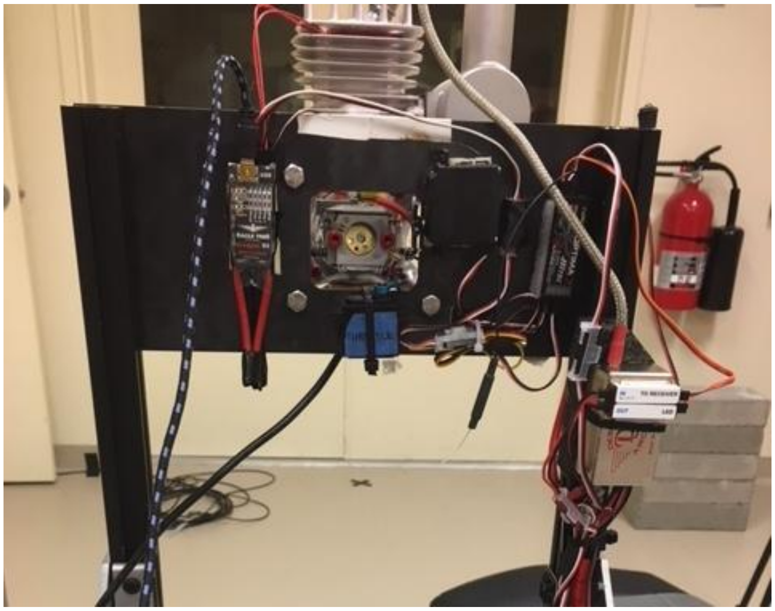

Figure 91: Engine sensors and wiring

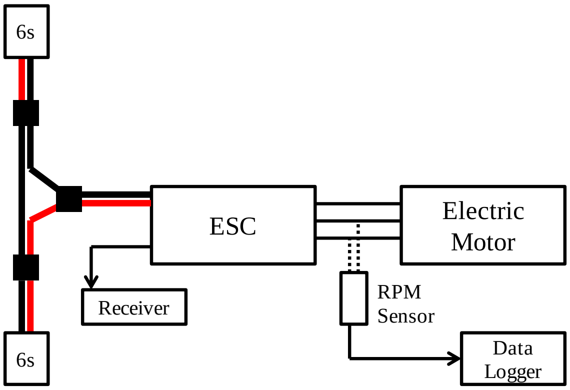

Figure 92: Electric motor electronics schematic

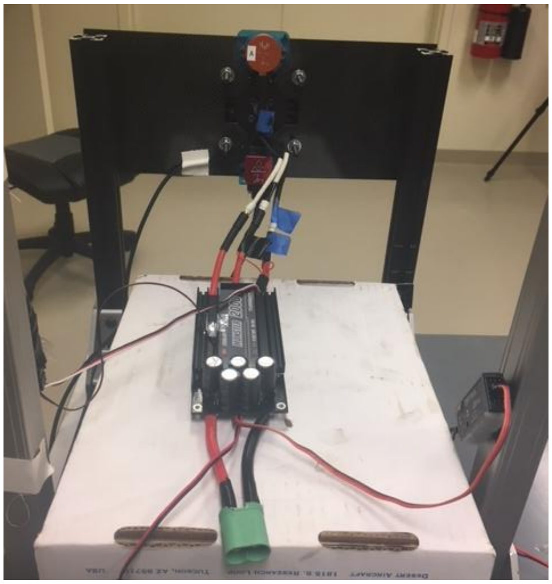

Figure 93: Electric motor electrical and sensor connections

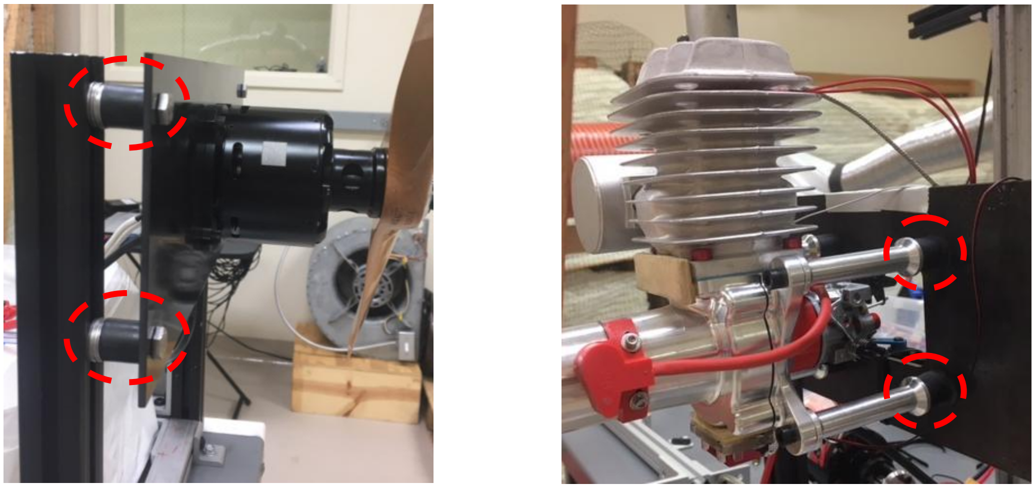

Figure 94: Additional Dampener Placement Figures

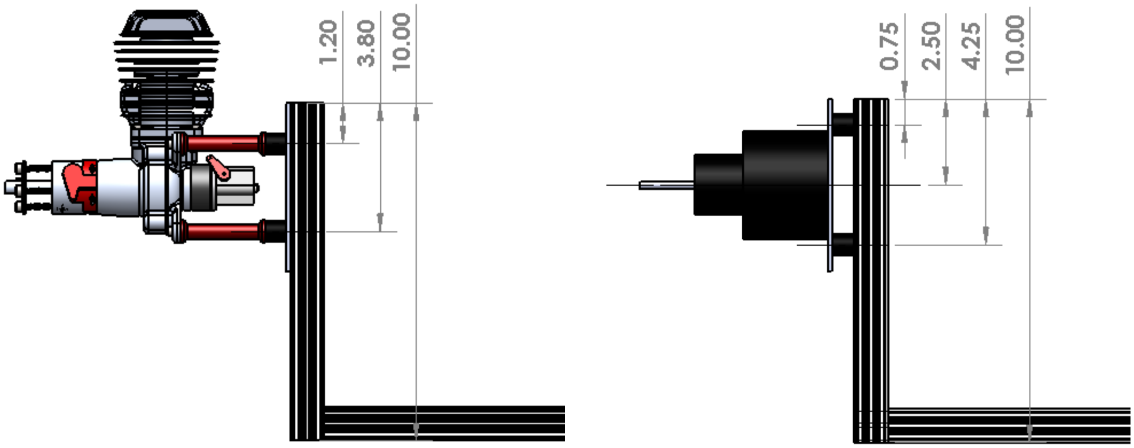

Figure 95: Dampener placement on engine and electric motor test stand, dimensions in inches.

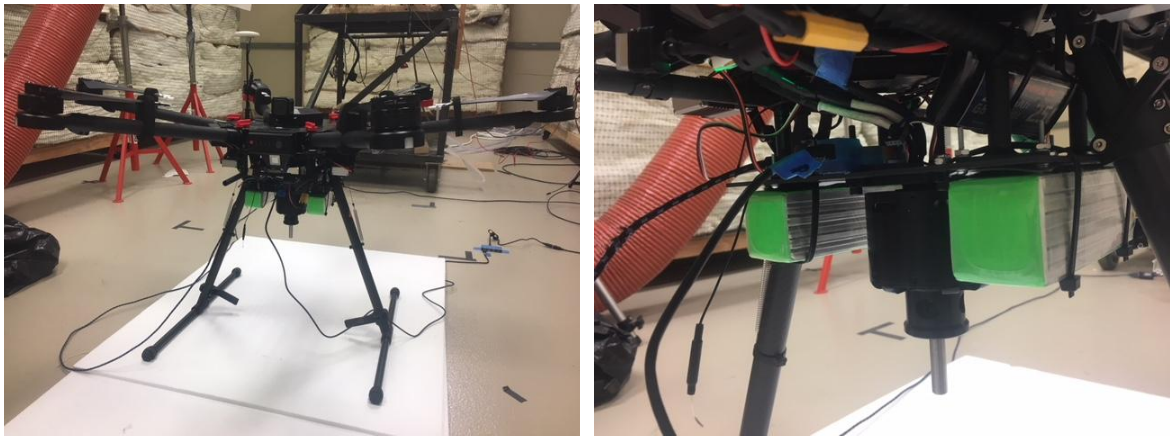

Figure 96: Electric motor with cam mounted to M600 on lab floor

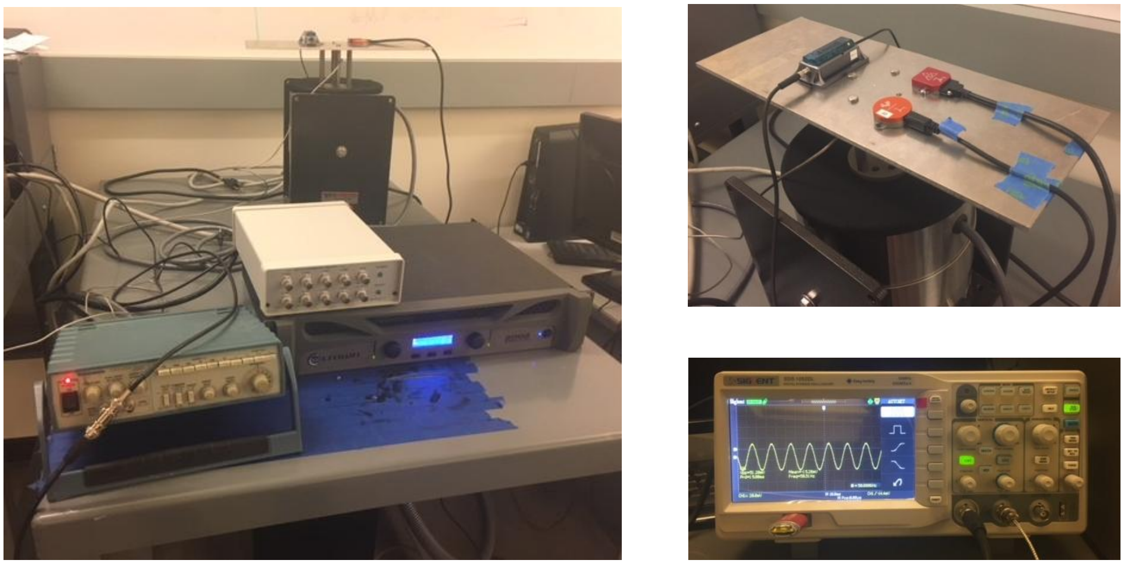

Figure 97: Sensor validation setup. A signal generator is used to produce a sine wave of a specific amplitude and frequency which is then sent through an amplifier to an actuator which stimulates all three sensors simultaneously.

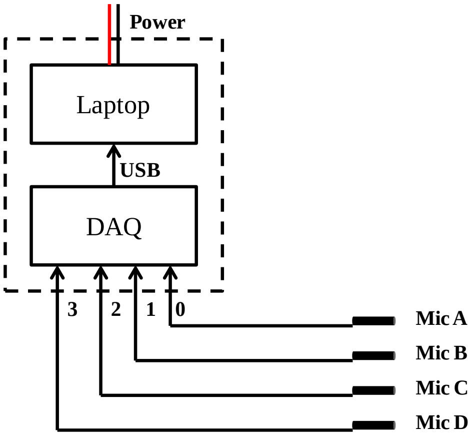

Figure 98: Microphone array wiring schematic

Figure 99: M600 flight testing

Figure 100: Engine testing in the propulsion lab

VITA

Kristen Elise McKinney

Candidate for the Degree of

Master of Science

Thesis: EVALUATION OF HYBRID-ELECTRIC POWER SYSTEM INTEGRATION CHALLENGES FOR MULTI-ROTOR UAS

Major Field: Mechanical and Aerospace Engineering

Biographical:

Education:

Completed the requirements for the Master of Science in Mechanical and Aerospace Engineering at Oklahoma State University, Stillwater, Oklahoma in May, 2018.

Completed the requirements for the Bachelor of Science/Arts in Mechanical Engineering at Oklahoma State University, Stillwater, Oklahoma in December, 2016.

Experience:

Student Engineer - Southwest Research Institute, San Antonio, Texas
Research Assistant - Oklahoma State University, Stillwater, Oklahoma

Professional Memberships:

AIAA Student Member